Observing the dynamic Sun: MHD waves in the chromosphere

K. Mooroogen

PhD

2017

Observing the dynamic Sun: MHD waves in the chromosphere

Krishna Mooroogen

A thesis submitted in partial fulfilment of the requirements of the University of Northumbria at Newcastle for the degree of Doctor of Philosophy

Research undertaken in the

Department of Mathematics, Physics and Electrical Engineering

May 2018

Abstract

Due to their ubiquity in the atmosphere magnetohydrodynamic waves have been theorised to play an important role in the coronal heating problem. The kink wave in particular, due to its Alfvénic qualities, is thought to be able to transport energy over the large distances of the stratified solar atmosphere. In the principal study, 'Dynamics of internetwork chromospheric fibrils: basic properties and MHD kink waves', we provide the first investigation on the nature and dynamics of elongated absorption features (fibrils) observed in H-α in the internetwork. The fibrils were found to support wave-like behaviour that we interpret as the MHD kink wave. Using the spectroscopic imaging capabilities of the Swedish Solar Telescope, multi-scale image processing, Fourier analysis and sub-pixel model fitting we provide a statistical study of these waves.

In the second study, 'Observational evidence of Kink waves in Ca II (8541 Å) super-penumbral fibrils'; we present the first observation of kink waves in a sunspot super-penumbra. By employing similar methodologies to the first study, we suggest that the kink waves may be the result of mode conversion of low-frequency magnetoacoustic waves propagating from the lower atmosphere.

Of both studies, we present the measured properties of the amplitudes and periods of the kink waves; we found similar behaviour to those previously studied in different atmospheric regions. However, we provide one of the few comprehensive measurements of the wave propagation speed, that serves as an approximation to the local Alfvèn speed. We find that relative to the Ca II data, the H-α kink waves have large phase speeds. Further, we exploit the wave properties via inversion to perform magneto-seismology. With this, we are able to infer the variation of plasma properties of the fibrils. Lastly, we develop average power spectra of the quiescent H-α and active Ca II chromosphere as a method of examining the local propagation of wave power. On comparison to previous results we observe amplification of power from the photosphere to chromosphere, supporting the notion of a stratified atmosphere.

The results of the measurements serve to constrain the properties of internetwork and super-penumbral fibrils to aid in the understanding of their role as wave guides. The discovery of kink waves in the Ca II super-penumbra may prove to be a source of Alfvénic waves in active regions in the corona.

Contents

Acknowledgements

The road to my PhD has been long and bumpy. However, along the way a host of notable people have supported and aided me. It is here I give them thanks.

Firstly, to my supervisor Richard Morton, you gave me the chance that nobody else would and without your guidance this work would not have been possible. David Williams, you provided the opportunity that led onto my PhD and yes I still need to give you back Joy's work! Stuart Boogert, my masters supervisor and ongoing mentor, you laid the foundations of my physics knowledge and without your inspirational talks I would have given up. You gave me advice throughout my journey, more so than any academic should need to bother. I'll be sure to pay it forward.

To the senior staff and colleagues at Northumbria University, James McLaughlin, Stephane Regnier, Eamon Scullion, Malcolm Druett and Ben J Snow, your assistance and knowledge have been invaluable. Special thanks to, Micah Weberg for putting up with my code requests and Vasco Henriques for my data.

To the lads in the PA, you know who are and you know what you did! Courtney Cox. Thanks for always being around and providing the much needed distractions. There isn't enough room to thank all of you, but big thanks to Luke for helping me move and Alex, thanks for everything mate.

To my physics crew, Dave, Angelo, Dre and Katie, we did it! Sarah and Beej, without your maths problem sheets I would have been quite stuffed. Dre, after all those all nighters in Hitt Lab and the DOP, did we learn our lesson? Dave and Ange, I think I'm going to finish first, do I get to sit in the front now?

To the guys in the PRC, thanks for keeping me grounded.

A very big thanks to my parents and my sisters, without your encouragement and support (and finances!) I wouldn't be here.

Finally, to the most important person, Gaby. You moved across the whole country to be with me, your belief, love and patience has meant everything to me. The fun we've had together over the last three years was essential to my sanity. You are my rock. Thank you.

> *Facts are meaningless. You could use facts to prove anything that's even remotely true.*
>
> – Homer Simpson, *The Simpsons*

Declaration

I declare that the work contained in this thesis has not been submitted for any other award and that the work is of my own authorship. I also confirm that this work fully acknowledges opinions, ideas and contributions from the work of others.

Ethical clearance for the research presented in this thesis has been approved and granted by the University Ethics Committee on 12th February 2016.

I declare that the Word count of this Thesis is 43673

Name: Krishna Mooroogen

Signed:

Date:

1

Introduction

1.1 At a glance

The Sun, our closest star has fascinated peoples for millennia, its omnipresence led civilisations to worship it as a god and throughout history it has remained a central object in culture and religion. Today, this fascination continues; however, we take a more pragmatic approach, focusing on the science rather than the supernatural.

The Sun is of course essential to our existence; it provides the energy required to sustain life and by means of thermal input into the atmosphere and oceans, drives the climate. Yet its importance goes beyond this; the Sun also generates a magnetic field, this is caused by the dynamo effect resulting from motions of ionised gas in the solar interior. This magnetic field which is known as the heliosphere, reaches out across space and marks out the boundary of our solar system. It acts as a magnetic barrier to interstellar radiation that would otherwise bombard the solar system. The modulation of the cosmic radiation can be seen over the Sun's periodic magnetic activity cycle, where over an eleven year period the Sun's magnetic activity increases and decreases. This modulation arises from both the magnetic barrier that appears enhanced during the increasing stage of the magnetic cycle but also from solar energetic particles (SEP) emanating from the Sun scattering cosmic radiation, (Balasubrahmanyan, 1969, McCracken et al., 2002).

However, the Sun also brings with it a violent and temperamental manner. Above the Sun's surface embedded with a complex network of magnetic fields, the solar atmosphere exceeds temperatures of millions degrees, exploding and shaking with activity. This temperature is in stark contrast to the Sun's surface, a mere six thousand degrees and after examining the solar energy budget it would seemingly violate classical thermodynamics. This vast temperature discrepancy is described as the coronal heating problem and is

hypothesised to be caused by the release and transportation of energy stored or guided by the magnetic field.

It is this magnetic field that drives the Suns dynamic behaviour; the eleven year solar cycle that is linked to the myriad of events that light up the Sun's atmosphere, e.g. solar flares, coronal mass ejections but also the vast speeds of the solar wind (100's km/s). These are some of the largest, most energetic phenomena in the solar system, all of which generate what we call space weather. Space weather is concerned with near Earth environmental changes that vary over time, specifically solar particle interactions with the magnetosphere, ionosphere and thermosphere of the Earth. These phenomena can have a direct impact, with the potential for solar magnetic storms to damage satellites, bring harmful radiation to aviation crew and in extreme cases, causes geomagnetic storms that damage power networks (e.g. 1989 Quebec blackout). In fact, it is thought that the solar wind contributed to the stripping of the atmosphere of Mars, a fate the Earth's own magnetic field protects us from, (Jakosky et al., 2017).

Physicists are still yet to understand the energy exchange through the atmosphere that powers this activity. In order to interpret these large-scale events one must peer into the layers of the Sun's atmosphere and observe the finer details.

This thesis will examine the fine-scale structures of the solar atmosphere using newly developed state-of-the-art instrumentation. The goal of the research is to study the properties of magnetohydrodynamics (MHD) oscillations supported by these structures. We aim to develop the understanding of the role these features play in energy transport in the solar atmosphere in lieu of advancements in instrumentation. The focus of the study will be the chromosphere, a region in the Sun's atmosphere that requires significant energy flux to heat it. In this introduction the necessary background topics and literature will be discussed in order to give context to the original research.

1.2 The Sun: The interior & atmosphere

The Sun is described as a yellow dwarf star on the main sequence of the Hertzsprung-Russell diagram (Weston, 1972), with a spectral classification of G-class. It was formed approximately 4.5 billion years ago when a vast rotating cloud of gas, dust and particles came together under gravity. The centre of this cloud grew in mass over time, bringing in more surrounding material. The cloud would gradually spin faster, conserving angular momentum as its radius would shrink, until eventually the cloud collapsed and flattened into a disc. This disc later formed our solar system and all the planets in it. The centre of this disc grew as more mass gathered under gravity, until the pressure was

intense enough for the gas to undergo nuclear fusion. The Sun formed into a spherical mass due to conservation of angular momentum and remains balanced via hydrostatic equilibrium, where gravity and pressure, from the energy released from fusion, balance. This will continue until the Hydrogen that fuels the Sun is used up (another five billion years from now) and the Sun enters it's red giant phase, expanding to several times its size until it begins to fuse Helium.

The Sun is described as having seven layers, distinguished by their relative physical properties. The interior of the Sun is separated by its key modes of energy transport and densities, it is made up of the core, radiation zone and convection zone. The photosphere, chromosphere and corona make up the bulk of the atmosphere with the 'transition region' occupying a much narrower region between the chromosphere and corona. A short description of each layer can be found in the following subsections.

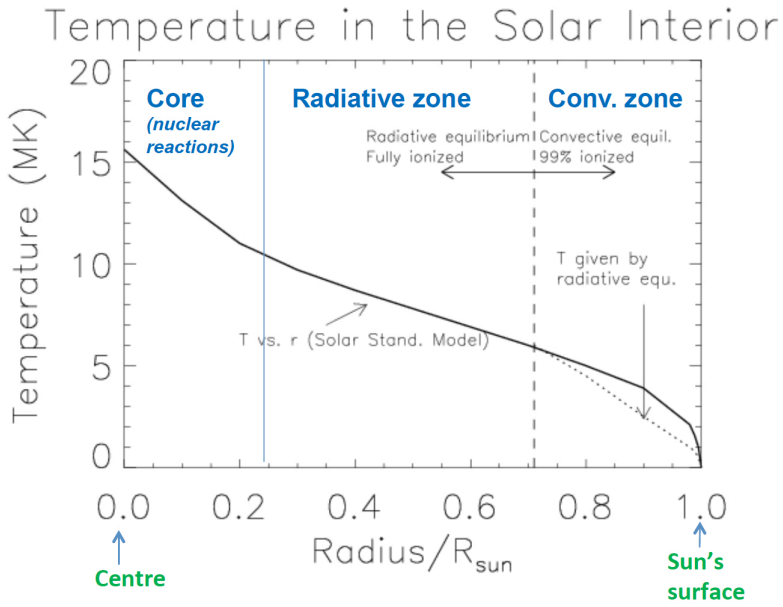

FIGURE 1.1: **Temperature Profile of the Solar Interior.** The three interior layers, the core, radiative zone and convection zone are separated vertically by radius. It can be seen clearly form this profile the temperature decreases from the core outwards to the surface. The radius is shown as a fraction of the total solar radius. Image credit: UCL Solar Physics undergraduate course, David Williams and Lidia van Driel-Gesztelyi.

1.2.1 The Core

The solar core is where nuclear fusion takes place; where ionised Hydrogen, under immense gravitational pressure, overcomes the Coulomb barrier and is fused into Helium. This process occurs via proton-proton chain and Carbon-Nitrogen-Oxygen cycle. As well as producing Helium, energy is released equal to the mass-energy difference between the product atom and the reactants. Successive fusions in the core go on to create heavier

elements but in fewer abundances. The core is approximately a quarter of the solar radius and hosts temperatures in excess of ten million degrees kelvin, (Priest, 2014, p.p 10).

1.2.2 Radiative Zone

The next layer, the radiative zone, is named for the prominent energy transport mechanism in that layer, radiation. Since the gas pressure in the interior of Sun is larger than radiation pressure, it could be expected that conduction would play a significant role in energy transport. However, the electron mean free path is so small, compared to the Sun's length scales, that conduction is negligible and so radiation dominates the transport mechanism.

Photons, released from fusion reactions, carry energy from the core outward in the so called random walk fashion, this term comes from the fact that large densities in the interior cause photons to be scattered by free electrons (Thomson scattering) on small spatial scales. The photons mean free path in this region is so small, it takes as much as 170,000 years for photons to travel from the core to the surface, (Priest, 2014, p.p 6). This region extends to 70 % of the solar radius, (Priest, 2014, p.p 12).

1.2.3 The Convection Zone

Next is the convection zone, named again from the dominant mode of energy transport in that region. Convective motions occur in fluids when a local rising element is less dense than the surrounding regions. In these regions hot parcels rise (adiabatically) to the photosphere where they radiate, cool and become denser then fall back down. The process continues as a cycle, with the interior fluid mass giving up its energy to the surface. This depends on the rate that element expands due to decreasing pressure, and the rate of decreasing ambient density as a function of height. More specifically, this instability arises when the temperature gradient exceeds some critical value (the adiabatic constant, specific to the medium), this is known as the Schwarzchild criterion. In the convection zone, higher rates of recombination (free electrons with ions) increase absorption rates causing opacity to increase, and as a result a steeper temperature gradient forms. This gradient is steeper than in the radiative zone, Fig. 1.1, and the reduced temperature ($\sim 10^6 K$) meets the required value for the onset of a convective cycle.

Separating the radiation zone and the convective zone is a shear layer known as the tachocline, where it is thought that most of the Sun's magnetic field is generated by

the dynamo, (Tobias & Weiss, 2007). The convection zone extends to the surface to the Sun.

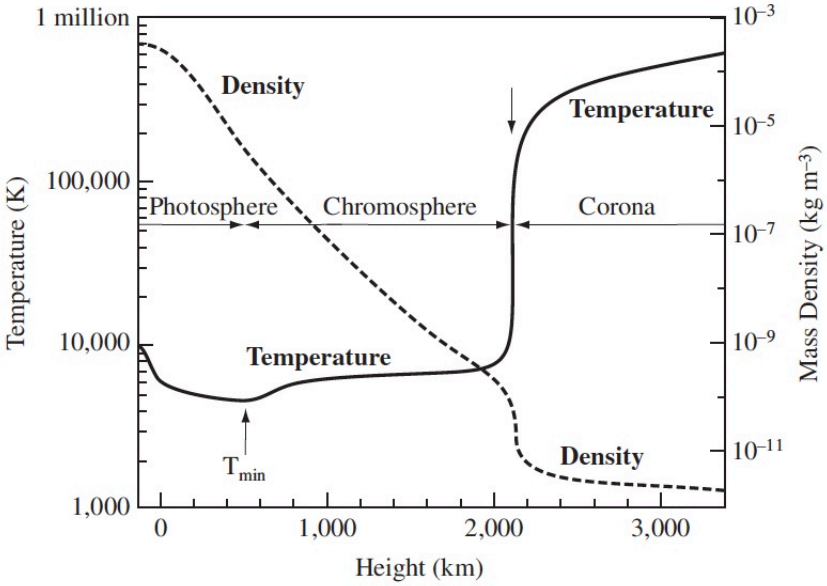

FIGURE 1.2: **Temperature and Density Profile of the Atmosphere.** Schematic model showing the mean temperature and density profiles of the atmosphere from the Vernazza-Avrett-Loeset model. The origin on x axis starts at the solar 'surface' at maximum radius. Image credit: (Priest, 2014, p.p 8).

1.2.4 The Photosphere

The atmosphere is identified by its plasma properties, i.e., temperature and density, into four parts, the photosphere, the chromosphere, transition region and corona. The relative organisation of the interior and atmosphere can be seen in Fig. 1.3.

The photosphere is a relatively thin layer at only few 100 km, this is where the majority of the Sun's photons escapes towards Earth, making it easily observed in the visible spectrum. This is because compared to the interior of the Sun, the atmosphere is significantly less dense. As such, there is a smaller abundance of matter to absorb and scatter the photons. In turn, this makes the atmosphere approximately transparent to photons emitted by the photosphere and thus the photosphere is considered the effective 'surface'. The boundary where the atmosphere starts is at the temperature minimum at a temperature of 4100 K. This is approximately 500 km above the photosphere and the point where the photons escape, (Priest, 2014, p.p 21).

A defining feature of the photosphere is the pattern of granulation. These are cells of plasma that have clear boundaries of varying size on the order of thousands of kilometres. Super-granules however, exist at scales a factor of ten larger. The granulation

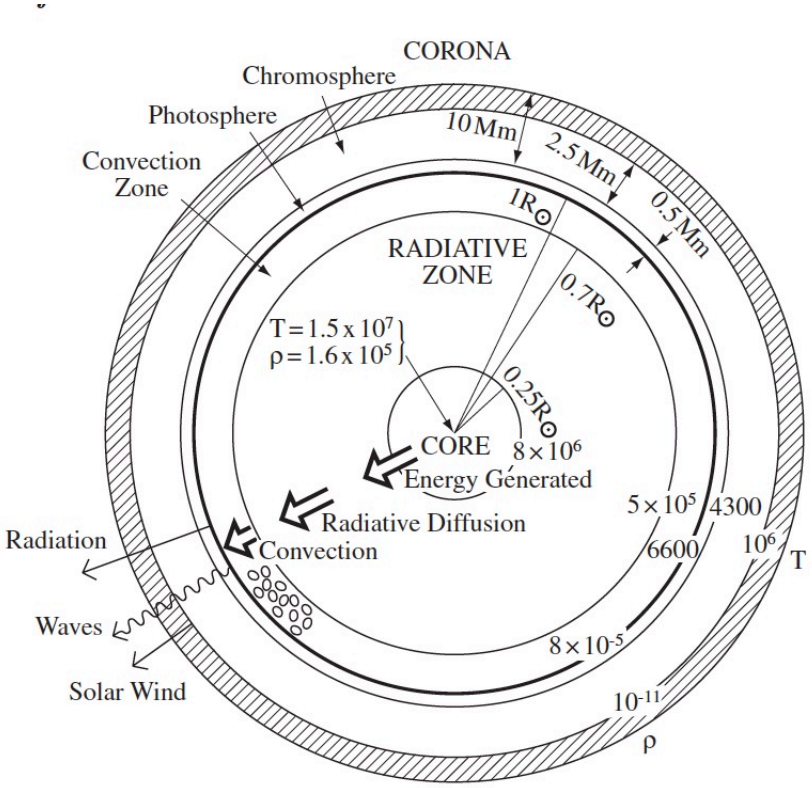

FIGURE 1.3: **Solar model.** Schematic diagram showing the relative layers of the Sun and their length scales given in Mm and as a function of the solar radius (R) where shown. Values for average densities and temperatures are indicated with the notation (ρ, T) respectively. Large arrows indicated the transport of bulk energy from the core to the photosphere, convection is shown as granules in the convection zone, the curved arrow that points from the photosphere outwards represents the propagation of waves into the atmosphere, The straight arrow of like-direction signifies the photospheric radiation and the final arrow leaving the corona indicates the solar wind. Image credit: (Priest, 2014, p.p 6).

patterns are a distinct signature of the convection occurring below. These convective motions generate acoustic waves that peak at approximately 3 mHz, and this time-scale resembles that of the life-times of the granules. Confined in the sub-surface layer, the acoustic waves are known as the p-modes (Priest, 2014, p.p 16). These waves have the potential to perturb the photosphere and drive oscillatory features seen there. The p-modes are able to leak into the atmosphere, where they can drive magnetoacoustic oscillatory phenomena (e.g. running penumbral waves). However, only waves with frequencies higher than the acoustic cut-off frequency (approximately 5.2 mHz) can propagate, lower frequency waves are evanescent. Some acoustic waves below this frequency reflect internally and along with f-modes, which are surface/gravity waves, and are exploited for helioseismology (the use of waves to infer the internal structure of the Sun).

Magnetic flux emergence from the interior manifests in two ways; small-magnetic flux

is dragged up from the interior via the convective motions and breaks through granular cells, the flux is then expelled to the edges where it gathers in inter-granular lanes. In certain spectral lines, small-scale flux that has gathered within granular lanes can appear bright, these are known as magnetic bright points. However, in regions with lager magnetic flux, convection is suppressed and flux emergence is due to magnetic buoyancy. This where the internal plasma density of a magnetic flux tube is less than the density of the surrounding plasma (whilst in the thermal equilibrium), causing the tube to rise buoyantly due to gravity. Where a flux tube can be described simply, as magnetic flux bundle that is modelled as a cylindrical tube, more on this later (subsection 1.4.2). The assumption of thermal equilibrium is imposed here to separate the effects of convection, which as discussed can drag up the magnetic field. We can describe the process in more detail by first defining the ideal gas equation of state,

$$P = \frac{R}{\mu_m}\rho T, \tag{1.1}$$

where P is the gas pressure, ρ is the density, R is the gas constant, μ_m is the mean atomic weight and T is temperature. Now, we consider a magnetic flux tube in local hydrostatic equilibrium. In this case the total pressure inside the tube requires an additional term for magnetic pressure,

$$P_e = P_i + B^2/2\mu_0, \tag{1.2}$$

where the subscripts, $(e\&i)$, refer to external and internal properties respectively, B is the magnetic field and μ_0 is the magnetic permeability. If in this case we assume thermal equilibrium such that $(T_e = T_i)$, and then substitute Equation 1.1 for the values of internal and external gas pressure and rearrange we obtain,

$$\rho_e - \rho_i = \rho_e B^2/2\mu_0 P_e. \tag{1.3}$$

Here, we can see that the internal density is less than the external density and hence the tube rises.

The interconnection between the plasma and the magnetic field stems from the frozen-in flux condition (*Alfvén*), (Schnack, 2009). From Alfvén's theorem, the condition states that in a conductive fluid, motions along the field lines do not change the field, but transverse motions carry the magnetic field with it. Mathematically, this is described by,

$$\frac{d\Phi}{dt} = \frac{d}{dt}\Big(\int_C B.ds\Big) = 0, \tag{1.4}$$

where Φ is magnetic flux, t is time, s represents the surface that encloses the field and C is any closed contour moving in the fluid, (Hood, 2000). Essentially, this equation describes the invariance of magnetic flux in time, in a moving fluid, resulting in the condition of the magnetic field lines being *frozen-in*.

The flux is continually emerging, separating and at times cancelling with itself on time-scales on the order of hours, forming what is referred to as the magnetic carpet. The photospheric magnetic field is relatively strong compared to the atmospheric magnetic fields but due to the large gas pressure and density, the dynamics are dominated by the plasma pressure (in the general case, not true for active regions and areas of local magnetic activity). The ratio between gas pressure and magnetic pressure is denoted the plasma beta (β) given by,

$$\beta = \frac{2\mu_0 P}{B^2} \tag{1.5}$$

When $\beta >> 1$ the pressure balance is described by the plasma distribution and the magnetic field contribution is negligible. However, when $\beta << 1$ the magnetic pressure dominates, (Judge, 2006). Thus in active Sun regions such as Sunspots, where the magnetic field is stronger relatively, β is small and vice versa for quiet Sun regions.

Plasma density, and in general pressure decreases with height, Fig. 1.2. In fact pressure falls off due to the average hydrostatic equilibrium (balance between gravity and pressure), as gravity decreases with distance from the core so does pressure. As a result, rising magnetic flux tubes expand as they reach higher into the atmosphere, this expansion cause the field lines to fan out forming a network known as the magnetic canopy. It is this canopy that contributes to the dynamic features seen in the chromosphere, but also supports the plasma that makes up the chromosphere and corona against gravity. In fact, both the magnetic field and gas pressure decrease with height but while magnetic field does so at scales of thousands kilometres, the gas pressure does so at hundreds kilometres, (Zirin, 1988, p.p 155). Therefore, the gas pressure becomes less dominant in respect to the magnetic field with increasing height. However, this is only true in the general case and β can vary over heights, (Gary, 2001).

1.2.5 The Chromosphere

The chromosphere is a highly dynamic, magnetically dominated region that is optically thin in continuum wavelengths, (Zirin, 1988, p.p 155). However, it can be easily observed in the narrow band of the Balmer and Ca II strong resonance lines, where it appears opaque, (Uitenbroek, 2006) and (Zirin, 1988, p.p 155). The chromosphere is

distinguished by a host of unique fine-scale magnetic features for example, spicules, fibrils and mottles. These features permeate the chromosphere and have been observed to exhibit oscillations, we will discuss these in further detail in the later Section 1.5.

The chromosphere is an inhomogeneous region, not a purely spherical uniform layer, it is estimated to occupy a height on the order of a few mega meters. In terms of its density relative to the rest of the atmosphere, it is less dense than the photosphere but denser than the corona. The gas pressure is much lower here than in the photosphere, and the magnetic field becomes the dominant force. From Fig. 1.2 we can see that it is in the chromosphere that temperatures begin to rise, from the temperature minimum to several thousand degrees kelvin.

1.2.6 Transition Region and Corona

The transition region is heterogeneous, this means that it is not a distinct, uniform layer but better described as regions of the atmosphere that hold specific temperatures and densities. This layer exhibits a steep temperature gradient that leads onto coronal temperatures in the millions of kelvin. Models give an approximate thickness of 30 km for a temperature change of 10^4 to 10^5 K, (Priest, 2014, p.p 34). This can be seen in Fig. 1.2 as the near vertical rise in temperature and drop in density. Thus, the transition region sharply separates the chromosphere from the corona. This rapid change in physical properties suggests that in part some phenomena or process in the transition region facilitates the large temperature of the corona. This in turn inspired the creation of the Transition Region and Corona Explorer (TRACE), that took data until 2010, and the recently built Interference Region Imaging Spectrograph (IRIS).

The solar corona is the outer most layer of the Sun and also the least dense. However, it holds temperatures on the order of a million degrees kelvin. The gas pressure here is significantly lower than in the photosphere and so the magnetic field pressure dominates the dynamics, (Priest, 2014, p.p 34). The corona is mostly transparent in the visible wavelengths, meaning that it lets through the large photospheric photon flux. However, during an eclipse when the solar disk is occulted and the photospheric light is blocked from view, the corona can be seen as a 'crown' around the Sun, Fig. 1.4. The white light seen coming from the corona during an eclipse is actually light from the photosphere that undergoes Thomson scattering by electrons in corona as it passes through, this scattering then reveals the structure of the corona in the visible wavelengths.

Due to the high temperatures in the corona it is easily viewed in extreme UV and X-ray spectral lines. Observations are therefore carried out from space-based instruments, where the Earth's atmosphere does not absorb the radiation. The corona is well known

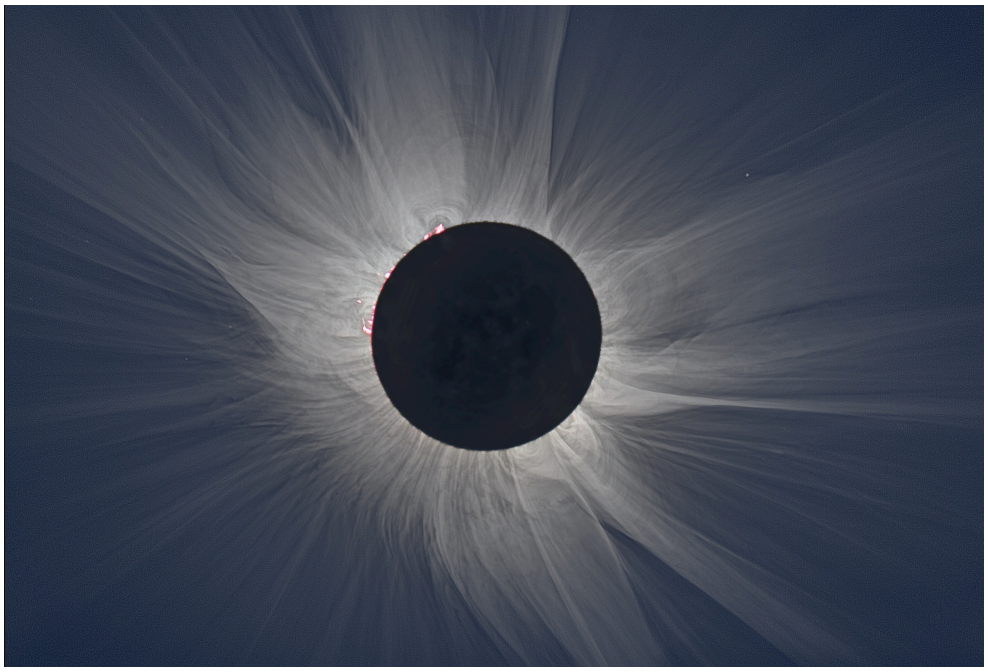

FIGURE 1.4: **Total Solar Eclipse.** Image of a total solar eclipse: the corona or 'crown of the Sun' can be seen as the long strands emanating from the limb of the solar disk. This white light is scattered towards the viewer during an eclipse and is the only time that the white light of the corona can be viewed unaided thanks to the light of the photosphere being blocked out in the viewers direction. The pinkish hue visible on the left side of the limb, is the chromosphere. Image credit: S. Habbal & Aniol (2017).

for it's iconic coronal loops, solar flares and coronal holes which appear over areas of increasing magnetic activity respectively. The solar wind is essentially the supersonic expansion of the corona, hypothesised by Parker, (Parker, 1958), that reaches out across the solar system bringing with it the frozen-in magnetic flux.

1.3 The heating problem

The Sun's temperature profile indicates cooling from the core to the surface at a temperature on the order of $\sim 10^3$. However, in the chromosphere temperatures begin to rise again and sharply increase in the transition region to values on the order of $\sim 10^6$ in the corona, Fig. 1.5. This profile is at odds with the known fact that the main source of the Sun's energy is produced deep in its interior, at the core. Classical thermodynamics would lead us to believe that the temperature should drop off with distance from the source. The discovery of the heated solar atmosphere followed from the observation of highly ionised Iron in the solar corona that can only occur at high temperatures on the order of millions of degrees, (Parnell & De Moortel, 2012). Evidence would suggest that the temperature rise could not be due to radiative transfer as the majority of the photospheric radiation passes through the corona, and therefore some alternative method

of energy transfer is required to heat the Sun's atmosphere. This has become known as the coronal heating problem.

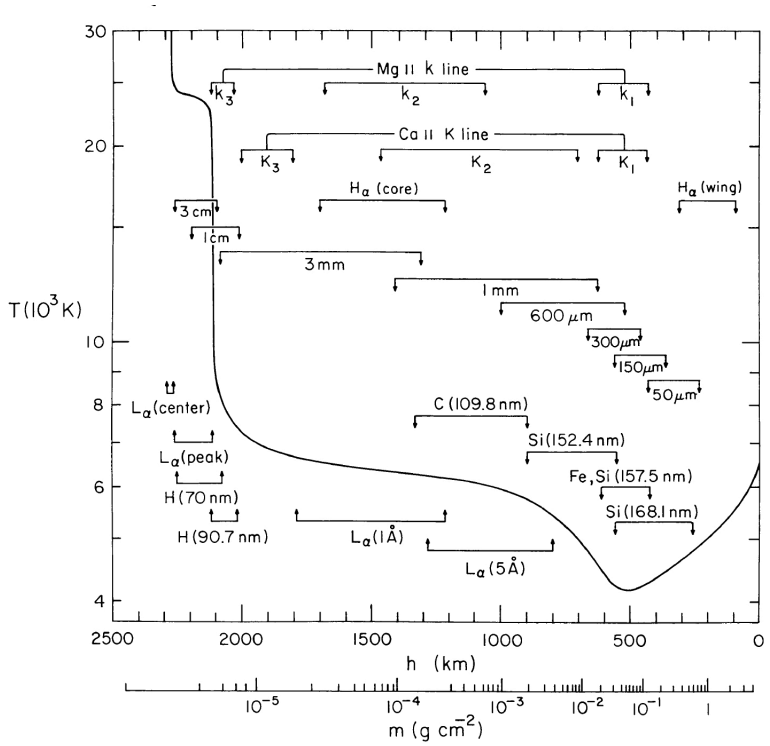

FIGURE 1.5: **Vernazza-Avrett-Loeset Model.** VAL model showing the temperature profile of a modelled Sun-like stellar atmosphere. The formation heights of specific spectral lines are indicated. Image credit: (Vernazza et al., 1981).

Much of the focus of the heating problem falls onto the staggering temperatures of the corona, which is understandable considering the orders of magnitude in temperature difference with the photosphere. However, chromospheric heating actually poses a more subtle mystery. With its larger density the chromosphere requires a larger energy input than the corona to heat it, (de la Cruz Rodríguez et al., 2013, Jess et al., 2015).

Currently, there exists two popular explanations for the atmospheric heating. First, there is the hypothesis that magnetic reconnection events are responsible for direct heating of the plasma. Secondly, it is proposed that Magnetohydrodynamic (MHD) oscillations propagate throughout the atmosphere and dissipate energy.

However, the recent paradigm is one that favours a combination of the two viewpoints, where reconnection events are significant in active regions and waves more so in quiet regions. Further, the two phenomena can be brought together under the theory of MHD turbulence. (van Ballegooijen et al., 2011) and later papers present a model that suggests MHD oscillations driven by convective motions that undergo non-linear interactions can incite braiding of the magnetic field. This in turn can result in reconnection events that resemble energies of the so called 'nano-flare' models, discussed in next subsection 1.3.1.

Furthermore, oscillatory reconnection (McLaughlin et al., 2009, 2012a,b) offers another method in which the reconnection and wave viewpoints can be related. In this process it is hypothesised that a reconnection event could trigger waves, that in turn perturb the magnetic field to facilitate further reconnection. In this manner, a series of wave and magnetic field interactions make it possible for many mechanisms of heating and energy transport to occur.

An extensive volume of literature has been dedicated to both MHD waves and reconnection in reference to atmospheric heating, as such they will only be discussed briefly here.

1.3.1 Reconnection

Magnetic reconnection is the reconfiguration of magnetic field topology when oppositely directed magnetic fields diffuse and connect, (Priest, 2014, p.p 189). This can occur when magnetic flux emerging from the surface below entwines and cancels or when magnetic field is brought together by movement of plasma in which the field is coupled, (Aulanier et al., 2007, De Moortel & Galsgaard, 2006). Reconnection events convert magnetic energy into kinetic energy, analogous to a stretched rubber band snapping. In addition, there will be direct heating via ohmic dissipation of charged particles in the plasma, but also indirect heating via viscous damping of waves of the subsequent displaced plasma, (Priest, 2014, p.p 194) and (Parnell & De Moortel, 2012). It remains an open question whether direct or indirect heating dominates, though it is likely to depend on the reconnection regime.

Observations of solar reconnection events are typically associated with, but not limited to solar flares. These large-scale events occur when sections of field become detached during the reconfiguration and are accelerated away carrying with it hot plasma that is eventually reclaimed by the Sun's gravity. Recent evidence have shown that flares in the upper atmosphere have the ability to heat lower regions via beam injection, (Druett et al., 2017). Though significant energy is released during these large-scale events, they do not occur frequently enough to sustain prolonged heating. The mechanism proposed by, (Parker, 1988), the so called nano-flare model, sought to address this. The hypothesis suggested that frequent enough small-scale, impulsive reconnection events could deliver the energy required over the needed time-scales. Parker's original definition of nano-flares was prompted by observations of local brightening with energies on the order of 10^{24} $ergs$, which is approximately a billionth smaller than a large flare event. However, current definitions of nano-flares include energies much smaller than this. As such, other events that show brightening observed along the line-of-sight, that fall into this energy

band, are often mistakenly identified as nano-flares, (Klimchuk, 2015). The condition then remains that these events must have high enough frequencies to produce regular heating, in other words the time between successive events must be smaller than the plasma cooling time. However, direct observation has yielded limited determination of the distribution of nano-flare energies, (Parnell, 2004), though a handful of papers have record indirect evidence of these events, (Jess et al., 2014, Sakamoto et al., 2008, Terzo et al., 2011).

Observations have generally been limited by the available instrument resolution required to probe these small scale events, yet (Testa et al., 2013) has offered some evidence. Instead, forward modelling techniques are needed to compare theoretical models to observational data. In this manner it is possible to simulate nano-flare type scenarios and vary the properties of such a scenario until they match observations.

1.3.2 Waves

As this thesis is focused on the discussion of MHD oscillations in the chromosphere, a comprehensive overview of the MHD wave modes and features will follow in later sections. However, an introduction to the topic of MHD waves as a participant in atmospheric heating will be described here.

MHD oscillations, driven by convective motions (Khomenko & Calvo Santamaria, 2013) have seen to be ubiquitous in the solar atmosphere, (Banerjee et al., 2007, De Moortel, 2009, De Pontieu et al., 2007a,b, Hillier et al., 2013, Jess et al., 2015, Mathioudakis et al., 2013, Morton et al., 2012a, Tomczyk et al., 2007). It is their sheer abundance in the atmosphere that makes them popular targets of research in regards to the heating problem. In order to sufficiently heat the atmosphere, the waves need to carry a significant flux of energy to the upper atmosphere whilst depositing some of that energy into the chromosphere. Further, the waves need to be able to efficiently dissipate energy over specific time scales, (Parnell & De Moortel, 2012).

In a homogeneous plasma, three wave varieties present themselves as candidates for energy transport, Alfvén, fast and slow magneto-acoustic waves, (Khomenko & Cally, 2012). The two magneto-acoustic waves are compressible meaning the associated restoring forces are predominantly magnetic pressure and plasma pressure, (Jess et al., 2015). As compressible waves, they are susceptible to rapid damping by kinematic processes in the environment and thus are less likely to propagate into the upper atmosphere.

Conversely, Alfvén waves appear to be promising candidates for energy transport as they are incompressible, with only magnetic tension as the restoring force. This means

they are able to traverse over the several layers of the stratified atmosphere with little dissipation, theoretically carrying enough energy to balance radiation losses. However, this very quality also makes it difficult to deposit their energy, as this needs large Alfvén speed gradients that occur over short spatial scales to facilitate the required rate of plasma heating. The Alfvén speed (V_A) is the velocity related to their propagation in a magnetised environment, which is dependent on both the local plasma density (ρ) and magnetic field strength (B),

$$V_A = \frac{B}{(\mu_0 \rho)^{1/2}}. \tag{1.6}$$

In reality, the solar atmosphere is an inhomogeneous plasma; in this scenario MHD waves have mixed properties (for some modes), meaning that they are described using facets of the slow, fast and Alfvén waves. One such wave that receives close attention due to its Alfvén-like qualities is the kink wave. The kink wave is readily observed in a host of features, it exhibits a transverse perturbation about its central axis that is indicative of the fast magnetic wave. However it also perturbs vorticity, which is a property of the Alfvén wave in a homogeneous plasma, thus the kink wave is often referred to as an *Alfvénic* wave.

Three dimensional models have been developed to include the influence of small-spatial scales required to facilitate the dissipation of Alfvén waves; for example resonant absorption, phase mixing and wave turbulence, (Antolin et al., 2015, Karampelas et al., 2017, Soler & Terradas, 2015, Soler et al., 2011). The resonant absorption model appears to be an efficient method to dissipate transverse waves in the solar atmosphere. The theory suggests that transverse motions of the waves in the wave-guide are converted into azimuthal motions as an incoming wave is in resonance with local oscillations at the flux tube boundary on fine spatial scale. The transverse motions are unstable to the kelvin-Helmholtz instability (KHI) because of the shear motions. The KHI deforms the boundary of the flux tube dissipating the wave energy into heat via thin turbulent current sheets, (Okamoto et al., 2015) and reference therein. In a two part paper, (Okamoto et al., 2015) and (Antolin et al., 2015) present observational evidence for resonant absorption as measured with a spectrograph. Further, the authors show with numerical modelling, the importance of the KHI efficiently extracting energy from the resonant layer. A host of studies exist exploring resonant absorption and KHI and some of these are listed here, (e.g., Soler et al., 2009, 2010, Terradas et al., 2010). (Goossens, 2008) provides a detailed mathematical review of resonant absorption in the context of coronal loops.

Phase mixing describes a scenario in which transverse waves on neighbouring field lines with different Alfvén speeds become gradually out of phase generating increasingly large transverse gradients until dissipation length scales are achieved, (Parnell & De Moortel, 2012).

However, all wave types including the Alfvén mode, with its incompressibility, are subject to partial reflection at the transition region boundary due to the steep temperature, and density gradients. This further reduces the flux that can reach the corona, (Cally, 2011, Hansen & Cally, 2012, Snow et al., 2015). (Cranmer & van Ballegooijen, 2005) suggest as much as 95% of Alfvén waves are reflected at the boundary.

1.4 Plasma & Magnetohydrodynamic waves

In this section we present the basic definitions of a plasma and the concepts of MHD wave modes in a cylindrical flux tube model.

1.4.1 Plasma

The Sun, like all stars, is made up of plasma; the so called fourth state of matter. Plasma is a quasi-neutral gas of charged and neutral particles that exhibits collective behaviour, Fig. 1.6. In a quasi-neutral gas, transient net concentrations of like-charge particles exist. However, on average ion and electron densities are the same, and so on large scales the gas is neutral, (Goossens, 2003, p.p 1). Charge concentrations can arise due to random and organised (oscillations/waves) motions, these concentrations are short lived due to electrostatic forces acting to break up regions of like-charges. A plasma's collective behaviour depends on both remote and local conditions. A charged particle is a source of electric field and when in motion, constitutes a current which in turn generates a magnetic field. Concentrations of charged particles in motion then generate strong electromagnetic forces that can be felt by particles in the plasma over long ranges, (Goossens, 2003, p.p 2). Remote areas 'react' to the local concentrated areas causing collective interactions. For collective behaviour to be possible the plasma needs to be a gas of 'free' charged particles such that the dominant forces influencing the behaviour is the Coulomb force from electromagnetism and not particle collisions.

1.4.2 Magnetohydrodynamics concepts

Magnetohydrodynamics (MHD) serves as a set of mathematical approximations that describe the motions of an electrical conducting fluid, e.g. plasma. These approximations

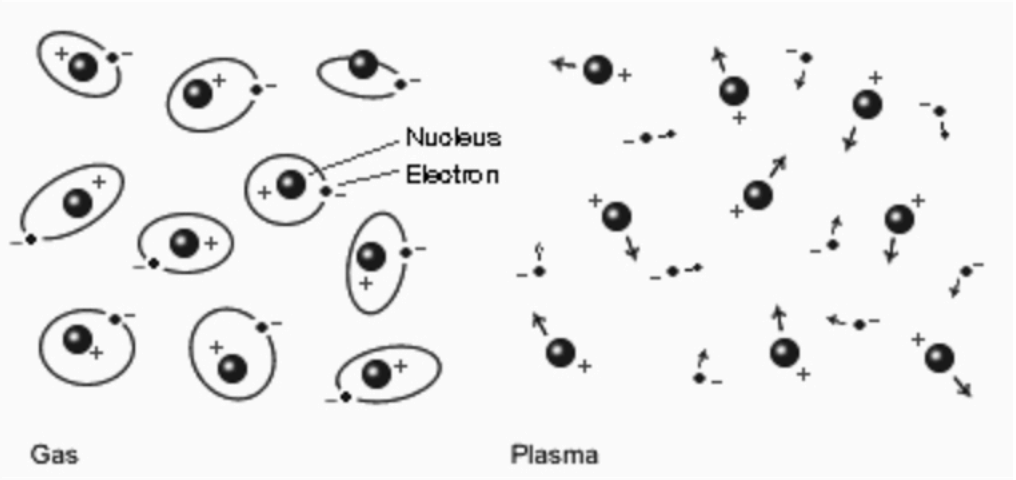

FIGURE 1.6: **Plasma-Gas Make up.** Diagram depicting gas (*left*) and plasma (*right*), In a gas the electrons are bound to the nuclei where as in the plasma the electrons are free or partially free. Image credit: (institute for Plasma Physics, 2003).

are derived from the Navier-Stokes equations from fluid dynamics and the Maxwell equations from electrodynamics, however it is also possible to derive them completely from kinematics. MHD is a well suited when modelling the macroscopic perturbations of plasma and when the magnetic field plays a dominant role, as with the magnetically guided waves observed in the solar atmosphere. The MHD approximations are easier to compute than the more detailed two fluid MHD or kinetic approximations, (Narayanan, 2013, p.p 38). MHD has been used successfully in the field of solar physics to model the properties of magnetic wave-guides that support oscillations in the solar atmosphere (e.g., Cally & Goossens, 2008, Edwin & Roberts, 1983, Erdélyi & Fedun, 2006, Morton & Ruderman, 2011, Nakariakov & Roberts, 1995, Verth & Erdélyi, 2008). These wave-guides are often modelled as a cylindrical collection of magnetic field lines that together are called a magnetic flux tube. More precisely it is the volume enclosed by a set of field lines that intersect a simple closed curve, (Priest, 2014, p.p 100). The terminology derives from the idea that the magnetic field is collectively threading a cylindrical area i.e. a flux.

The magnetic field pre-exists below the solar surface due to dynamo processes in the plasma. As mentioned in subsection 1.2.4, a combination of convective motion and magnetic buoyancy causes the field to rise further into the atmosphere. The appearance of these flux tubes are apparent as the many different observed features throughout the whole solar atmosphere; fibrils, spicules, mottles, coronal loops to name a few, but they all have the same thing in common. The features are the result of emergent flux tubes coupled to the plasma (frozen in flux assumption), their differences lie with the orientation of the field in which they form, as well as local properties such as the magnetic field strength, densities and temperature. Flux tubes are embedded in the

atmosphere and are constantly buffeted by convection induced plasma motion below the photosphere, (e.g., Kuridze et al., 2013, Mumford et al., 2015). This buffeting brings the tubes into motion and can cause oscillatory behaviour.

Recalling Section 1.3.2, there are three distinct wave types in a homogeneous magnetised fluid and these are the Alfvén, fast magnetoacoustic and the slow magnetoacoustic waves, (Jess et al., 2015, Khomenko & Collados, 2006) and (Goossens, 2003, p.p 140). The Alfvén wave in the linear regime is incompressible and the main restoring force is from magnetic tension. The tension force then also dictates the propagation speed of the wave. The two magnetoacoustic waves are compressible in nature and their restoring forces include plasma pressure as well as magnetic pressure forces. We can see the manifestations of these qualities by highlighting the characteristic equations describing MHD waves, (Goossens, 2003, p.p 140),

$$\omega^2(\omega^2 - (c_s + V_A)\nabla^2)Y + c_s^2 V_A^2 k_z^2 \nabla^2 Y = 0, \tag{1.7}$$

$$(\omega^2 - V_A^2 k_z^2)Z = 0, \tag{1.8}$$

where, ω is frequency, c_s is the sound speed, k_z is wave number in the z direction, ∇ is the nabla operator and finally Y and Z are the compressional and rotational components respectively. These are defined as,

$$Y = \vec{k} \cdot \vec{\xi}, \tag{1.9}$$

$$Z = (\vec{k} \times \vec{\xi}) \cdot \vec{1}_z, \tag{1.10}$$

where ξ is displacement parallel to the magnetic field and 1_z is the unit vector in the z direction. Evaluating the solutions for, $\xi = 0$, $Y = 0$ and $Z \neq 0$ leave us with the Alfvén wave solution, Equation 1.8 only. Conversely, if we evaluate $\xi \neq 0$, $Y \neq 0$ and $Z = 0$, we gain the magnetoacoustic solution, Equation 1.7 only. Rearranging Equation 1.7 and solving for ω yields a quadratic equation with solution,

$$\omega^2 = \frac{k^2(c_s^2 + V_A^2)}{2}\left\{1 \pm \left(1 - \frac{4\omega_c^4}{k^2(c_s^2 + V_A^2)}\right)^{1/2}\right\}, \tag{1.11}$$

where ω_c is the cusp frequency defined,

$$\omega_c = k_z^2 \frac{c_s^2 V_A^2}{c_s^2 + V_A^2}. \tag{1.12}$$

The two solutions of Equation 1.11 give the fast (positive) and slow (negative) magnetoacoustic waves. In the presence of zero magnetic field i.e. $V_A = 0$, and so $\omega_c = 0$, only the fast wave exists and it is an acoustic wave driven by gas pressure. In the weak magnetic field limit, where $V_A << c_s$, the fast wave is an acoustic wave with a magnetic field component. In this case, the slow wave is a magnetic wave that is weakly affected by acoustic effects. In a strong magnetic field, $C_s << V_A$, the slow wave is an acoustic wave modified by a magnetic field, and the fast is a magnetic wave mainly driven by magnetic pressure with small acoustic affects. When there is no plasma pressure, i.e. $c_s = 0$, only the fast wave exist and is a purely magnetic wave driven by magnetic pressure. In an incompressible plasma, where the sound speed tends to infinity, the slow wave is a magnetic wave and the fast wave is an acoustic wave with infinite speed, (Goossens, 2003, p.p 141).

In a cylindrical wave-guide where the plasma is inhomogeneous, MHD waves have mixed properties. That is, a description of their properties would entail a mix of terms from the slow, fast and Alfvén waves of the homogeneous regime. This indicates the slow and fast waves are no longer strictly magnetoacoustic. However, this is not always the case. When a component of motion is negligible/ignorable the waves do not have mixed properties. In the cylindrical flux tube approximation, this is true when the motions are axis symmetric. This occurs when azimuthal wave component, n, is zero. Though, the assumption of a cylindrical flux tube is imposed for simplicity of geometry, in reality, this model may not be realistic and all modes will have mixed properties. Using again Equations 1.7 and 1.8, we can see the coupling of the incompressible and compressible modes in an inhomogeneous plasma. First, the Equations 1.9 and 1.10 are modified by the azimuthal wave number, n, and rewritten for a cylindrical system such that,

$$Y = \frac{1}{r}\frac{\partial}{\partial r}(r\xi_r) + in\xi_\theta + ik_z\xi_z, \tag{1.13}$$

$$Z = \frac{1}{r}\frac{\partial}{\partial r}(r\xi_\theta) - i\frac{n\xi_r}{r}. \tag{1.14}$$

In this case, when we evaluate the solutions as before for, $n = 0$, we obtain the equation for the compressible sausage mode, Equation 1.7, with the azimuthal component. In the $n = 1$ case, the equation for Z (rotational part) is always non-zero and so the two equations are coupled, hence mixed properties.

Starting with the Alfvén wave we shall briefly describe the nature of the waves in the flux tube regime.

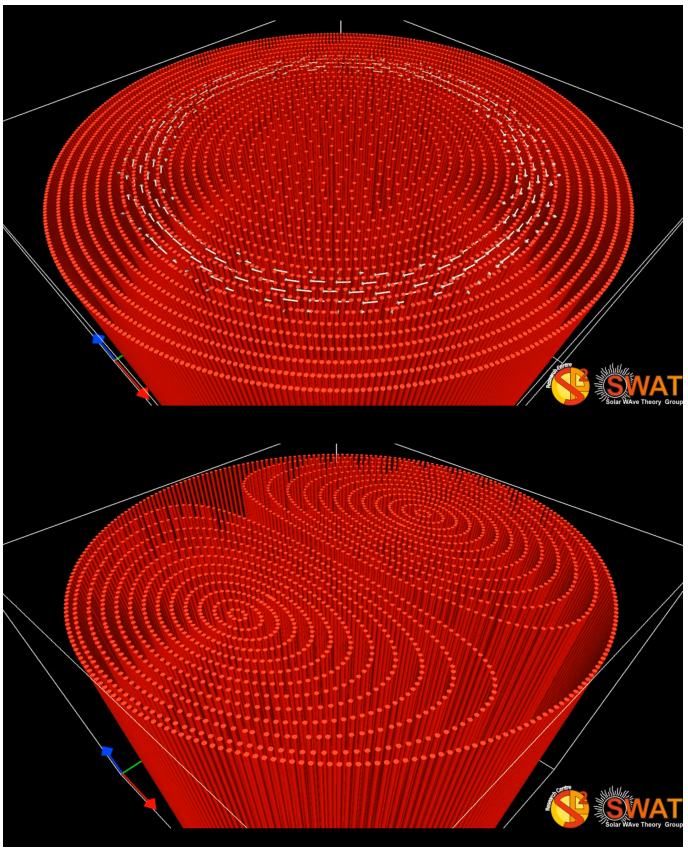

FIGURE 1.7: **Alfvén Waves.** Displayed here are flux tube simulations of; the torsional Alfvén wave, ($n = 0$) in a flux tube (*top*), and the decoupled twisting paths of the ($n = 1$) Alfvén mode (*bottom*). The parallel red lines indicate the orientation of the magnetic field and white arrows indicate the direction of motion. Image credit: (Fedun, 2014).

The $n = 0$ Alfvén wave mode in a flux tube is a twisting of the wave-guide also known as the torsional Alfvén wave, Fig. 1.7 top panel. In the $n = 1$ mode the magnetic surface is decoupled into two intricate twisting paths, Fig. 1.7 bottom panel. These torsional modes can be induced by a constant torque being applied to the wave-guide. As the torsional motion does not perturb the plasma pressure, spectral intensity or the shape of the flux tube it is difficult to observe and is only inferable by periodic motions in Doppler velocity.

The $n = 0$ azimuthal number of the fast and slow wave is known as the sausage mode. The sausage mode is a longitudinal wave mode that exhibits compression and expansion of the central axis perpendicular to the magnetic field orientation, but does not move the axis of the tube spatially. This change in tube cross section induces oscillations in plasma pressure, and hence spectral intensity. In the flux tube medium, for the sausage mode magnetic tension plays a far less significant role in the restoring forces

and the total pressure dominates, (Jess et al., 2015). To date, limited observations of the sausage-mode have been made the details of which will be discussed in subsection 1.5.4.

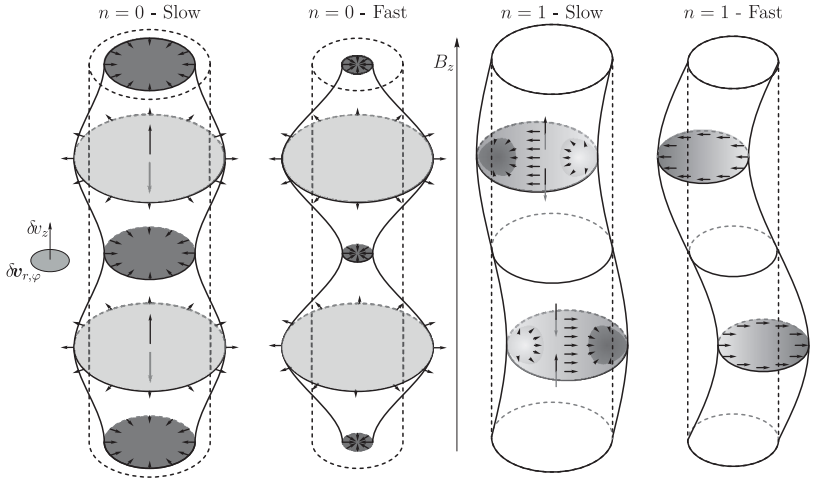

FIGURE 1.8: **Fast and Slow Magnetoacousitc Modes.** Schematic diagram of the fast and slow magnetoacoustic modes supported in a modelled cylindrical wave-guide approximating a flux tube. From left to right the slow and fast 'sausage-mode' ($n = 0$) and the slow and fast 'kink-mode' ($n = 1$) are shown. Vertical arrows within the tube show the velocity perturbations (δv_z) in the z direction. Conversely, the horizontal arrows show the velocity perturbations in the (r,φ) plane. The planar cuts along the tube show the density perturbations, higher and lower densities being with darker and brighter respectively, with respect to equilibrium. Image credit: (Jess et al., 2015).

The $n = 1$ azimuthal number of the fast and slow waves is known as the kink wave. This exhibits a transverse displacement of the central axis of the wave-guide, and as such displaces the tube spatially. In the linear and long-wavelength regime the transverse displacement has limited affect on the plasma pressure or spectral intensity inside the flux tube as the tube cross section is not altered. The kink mode has coupling between magnetoacoustic and Alfvén components, (Goossens et al., 2009). It is highly incompressible with its main restoring force supplied by magnetic tension (Jess et al., 2015) and also has a component of vorticity. This combination of incompressibility and propagation of vorticity, means the kink wave has a strongly Alfvénic nature. Figure 1.8 shows the organisation of the fast and slow, kink and sausage waves in the flux tube.

An infinite number of modes of $n > 1$ can exist and are known as fluting modes, but have not been observed in atmospheric features, possibly due to resolution limits, (Jess et al., 2015, Zhugzhda et al., 2000).

1.4.3 Wave propagation in the atmosphere

In subsection 1.2.4, we described the generation of p-modes in the solar interior, it was asserted that these waves can leak into the atmosphere and drive magnetoacoustic oscillations, (Khomenko & Calvo Santamaria, 2013). Here, we discuss the propagation

of the magnetoacoustic waves in the atmosphere and their subsequent mode conversion. Wave propagation into the atmosphere is dependant on the frequency of the wave; it is moderated by the acoustic cut-off frequency in the local environment, imposed by gravitational stratification. In this discussion, we will refer to waves with frequency above the acoustic cut-off as 'high-frequency', and those below as 'low-frequency'.

High-frequency acoustic waves, being above the cut-off frequency, easily propagate into the atmosphere. However, there does exist a scenario in which the low-frequency acoustic waves can also propagate. This is in the presence of an inclined magnetic field, the low-frequency waves are able to travel along inclined magnetic field lines like a ramp or 'magnetic portal'. The field inclination has effect of modulating the cut-off frequency by lowering it. This was demonstrated theoretically by (Bel & Leroy, 1977) and rediscovered observationally by (Jefferies et al., 2006). We describe this modulation using the following equation from (Löhner-Böttcher, 2016),

$$f_{cut} = cos(\theta_B)\frac{\gamma g}{4\pi c_s}, \tag{1.15}$$

where f_{cut} is the the cut-off frequency, θ_B is the inclination angle of the magnetic field, $\gamma = 5/3$ is the ratio of specific heats (adiabatic constant), g is the gravitational acceleration on the Sun and c_s is the isothermal sound speed. When $0° < \theta_B < 90°$ the cut-off frequency is reduced, this action is commonly referred to as the ramp effect. It is expected that areas of inclined magnetic field will show an abundance of low-frequency acoustic waves and areas of vertical field will show high-frequency waves. Perhaps a good example of this (but not the only case) can be seen in Fig. 3 of (Stangalini et al., 2011). Further examples will be shown in the context of this research in Chapter 5.

The inclusion of additional wave power from the low-frequency waves (in addition to high frequency waves) may increase the supply of energy flux and this may be particularly important in areas of strong magnetic field where convective motions are suppressed.

Magnetoacoustic waves can also undergo mode conversion, and this occurs at the equipartition layer, depicted in Fig. 1.9. The equipartition layer is where the Alfvén speed equals the sound speed ($V_A = c_s$), at this point the waves are able to transfer energy, (Cally, 2005). The equipartition layer is also approximately close to be the $\beta = 1$ layer, where magnetic pressure equals plasma pressure. In the first instance, it is possible for either conversion or transmission to occur at this level. In the case of conversion, the magnetoacoustic wave travels from a pressure dominated region, $c_s >> V_A$, as a fast-magnetoacoustic wave and converts at the $V_A = c_s$ layer to a fast-magnetic wave in the $V_A >> c_s$ region as seen in Fig. 1.9. In the case of transmission, the fast-magnetoacoustic wave travels through the equipartition layer and becomes a slow-magnetoacoustic wave,

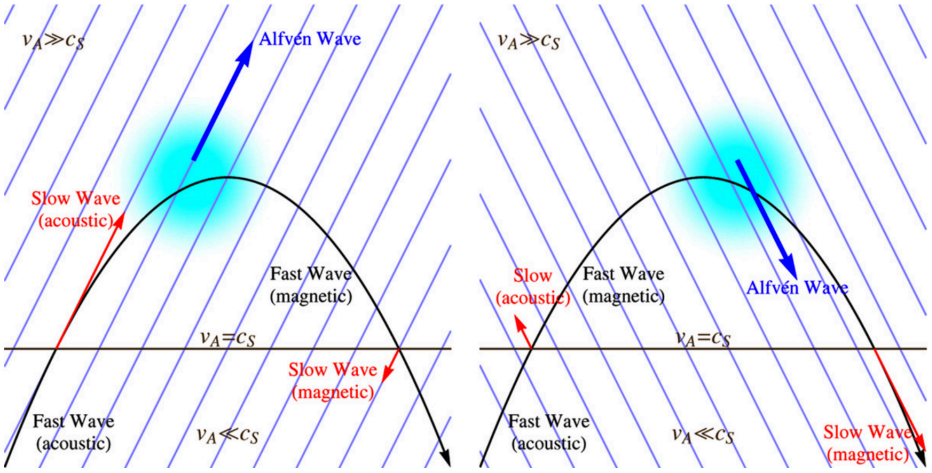

FIGURE 1.9: **Wave Propagation and Mode Conversion in the Stratified Atmosphere.** Schematic showing the fast/slow magnetoacoustic conversion/transmission at the $V_A = c_s$ equipartition level and the fast-Alfvén conversion near the transition region reflection point. The background magnetic field is shown by the blue diagonal lines, indicating their relative orientations in both panels. The arrowed lines show the propagating wave vectors. Image credit: (Khomenko & Cally, 2012).

it is now slow as it is in a $V_A >> c_s$ region. Transmission or conversion depends on the attack angle of the wave vector with the magnetic field. Transmission is favoured at small attack angles and conversion at hight attack angles, Schunker & Cally (2006, highly inclined magnetic field).

Further subsequent conversion of the fast-magnetic wave to the Alfvén wave is possible, and this occurs near curve inflection point shown in Fig. 1.9. This conversion depends on the orientation of magnetic field and incoming fast-wave vector. At this point, which is the transition region boundary, the Alfvén speed gradient is high and causes the fast-mode wave to steepen and reflect. These reflected waves can once again undergo conversion as they pass through the equipartition layer on their downwards propagation.

While on the topic of the acoustic cut-off frequency, here we will introduce a method by which the magnetic field inclination can be estimated from dependencies on temperature and the peak periods of the waves. The following is described by (Löhner-Böttcher, 2016) and is employed in Chapter 5. Equation 1.15 revealed the relationship between frequency and magnetic field. By taking the inverse we obtain an equation in terms of periods,

$$T_{cut} = \frac{4\pi c_s}{\gamma g \ cos(\theta_B)}, \tag{1.16}$$

where T_{cut} is the the cut-off period. The relation between the cut-off period and the peak-period of magnetoacoustic wave power is given as,

$$T_{cut} = 1.25 T_{peak}. \tag{1.17}$$

Substituting Equation 1.17 into Equation 1.16, replacing the sound speed (c_s) with its temperature dependent equation and finally making T_{peak} the subject we obtain,

$$T_{peak} = \frac{T_{cut}}{1.25} = \frac{4\pi\sqrt{\frac{\gamma R T_K}{M}}}{1.25\gamma g \ cos(\theta_B)}, \tag{1.18}$$

where R and M is the molar gas constant and mean molar mass respectively and T_K is temperature. Re-arranging finally for θ_B we recover,

$$\theta_B = cos^{-1}\left(\frac{4\pi\sqrt{\frac{\gamma R T_K}{M}}}{1.25\gamma g T_{peak}}\right). \tag{1.19}$$

This gives us an equation for the inclination angle dependant on two measurable quantities (T_K, T_{peak}) and a set of available constants.

1.5 Chromospheric features and observations

The chromosphere plays host to a rich tapestry of energetic fine-scale-magnetic-features (FSMF) that can act as wave-guides for MHD oscillations. Reaching speeds of 100,000 *mph* and varying on time-scales of minutes (Kuridze et al., 2013) the FSMF permeate the chromosphere, organising into ridges and spider-like patterns dictated by the magnetic field; analogous to iron filings around a bar magnet - *Hale*. The FSMF are ubiquitous and therefore worthy candidates in the story of the Sun's energy budget, (Goossens et al., 2009, Morton et al., 2012a). Examining the dynamics of the FSMF is therefore imperative to provide a comprehensive picture of how energy is transferred through the atmosphere and it is these features that are the focus of this thesis. Though the chromospheric feature nomenclature is busy, a steady set of FSMF have become prevalent in literature, these are; fibrils, spicules, mottles, RBE/RRE (rapid blue shifted/red shifted excursions) and rosettes. A description of these features and their observed oscillatory behaviour will follow, as well as some general characteristics of the chromosphere.

As described in subsection 1.2.4, the large photospheric photon flux can easily wash out the chromospheric white light and so narrow band wavelengths are needed to see the chromospheric FSMF. Strong optical and ultra-violet (UV) lines can be used for observations, however the information can be difficult to interpret, (Uitenbroek, 2006).

This is due to the non-local radiative properties, the intensity contribution functions of the spectral lines span over a range of temperatures and range of heights. This means that there is not a uniform observable atmosphere, which creates difficulties when interpreting results due to multi-height contributions to measurements. Nevertheless, the chromospheric fine structure is readily seen in the Balmer lines (e.g. H-α) and Calcium II spectral lines. As such, morphological and wave studies are often carried out in these regimes. However, for both UV and optical lines full radiative transfer models are needed to properly interpret the scene and these are difficult to compute. A detailed discussion of the H-α and Ca II spectral lines will be found in Chapter 3.

1.5.1 The internetwork

In preparation of the coming discussion, we will address some aspects of the magnetic internetwork (IN) photosphere which underlines aspects of the FSFM seen in the chromosphere. The following is adapted from (Mooroogen et al., 2017), the first paper published from this thesis. The internetwork refers to the area spanning super-granular cells, as opposed to the network areas that outline the cell boundaries marked by large flux concentrations. Making up approximately 14 % of the quiet Sun flux, the IN replenishes the network through mergers of the magnetic field as a result of flux migration possibly carried by super-granular flow, (Gošić et al., 2014, Wang & Zirin, 1988). The lifetimes of IN features vary, though typically they exist on the order of minutes with some lasting longer contributing to the network flux, (Zhou et al., 2010).

Magnetic field extrapolations that include IN field have shown that short, closed magnetic fields should be numerous (Schrijver & Title, 2003, Wiegelmann et al., 2010), however only a small a proportion make it to the corona. The strength of the photospheric IN magnetic field is on the order of $\sim 200\ G$, however kGauss features do exist, (Domínguez Cerdeña et al., 2003, Orozco Suárez & Bellot Rubio, 2012). It has been suggested by (Wiegelmann et al., 2010) that photospheric field strengths above 300 G supply around 90 % of the chromosphere's magnetic energy. Recent high-spectral-resolution Ca II H observations of active regions have potentially seen comparable low-lying magnetic fields, (Jafarzadeh et al., 2017a).

Photospheric magnetic fields are observed to be highly dynamic with small-scale magnetic elements migrating through the photosphere due to local plasma flow or supergranule flow. This was revealed by studies of magnetic bright points in G-band images (Berger & Title, 1996, Chitta et al., 2012, Nisenson et al., 2003) and flux concentrations in magnetograms, (Giannattasio et al., 2014a,b). Existing on top of the longer time-scale migrations, granular buffeting causes random motion on shorter times-scales (e.g., de

Wijn et al., 2005). These motions can excite MHD waves and in particular transverse waves, (e.g., Choudhuri et al., 1993). (Stangalini et al., 2015) presented observations in chromospheric network bright points in Ca II H (3969 Å), the evidence showed that kink waves could be excited by the granular motions. Furthermore, correspondence between the motions of photospheric bright points and transverse waves of H-α long network fibrils was shown by (Morton et al., 2013, 2014). A similar correspondence of motions were seen for prominences by (Hillier et al., 2013). Therefore, it can be suggested that waves can also be excited in the magnetic IN by photospheric velocity fields.

1.5.2 Chromospheric fine scale magnetic features

On-disk, the FSMF appear as elongated 'strands', appearing dark on the backdrop, these are known as fibrils, Fig. 1.11. The assumed geometry is of a flattened closed loop like horizontal structures with foot points connecting opposing magnetic flux, though this has not always been observed to be true, (Reardon et al., 2011). The right panels of Figure 1.11 show the photospheric magnetic field in the fibril FOV, though flux concentrations can be seen to appear around the fibrils and often correlating with bright points in the wing images (centre panels). There appears to be no structuring of field (or concentration of flux) aligned with the fibril foot points. This would perhaps suggest that the fibrils are connected elsewhere.

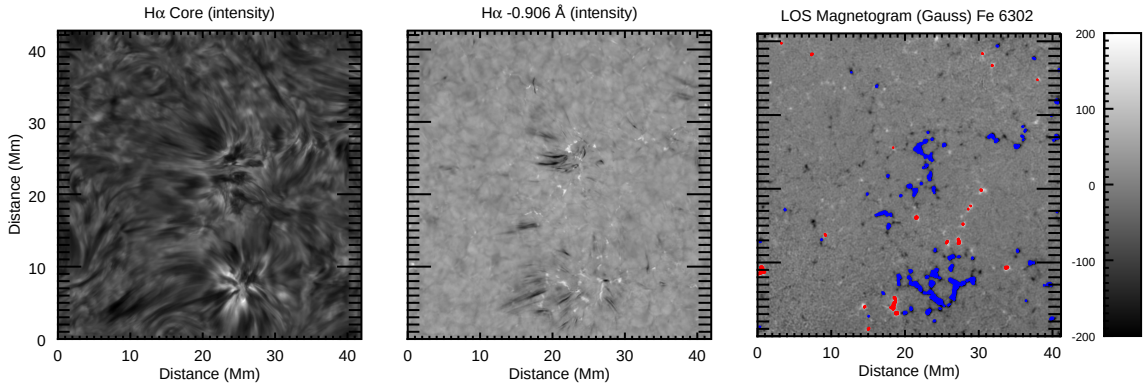

FIGURE 1.10: **Field of View of H-α Quiescent Dataset.** The left and centre panels show images of the H-α line core and blue-wing respectively. Central in the FOV of all three images are the two major magnetic flux concentrations that form part of the network and associated chromospheric rosettes. A host of fibrils can be seen in the core image (left) as the dark elongated features spanning the FOV. The photospheric magnetogram can be seen in the right hand panel, the weaker internetwork fields have been highlighted by clipping the levels to B $\sim \pm$ 200 G. The contours outline the absolute magnetic field strengths that are greater than the cut-off, red showing positive flux and blue negative. Figure recreated from (Mooroogen et al., 2017).

The features are thought to be field aligned flows of chromospheric material and appear dark due to increased column mass scattering the photospheric radiation, (Leenaarts et al., 2012). Due to the feature's field alignment the chromospheric fine structure is used as a topographical indicator of the plane-of-sky magnetic field orientation. This is reflected by the organisation of fibrils in the left panel Fig. 1.10. The fibrils span the area across superganular cells and appear strongly organised in active regions and less so in quiet regions except near the network. (Marsh, 1976) presented probably one of the earliest studies of super-penumbral fibrils. In that work, the author suggests that fibrils are the result of an 'impulsive' injection of material along a field line, and that subsequent flows result from gravity depending on the inclination. Spurred by the observation of flows and the gradual disappearance and reappearance of fibrils, this interpretation is not unlike our own, presented in Chapter 4.

Recent research has challenged the notion of field aligned fibrils. (de la Cruz Rodríguez & Socas-Navarro, 2011) in particular, brought to attention observational evidence of the partial orientation of fibrils with the magnetic field in a Ca II sunspot dataset. The authors showed that the orientation of the ordered fibril structure did not always align with the field line vector extrapolated from spectropolarimetry. The authors also suggest this could be a result of formation height difference between line core intensities and $|Q|$ and $|U|$ polarizations or that the plasma temperature structure lags behind changes in field orientation. Ultimately, the results of this paper indicated that the assumption that the fine structure traced the magnetic field in the chromosphere needs to be reconsidered and further research to be carried out. Furthermore, (Leenaarts et al., 2015) demonstrated simulations of H-α quiet sun fibrils that showed similar behaviour in intensity contrast, Doppler shift and time evolution compared to observations and oscillatory properties consistent with observed measurements. However, while the simulations showed fibrils aligned with single field lines and field line bundles they displayed examples where fibrils intersected the field at large angles but also examples where different field lines were visible at different locations along the fibril. Both of these results have significant implications for magneto-seismology and flux energy approximations where estimates are inferred based on assumptions of magnetic field geometry. Adding to this discussion on fibril-field alignment, (Asensio Ramos et al., 2017) sought to improve on the study carried out by (de la Cruz Rodríguez & Socas-Navarro, 2011) by utilising high-quality data and technical improvements. In this more recent study, the authors found no significant misalignment between fibrils and the magnetic field in the studied active region, attributing previous measurements finding misalignment to noise contributions. The study measured fibrils found in an active region containing a sunspot penumbra and two plage regions taken in Ca II. They also quote agreement with measurements of alignment performed by (Schad et al., 2013) from Helium I super-penumbral observations.

(Rutten & Rouppe van der Voort, 2017) proposed a new interpretation of an RBE event that suggested a hot bullet trail leading to the onset of fibril formation. This was presented via the observation of an RBE seen in the blue-wing of H-α and the corresponding delayed emergence of a fibril in the line core. The author recognises that the ubiquity of such an event is yet to be determined and currently only conjecture of the heating precursor could be made. Though there is no general consensus on the formation of fibrils as of yet, examples such as these cause us to cautiously re-evaluate how we interpret wave phenomenon while researching these features. Further details of fibril properties are presented in Section 1.5.4.

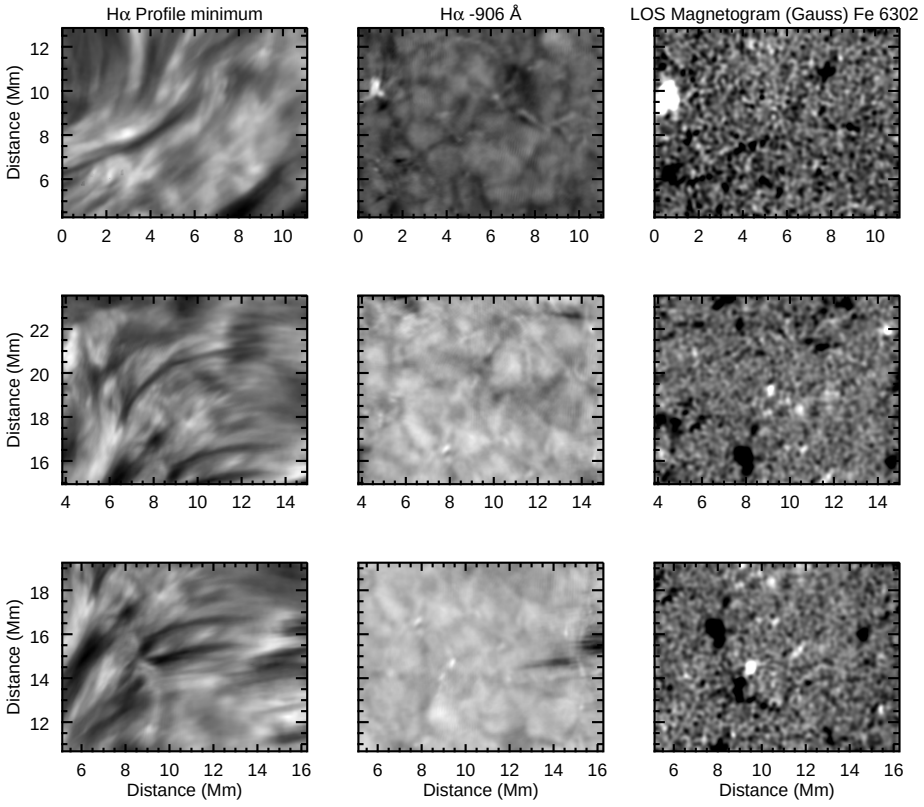

FIGURE 1.11: **Examples of Internetwork Fibrils.** The left hand column displays isolated fibrils in intensity images resultant from the profile minimum. The middle panels show the corresponding blue wing images at the photospheric level, the last column shows the photospheric magnetic field strength clipped between $\pm$ 50 G. Image recreated from (Mooroogen et al., 2017).

Viewed from the limb, FSMF can appear bright without the contrasting atmosphere and features that appear nearly vertical are known as spicules, Fig. 1.12. These are chromospheric plasma guided by near-vertical open magnetic flux, and they are best seen on the limb and occur at network boundaries. In contrast to fibrils, spicules appear to have have one foot point rooted in chromosphere and the other seemingly reaching into the higher atmosphere. Cross-height examinations of these features have shown their inter-connection across different layers of the atmosphere. This has been established via

correlations of chromospheric features with photospheric field concentrations and bright points found in inter-granular lanes, (Judge, 2006).

Spicules are split into two categories type I and type II. (De Pontieu et al., 2007a) describe type I spicules as dynamic on time-scales of 3-7 minutes and exhibit upward and downward motions. The authors note that spicules type I share similarities to dynamic fibrils and quiet sun mottles, and so are thought of as the at limb counter part to those features. These similarities are highlighted by the near identical linear correlation between deceleration and maximum velocity as compared to those expected for dynamic fibrils/mottles. Type I spicules appear regularly in active sun limb regions but not as frequently in coronal holes and the quiet sun. (De Pontieu et al., 2007a) describe spicule type II as dynamic, with speeds of 50-150 $km\ s^{-1}$, having lengths between 1000-7000 km and lifetimes between 10 and 60 s. These speeds are significantly higher than those of type I which do not reach velocities more than 40 $km\ s^{-1}$. Type II spicules are shorter in active regions and longer in the quiescent sun with lengths on the order of Mm to several Mm respectively. In contrast to type I they dominate coronal holes regions but like type I spicules exhibit transverse motions.

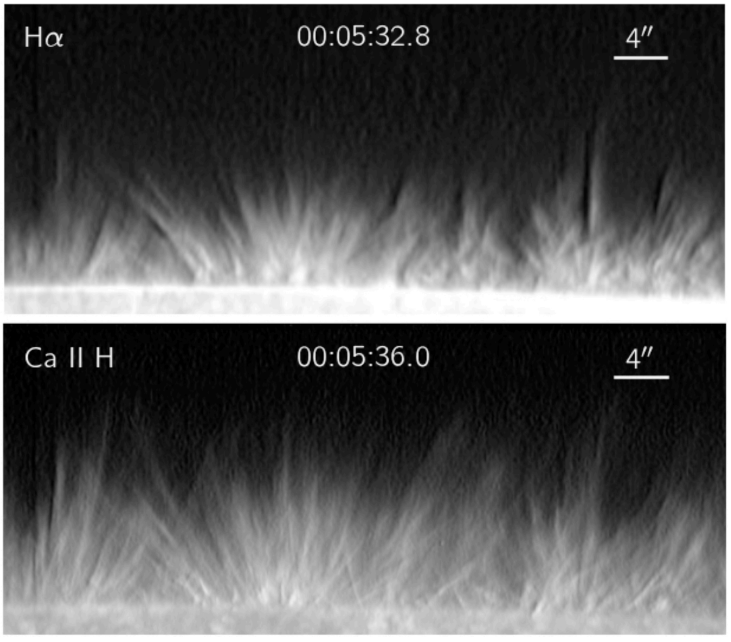

FIGURE 1.12: **Spicules on the Solar Limb.** Spicules seen on the solar limb from SOT polar observations, the top panel shows the sum of the red and blue channels of the H-α filtergram, the bottom panel depicts Ca II H filtergram. The fine-scale elongated structure can be seen and the spicules appear bright without the solar background. Image credit: (Pereira et al., 2013).

(Pereira et al., 2012) lead a significant statistical investigation of spicules in coronal holes, quiet sun and active regions. The study presented statistically significant results that confirmed the qualifying of spicules as type I and II consistent with the assertion of (De Pontieu et al., 2007a). They showed measurements of linear (type II) spicules

TABLE 1.1: Average (or measured) properties of fast kink-waves (Jess et al., 2015)

Structure	Region	ξ (km)	P (s)	v (km/s)	c_{ph} (km/s)	No. Events	Reference
Spicule	CH	$200-500$	$150-350$	20 ± 5	-	95	(De Pontieu et al., 2007b)
	CH	-	$60-240$	20 ± 5	-	-	(Kubo et al., 2008)
	CH	1000	130	15	460	1	(Kim et al., 2008)
		700	180	8	310	1	
		800	170	9	260	1	
	CH	36	48	4.7	75-150	1	(He et al., 2009a)
		36	37	6.1	59-117	1	
		130	45	18.1	73	1	
		166	50	20.8	109-145	1	
	CH	55 ± 50	45 ± 30	7.4 ± 3.7	160-305	89	(Okamoto & De Pontieu, 2011)
		600	180	22	-	1	(Ebadi et al., 2012)
	QS	670	220	19.2	-	1	(Jess et al., 2012)
		630	139	28.3	-	1	
		160	65	14.8	-	1	
		410	158	16.2	-	1	
		380	129	18.5	-	1	
		200	105	11.8	-	1	
		190	171	7.2	-	1	
	AR	283 ± 218	–	14 ± 112	-	112	Type-I -(Pereira et al., 2012)
	AR	463 ± 402	–	18 ± 12	-	58	Type-II
	QS	245 ± 211	–	16 ± 11	-	174	
	CH	342 ± 257	–	20 ± 12	-	170	
Fibrils		135	135	1	190	1	(Pietarila et al., 2011a)
	QS	315 ± 130	–	6.4 ± 2.8	50-90	103	(Morton et al., 2012a)
	QS	71 ± 37	94 ± 61	24.5 ± 1.8	-		(Morton et al., 2013)
	QS	94 ± 47	116 ± 59	5.5 ± 2.4	-	841	(Morton et al., 2014)
	AR	73 ± 36	130 ± 92	4.4 ± 2.4	-	744	
RBEs		300	–	8	-	35	(Rouppe van der Voort et al., 2009)
	CH	200	–	$4-5$	-	960	(Sekse et al., 2012)
	QS	200	–	8.5	-	1951	average - (Sekse et al., 2013a)
		220	–	11.7	-	1951	maximum

Table adapted from (Jess et al., 2015).

occurred mostly in coronal holes and quiet regions where as the parabolic (type I) rarely occurs there but more prevalent in active regions. Typical properties of type I spicules were measured as; 150–400 s lifetime, maximum ascending velocities of 15–40 $km\ s^{-1}$, maximum heights of 4–8 Mm, inclinations of 0–40 °, scale heights of 1.5–2.5 Mm and maximum transverse speeds of 5–30 $km\ s^{-1}$, (Pereira et al., 2012). Of type II spicules; much shorter lifetimes of 50–150 s, ascending velocities of 30–110 $km\ s^{-1}$, maximum heights of 3–9 Mm, inclinations of 0–30 °, scale heights of 1.8–3 Mm in the quiet Sun and 2.4–3.6 Mm in coronal holes and maximum transverse speeds of 4–40 $km\ s^{-1}$, (Pereira et al., 2012).

RBE's or rapid blue-shifted excursions (also RRE's rapid red-shifted excursions) are apparent fast moving moving streams of plasma seen in the blue wings of chromospheric spectral lines. However, the origins of the structures are not entirely clear. Similarities to the properties of type II spicules have led the suggestion that RBE's may be the disk counter part of type II spicules, (Langangen et al., 2008, Rouppe van der Voort et al., 2009). Table 1.1 shows the comparative properties for these features, as previously studied.

1.5.3 The chromosphere revisited: Quiescent H-α and Ca II 8542 Å

The research in this thesis is focused on measurements of fibrils and in the context of describing the chromosphere, we will take the opportunity to present the scene of the two datasets used in this study. Details of the spectral line formation of H-α and Ca II 8542 Å and the creation of the data products will be discussed in Chapter 3. The data products themselves, will be presented in more detail in Chapters 4 and 5.

The following description of the quiescent chromosphere from the H-α dataset used in this research is adapted from (Mooroogen et al., 2017). Figure 1.10 shows the observed FOV of the quiescent H-α chromosphere visibly dominated by fibrils, the fine-scale structure that perpetuates the FOV principally originate from the network regions. Long fibrils fanout around these regions with distinct structuring forming two distinct rosettes; these are the two central features in the left panel of Fig. 1.10 that the dark features appear to emanate from. In the context of this research we refer to the regions situated within the rosettes as the network, where field strength is strongest in the FOV and areas away form this region as the internetwork. Spicules can be observed directly over the network with a near perpendicular orientation to the surface. In the photosphere, which is revealed by the H-α wing and Fe magnetogram (centre and right panel, Fig. 1.10) two distinct regions of negative polarity, kilogauss magnetic fields can be seen (blue in the magnetogram). These field concentrations are correlated with the rosettes in the line core and wing images and are likely part of the magnetic network. In the photosphere, clusters of bright points highlight this network and the H-α line core images suggest that the network has a strong influence on the visual appearance of the chromosphere, similar to those seen in (Jess et al., 2012). Surrounding the network areas there appear to be patches of small-scale magnetic flux a small number of which have $|B| > 200\ G$.

From the rosettes in the network, fibrils extend out radially to approximately 10-15 Mm into the internetwork (areas away from the rosettes in the this context). However, this is not seen in the areas with shorter fibrils and strong positive field. Numerous in the internetwork areas are extended curvilinear features that are relatively long lived (>200 s) in the time sequences, these will referred to as the internetwork fibrils (IN fibrils). Evident throughout the time series data, the IN fibrils appear, disappear and re-appear in approximately the same location over time and follow the same apparent path. This behaviour would suggest the constancy of a magnetic field, and the changes in the fibrils visibility may be a result of variations in the H-α opacity. These long-lived IN fibrils are not dissimilar with the motion speed of photospheric IN magnetic elements, (Wang & Zirin, 1988, average speeds of $\sim 0.2\ km\ s^{-1}$).

The visual appearance and behaviour of the IN fibrils are similar to those that reach out from the network. This suggests that these features are dense plasma that outline the IN magnetic fields. If the IN fibrils do in fact trace the magnetic field, then the elongated shape implies that the field is relatively low lying in the atmosphere. Unlike the near-vertical features e.g. spicules, that reach into the corona and have limited inclinations from the vertical (Pereira et al., 2012, Tsiropoula et al., 2012), this scenario would correlate with the magnetic field extrapolations of (Wiegelmann et al., 2010) that suggested that low-lying loops would dominate the IN. However, it is possible that the IN fibrils curvilinear appearance is in the 'plane' of the chromosphere; in other words, the apparent sections of the fibrils are horizontal and wind through the chromosphere. Though from visual inspection of the dataset it is near impossible to tell if this is the case.

The fibrils presented in this dataset have behaviour that is reminiscent of slender Ca II H fibrils observed in an active region, reported from the balloon-borne SUN-RISE data, (Gafeira et al., 2017b).

Fig. 1.13 shows the FOV of the Ca II 8542 Å sunspot dataset; much like the H-α dataset, a host of fibrilar features with large opacity can be seen in the line core image, top left panel. These are predominantly noticeable in the super-penumbra fan out in a radial pattern from the umbra for 10-15 Mm. These fibrils that reach from the umbra appear over the penumbral region (seen in the wing images), but then continue for approximately another 5 Mm before tapering off, into where the inter-granular bright points can be seen in the photospheric images. However, another series of fibrils, with weaker relative intensity, can be seen in the area outside of the penumbral regions - at the edges of the FOV. In the Ca II blue-wing (top right panel), we see the sunspot in the photosphere, here we can clearly see the irregular shape of the umbra. The sunspot umbra is split into three parts by a light bridge, this structure is clearly seen in the photosphere and also in the line core images. Noticeable in the time-series movies are umbra flashes caused by acoustic waves shocking as they propagate along the vertical field in the sunspot umbra. This can been seen in each of three umbral structures. Radially from the centre, running penumbral waves can also be deduced. These penumbral waves appear to emanate from each umbra section and push out into the penumbra, where as in reality they are the manifestations of upward propagating magnetoacoustic waves that occur in successive wave fronts, (Bloomfield et al., 2007). The penumbra in the photosphere appears to reach out approximately 10 Mm from the umbra edge, and disappears sharply. The photospheric granular pattern is readily visible, and between the cell boundaries, bright intensity enhancements, signatures of strong magnetic field can be observed.

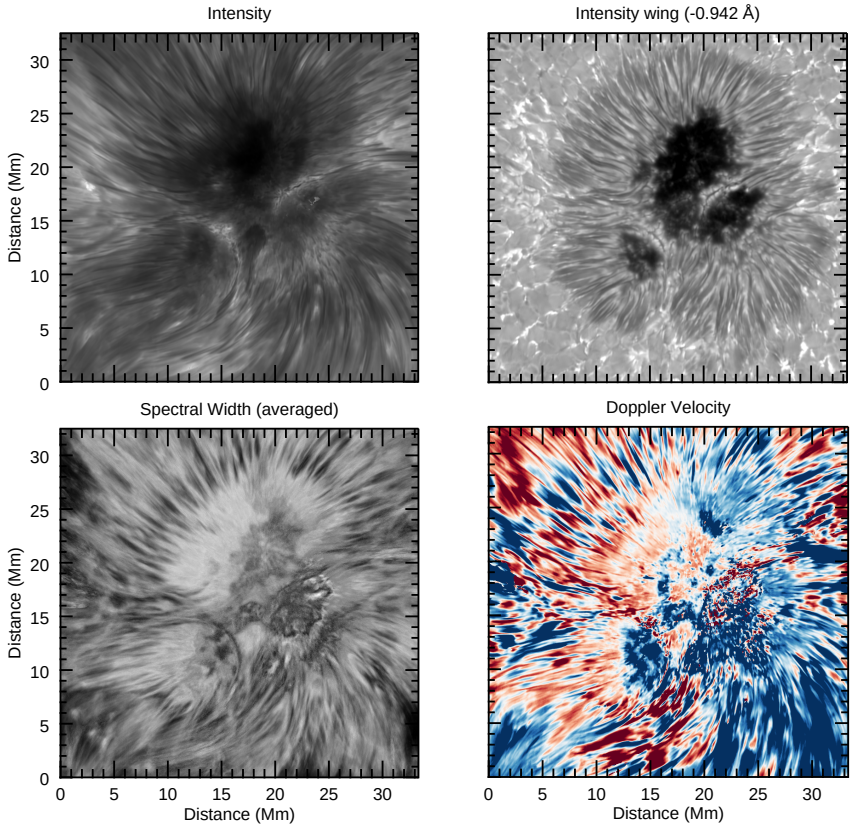

FIGURE 1.13: **Ca II 8542 Å Sunspot Dataset.** The top two panels show intensity data for the line core and blue-wing from left to right respectively. A host of fibrils can be seen in the in chromospheric super-penumbra fanning out radially around the sunspot centre. The lower two panels from left to right, show averaged line width and Doppler velocity data products made from least squares fitting of the spectral profile data. The width and Doppler components of the fibrils can be seen in both data product images.

The fibrils seen in the line core super-penumbra are not aligned with penumbra as seen in the photosphere, instead the fibrils in the bottom section of the FOV tend to a curvilinear path and the fibrils in the top section are somewhat along the radius of the sunspot. The existence of the super-penumbra is independent of the penumbra, in fact pores without penumbra can exhibit super-penumbral fibrils as seen in the pores studied in, (Chae et al., 2014). In that study the authors conclude that shocks from umbral oscillations are physically related to the fibrils as they observe a pattern of shock fronts that stop at the base of fibrils, this is something that is also noted in our Ca II dataset.

The fibrils apparent in this dataset, like the H-α IN fibrils described earlier, show temporal evolution that remains spatially localised even after disappearance and reappearance.

The magnetic field topological model of a sunspot is as follows, in the umbra large vertical flux tube concentrations cause a strong magnetic field, the vertical flux tube expands

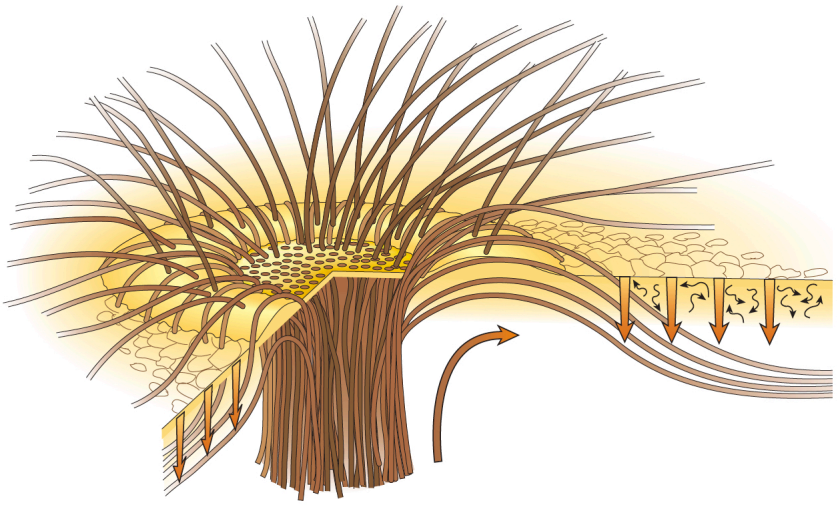

FIGURE 1.14: **Sunspot Cross-Section.** Cartoon showing a cross section of a sunspot, the magnetic field orientation is indicated by the layout of the field lines seen as the dark strands. The bundle of strands bellow the surface create the large magnetic flux that causes the umbra. Granular patterns indicating the convection motion are shown outside the sunspot umbra to indicate that convection is suppressed under the umbra. Image credit: (Thomas et al., 2002).

with the stratified atmosphere and becomes more inclined in the penumbral regions, as seen in the cartoon, Fig. 1.14. In the chromosphere and corona the sunspot dynamics are controlled by the magnetic field, in the corona one finds coronal loop structures situated over the sunspot regions and in the chromosphere the super-penumbral fibril fine-scale structuring.

Much of the observations and research into oscillations found in the sunspot chromosphere has been focused on magnetoacoustic oscillations. However, the first observations of the transverse kink wave evident in the super-penumbral fibrils will be presented in Chapter 5 of this thesis.

1.5.4 MHD wave observations

The review by (Jess et al., 2015) presents a detailed account of the history of wave studies in the chromosphere. A succinct version is provided here.

Highlighted in Section 1.3, oscillations have been detected in the Sun's atmosphere since the 1960's. (Leighton et al., 1962) and (Noyes & Leighton, 1963) observed periodic variations in intensity and velocity fields in the photosphere and lower chromosphere. These were interpreted as signatures of acoustically driven waves with periods of five minutes. Following these early papers a series of subsequent studies, listed in (Jess et al., 2015) e.g (Deubner, 1975, Schmieder & Mein, 1980, Ulmschneider, 1976, White

& Athay, 1979a,b), revealed upward propagating waves in the chromosphere but their energy flux was unable to account for the radiative losses in the chromosphere.

P-modes originating from the interior can easily leak into the atmosphere and perturb the plasma at the Sun's surface (Khomenko & Calvo Santamaria, 2013) and this energy can be transferred to features in the atmosphere that then act as wave-guides. However, there has been debate on whether high frequency magnetoacoustic waves ($>5\ mHz$) have sufficient energy to heat the atmosphere. (Fossum & Carlsson, 2006) and (Carlsson et al., 2007) presented Transition Region and Coronal Explorer (TRACE) observations that suggested that the high-frequency waves did not have sufficient power to heat the chromosphere. This was contested by (Cuntz et al., 2007), who cautioned the comparison of TRACE observations to models, it was pointed out that the resolution of TRACE was too low relative to the 'hot pockets' evident in the simulations and so was underestimating the energy flux. More recent results from (Bello González et al., 2009) and (Bello González et al., 2010) found acoustic wave flux of at least three times that of (Fossum & Carlsson, 2006) and (Carlsson et al., 2007). However, the authors acknowledged that these values were still unable to fully balance the radiation losses, they considered the wave power sufficient to provide a 'warm' internetwork chromosphere. The authors also note that they measure wave flux at frequencies below that of the acoustic cut-off.

Naturally, a push to high-resolution experiments ensued and a number of studies revealed significant high-frequency magnetoacoustic power in the lower chromosphere (Bello González et al., 2009, 2010, Solanki et al., 2010), this was concurrent with examination of smaller-scale features, magnetic bright points or MBP. (McAteer et al., 2003) provided evidence of upward propagating waves from the photosphere into the upper chromosphere in MBP's. (Bloomfield et al., 2004); (Vecchio et al., 2009) and others showed that high-frequency upward-propagating waves could cause shock heating of the plasma. Though it had been shown earlier that most shocks resulted from the interface with downward flows in the mid chromosphere, later work suggested that these shocks could potentially be exciting incompressible waves through the mass loading of magnetic fields, (e.g., Cauzzi et al., 2008, De Pontieu et al., 2004, Kuridze et al., 2013, Rouppe van der Voort et al., 2007).

(Beck et al., 2009, 2012, 2013a,b) were able to show that sub-arcsecond resolution observations of small-scale magnetic elements exhibiting magnetoacoustic energy lacked significant power at chromospheric heights to sustain heating. These results appear to confirm what previous studies have shown, that currently our measurements suggest that acoustic waves alone cannot provide sustained heating in the chromosphere. Although, (Liu et al., 2014) suggested that the many fine-scale structures, spicules, etc; showed

superposition of both upward and downward propagating waves, and thus studies that aim to estimate wave energy may be underestimating the flux.

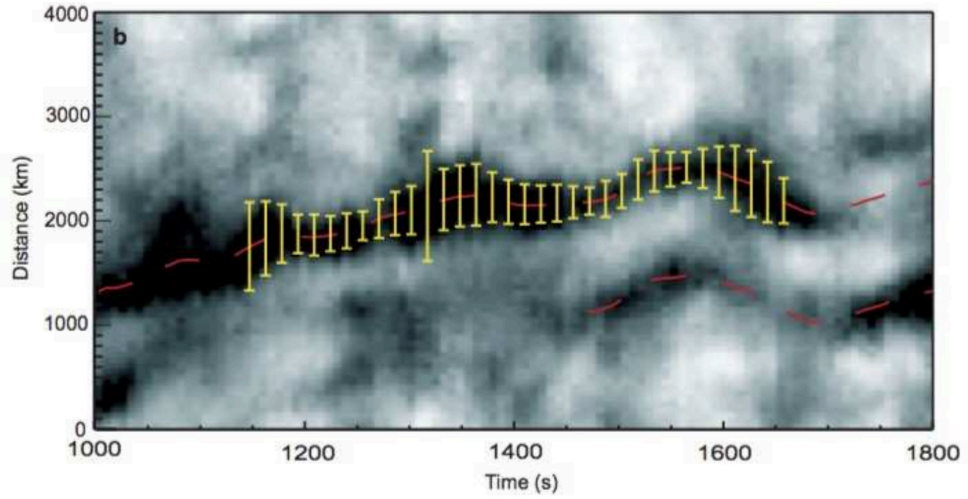

FIGURE 1.15: **Observational Evidence of the Sausage Mode.** Time distance diagram of fibrils in a quiescent H-α observations. The quasi-periodic compression of the central axis of the feature can be seen, indicating the sausage-wave. Over-plotted is the tracked central axis (red curve) and the yellow bars show the estimated width of the structure. Image credit: (Morton et al., 2012a).

Thanks to the development of high spatial resolution instruments, the observation of the sausage mode (a compressible mode) in the chromosphere has been made possible. (Morton et al., 2012a) studied H-α images of fibrils and mottles with the Rapid Observations of the Solar Atmosphere (ROSA) instrument on the Dunn Solar Telescope and found evidence for sausage modes along side kink modes in numerous structures. The work provided a rudimentary estimate of the phase speed of the sausage modes on par with the Alfvén speed, suggesting that the observation was of fast sausage waves. Further analysis revealed that the sausage modes fell within the 'leaky' regime meaning that they were able to radiate energy from the structure, this was characterised by the ka number, which is the product of the wave number (k) and the wave-guide half width (a). This is a dimensionless property that details whether wave energy is 'trapped' without the presence of external damping method. Coupled with the significant amount of energy estimated for individual waves, $\sim 11700 \pm 3800\ Wm^{-2}$ (Jess et al., 2015) sausage waves, at least in the context of that study, present themselves a suitable candidates for local heating. With photospheric imagery, (Morton et al., 2012a) showed evidence of MBP's being possible anchors for the wave-guides supporting the discovered kink and sausage waves. Later work by (Jess et al., 2012) reinforced this idea with findings of mode coupling between compressible and incompressible wave modes in MPB and connected spicules. The authors compared the observations with 2D simulations and found consistent results.

So far we have introduced the first sightings of wave modes in the solar atmosphere in the form of magnetoacoustic waves and have highlighted the important but limited research of the sausage wave and its potential for atmospheric heating. Now we will introduce observations of highly incompressible waves found in the chromospheric fine-scale features.

Observations by (De Pontieu et al., 2007b) made with the Hinode/SOT instrument of the Ca II H line revealed the transverse motion of spicules in time-distance diagrams. The authors reported that the majority of spicules exhibited transverse displacements on the order of 500-1000 km, on time-scales of 10-300 seconds. The authors also state that long lived features showed signs of oscillations. The authors wrongly identified these as Alfvén waves, which of course are torsional in an inhomogeneous atmosphere as discussed earlier, and should then show periodicities in the Dopplergrams. This led to gross over estimation of the energy flux they were able to transport at 4000-7000 Wm^{-2}. Revisions to this research by (Van Doorsselaere et al., 2014) under the kink wave interpretation led the flux to be reduced 200-700 Wm^{-2}. However, the newer value itself is underpinned by mathematical assumptions of the density filling factor, that is the the ratio of flux tube (wave-guide) volume to the volume of space occupied by the flux tubes.

Further studies of spicules (He et al., 2009a,b, Okamoto & De Pontieu, 2011, Suematsu et al., 2008), revealed further examples of transverse motions with (Suematsu et al., 2008) showing some evidence of rotational motion and increasing amplitude with height in the atmosphere. This result indicated a decrease in plasma density with height, which was to be expected with atmospheric models. (He et al., 2009a) was able to measure waves with periods of < 50 s and utilised cross-correlation to measure propagation speeds between 59-150 $km\ s^{-1}$. This study also reported the increase in amplitude with height consistent with, (Suematsu et al., 2008). (He et al., 2009b) provided a detailed observation of individual spicules and showed an unexpected low value for the phase speed with height (25 $km\ s^{-1}$) that suggested a weakening of magnetic field. (Okamoto & De Pontieu, 2011) produced a substantial study of eighty-nine spicules in a coronal hole, the measured average properties of period were 45 ± 30 s and velocity amplitudes of 7.4 ± 3.7 $km\ s^{-1}$. These results suggested that the waves carry less energy than estimated by (De Pontieu et al., 2007b). The authors note that the majority of the waves were upward propagating, and show the observation of the superposition of upward and downward propagating waves, this was falsely interpreted as standing waves. Superposition of oppositely directed waves is one manner in which standing waves can be created but the defining feature of a standing wave is fixed nodes that do not oscillate.

(Jess et al., 2012) presented observations of on-disk H-α spicules and highlighted potential driving mechanisms for the observed transverse oscillations. In this work the authors suggest that kink waves in type I spicules are the result of mode conversion in the lower atmosphere. This result is concluded after comparison of observations with 2D MHD simulations and the authors further suggest that these waves are significantly energetic. (De Pontieu et al., 2012) presented evidence for torsional waves found in type II spicules in the form of oppositely directed Doppler shifts. However this result has been contested, (Goossens et al., 2014), it is also possible that the Doppler signatures are line-of-sight components of the kink wave. While the kink wave has torsional components it is not the pure torsional wave as reported.

Observations of fibrils made by (Pietarila et al., 2011a) found transverse displacements with velocity amplitudes significantly less (on the order of 1 $km\ s^{-1}$) than found in spicules. A rudimentary measurement of the phase speed approximated it at 190 $km\ s^{-1}$ however the authors note this value is subject to large uncertainties. (Morton et al., 2012a) provided a statistical analysis of fifty H-α fibrils, showing ubiquitous transverse oscillations. The authors report a mix of uni-directional and sinusoidal motions in the studied fibrils, estimates of the propagation speed revealed upward and downward propagating waves on the order of 50-250 $km\ s^{-1}$. Measurements of displacement amplitude appeared to be smaller relative to those found at the limb, i.e. spicules.

(Morton et al., 2013, 2014) made use of an advanced tracking and fitting code (Northumbria University Wave Tracking code, Morton & Mooroogen, 2016, to analysis hundreds (> 700) of examples of fibrils in H-α active and quiet regions. In these extensive works it was possible to constrain the properties of the transverse waves at an unprecedented scale. The results of the measured parameters can be seen in Table 1.1. It was shown that the mean measured displacements and velocity amplitudes were smaller than previous measurements though the authors recognise that the extremities of high and low frequency measurements will be restricted by spatial and temporal resolutions of the observation and fibril lifetime respectively. As a consequence of the large number of measured fibrils, it was possible to establish the first velocity power spectra for chromospheric transverse motions. This was compared to similar photospheric spectra from granular flows as a novel method of examining the propagation of MHD waves in the atmosphere. The comparison revealed good correlation of low-frequency gradients suggesting that the granular motions were playing a significant role in the driving of the waves. Furthermore, (Morton et al., 2013) were able to show evidence for vorticity in strong photospheric flux concentrations. It was then shown that these vortices are able to excite torsional motions in the chromosphere that were observed to be periodic, rotating one way then the other in velocity vector plots. There torsional waves were subsequently seen to excite transverse motions in the chromosphere.

(Gafeira et al., 2017b) presented a quantitative study of the morphology of fibrils in Ca II H using the Sunrise II balloon. The observations covered a developing active region across a polarity inversion line. Using a series of automated methods the authors were able to measure the length, width, curvature, lifetime and brightness of 598 structures. Typical lengths were measured at 0.5-4.5 Mm, widths at 100-270 km, lifetimes between one minute to half an hour (taking into account the intermittent visibility). They identify that the fibrils have a varied distribution of curvature with gradual preference towards positive curvature. Interestingly, it was noted that there were two types of morphology in brightness; one scenario where brightness begun in the centre of the feature and spread out, the other where it begun at one or both ends and grew towards the centre. The lengths measured in this study appeared to be considerably shorter than that of spicules, however the authors note that this could be a selection bias but also that their automated technique likely underestimates the fibril length.

To this date there have been limited studies of fibrils, and attention tends more towards spicules with the ambition that their seemingly open field reaches into and connects in the corona. Nonetheless, fibrils are important in the discussion of atmospheric heating due their ubiquity in both quiet and active regions in the chromosphere.

Finally, we turn to talk briefly on the topic of MHD oscillations in RBE's. (Rouppe van der Voort et al., 2009) analyses thirty-five RBE events that exhibit transverse displacements and find displacement amplitudes are measured to be 0.3 Mm and velocity amplitudes 8 kms^{-1}. Larger studies by (Sekse et al., 2012, 2013b) showed similar measurements and little difference in the properties between H-α and Ca II 8542 Å spectral lines. They also found that the uni-directional RBE's had larger velocity amplitudes than periodic ones.

Kuridze et al. (2015) embarked on a study into RRE's (rapid red shifted excursions) and sought to compare them to RRB's in the H-α chromosphere. It was found that they occurred independently though with similar lifetime, length, width and occurrence rate. The authors also report the oscillations were transverse in nature but highlight the difficulty to report on the periodicity of the features due to their lifetimes being much shorter than the typical kink wave lifetime. Kuridze et al. (2015) described the oscillations as non-linear transverse waves, the motion is in one direction and continues in that direction until the feature disappears.

Recently, there have been observations revealing signatures of RBE's found in the transition region, (De Pontieu et al., 2011, Rouppe van der Voort et al., 2015), suggesting they have potential for heating through the atmosphere. (Henriques et al., 2016) describes statistical confirmation of H-α small scale transients i.e. RBE'S being linked to heating events in the transition region.

With the relevant background information established we move onto Chapter 2 where the instruments used in this study will be described. In Chapter 3 we will detail the data, observations, data uncertainties and data products. In Chapters 4 and 5 the body of the two research methodologies and results will be presented. Finally, in Chapter 6 a summary of the results is highlighted and scope for further work is outlined.

2

Instrumentation and data acquisition

In this chapter we will look at the instrumentation used to acquire the data for this research and the calibration methods employed. Furthermore, we will explore how spectroscopy enables the observation of specific heights in the solar atmosphere and how we can derive physical quantities from the polarisation of light. The primary data used in this research was taken with the Swedish Solar Telescope (SST) utilising the CRisp Imaging SpectroPolarimeter instrument (CRISP). In addition this study is supported with observations made with the Solar Dynamics Observatory (SDO) Helioseismic and Magnetic Imager (HMI).

FIGURE 2.1: **The SST.** The Swedish Solar telescope as seen from outside at Muchachos Observatory. Image credit: (IAC, 2017).

2.1 The Swedish Solar Telescope and the CRisp Imaging SpectroPolarimeter

2.1.1 The Swedish Solar Telescope

The Swedish Solar Telescope is one of the largest, high-resolution solar telescopes in the world, situated at the Roque de los Muchachos Observatory, La Palma, Canary Islands. At at a height approximately 2400 m above sea level, where atmospheric effects are reduced, the telescope resides in a seventeen metre high tower, Fig. 2.1, (de la Cruz Rodríguez et al., 2015). This site is regarded as one of the best locations for solar observations worldwide. The SST combines high quality optics, adaptive optics and advance image restoration techniques to produce some of best quality datasets available. The SST optical system has a resultant spatial sampling of 0".0592 per pixel or 52 km per pixel.

The SST is a one metre, refractive, vacuum-telescope that makes use of a Schupmann corrector system that corrects for chromatic aberrations caused by the singlet lens (Scharmer et al., 2003). A vacuum-telescope is evacuated internally, this ensures that turbulent motions of air inside the optical tube do not affect the image. Vacuum telescopes however are limited by the practical size of the vacuum window that can be placed into the telescope. This is the window that seals the vacuum to the outside air. This window must be polished to extremely high optically quality, however this is hindered by the fact the the window must also be thick enough to withstand the pressure differential between the air-side and vacuum. Therefore, a larger aperture will mean a larger vacuum volume, which in turn will rely on a thicker window. This then limits vacuum telescopes to an aperture of approximately 1 m, (ISF, 2002). In the SST, the primary singlet lens acts as the vacuum window to ensure the high optical quality. Some telescope systems overcome this issue by using helium filled optical tubes as opposed to a vacuum. This set up allows for a greater aperture size while maintaining reduced turbulent effects by air in the tube however, not to the same quality as a vacuum set up. For larger aperture telescopes, open-air tubes are used with advanced temperature control optics.

Air turbulence is particularly important in solar telescopes where significant heat is generated by the mass collection of sunlight, this heat will in turn cause turbulence in the air in the telescope. For instance, at the SST the 700 W of solar heat is transferred through the 1 m collector and focused onto a 18 cm image - just like a magnifying glass. This equates to a substantial heat load of 30 kWm^{-2} (Scharmer et al., 2003). Thus, it is also necessary to include efficient cooling systems and in this case the SST

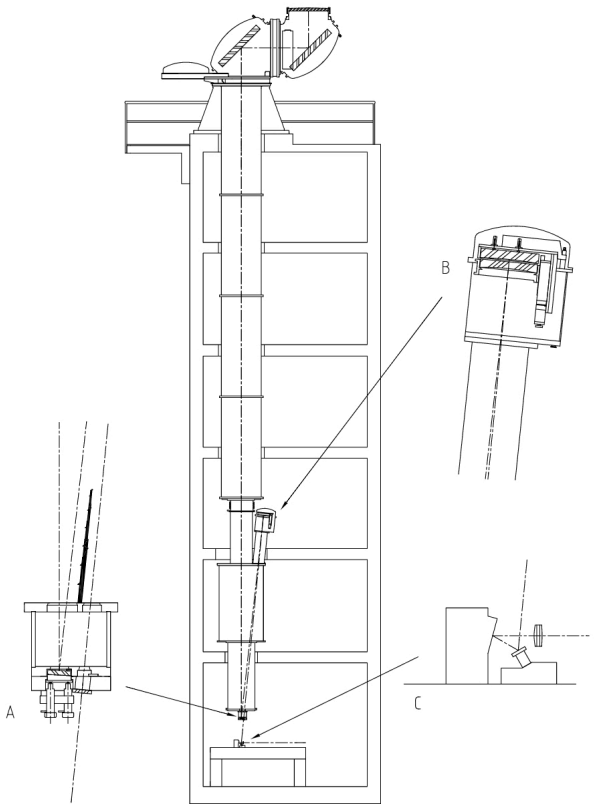

FIGURE 2.2: **The SST Schematic.** Schematic diagram of the SST vacuum tower. The turret and primary aperture can be seen at the top of the tower. Labelled at A is the location of the field lens and mirror, at B the re-imaging optics and finally at C the adaptive optics, re-imaging mirror and tip-tilt mirror on the optical table. Image credit: (Scharmer et al., 2003).

uses a water cooling system that maintains temperatures external of the vacuum do not exceed 35 °C. In addition to the cooling system, the SST makes use of adaptive optics to further reduce exterior atmospheric effects on the image quality, this system is made up of a deformable mirror and a wave-front detector. The wave-front detector measures the distortions in an image caused by atmospheric disturbances. Then, by applying a voltage at specific locations across the surface of the mirror, its shape can be altered thus accounting for the distortions.

The SST uses a fused silica lens for its primary optical system, the choice of this material was due to its low coefficient of thermal expansion. This essentially means that the lens does not respond significantly to heating during observations, relativity speaking (Scharmer et al., 2003). The telescope also makes use of stiff turret bearings to ensure controlled pointing. Figure 2.2 shows the optical set up of the SST, the objective lens is found on top of the tower at the opening and the two reflective mirrors redirect the light beam into the evacuated optical tube. The SST being a large aperture refractive telescope requires a long optical tube to achieve the necessary focal length and so the telescope is housed in the tower. To overcome the cumbersome task of rotating such

a large tube, the SST make use of a turret design that only rotates the prime opening and then reflects the light beam into the tube. The light beam is directed down the tube through the field lens at 'A' and onto an optical table at 'C' where the light can be directed to a specific imaging instruments. The Schupmann corrector resides at position 'B' in the diagram.

2.1.2 CRisp Imaging SpectroPolarimeter

CRISP is a telecentric, double Fabry-Pérot interferometer (FPI); FPI instruments have the ability to finely tune desired wavelengths, produce data of high-spatial and temporal resolutions as well as provide a relatively large field-of-view (FOV); (de la Cruz Rodríguez et al., 2015). An FPI instrument makes use of two parallel reflecting optical flats known as an etalon or parallel mirrors (interferometer) with the reflecting surfaces facing each other. Collimated light is focused on a point on the surface and is multiply reflected in the cavity producing an infinite train of transmission peaks. The light trains interfere constructively, producing a sharper image at the focus point (providing the degree of reflectivity is high). The observed wavelength can be tuned by changing the distance between the reflective surfaces. This can be operated quickly $\sim 50\ ms$, and is highly suited for spectral imaging of the chromosphere where the evolutionary time-scales can be on the order of a few seconds (Rouppe van der Voort et al., 2009). CRISP uses a double FPI set up, where the first etalon (high resolution, HRE) defines the wavelength and the second (low resolution, LRE) etalon suppresses the first few orders of the HRE secondary transmission peaks. The purpose of this set-up is to provide precise measurements of single wavelengths. A pre-filter is used to attenuate high-order transmission peaks of both etalon sets, further limiting the spectral range and ensuring a quasi-monochromatic beam. CRISP sits in the red band of an optical beam splitter that splits the main beam into red and blue light, the CHROMIS instrument sits in the blue band (de la Cruz Rodríguez et al., 2015).

CRISP utilises three high-speed low-noise CCD cameras with a frame rate of 35 frames per second and an exposure time of 17 ms (Rouppe van der Voort et al., 2009). An optical chopper synchronizes the cameras, two of the cameras are positioned behind CRISP after the polarising beam splitter, and the other is positioned before CRISP but after the CRISP pre-filter. The pre-CRISP camera is used for image restoration (Henriques, 2012) and is referred to as the wide-band channel and the two behind CRISP are narrow band, Fig. 2.3 (de la Cruz Rodríguez et al., 2015, Rouppe van der Voort et al., 2009). The use of these cameras for image processing will be described in the later sections.

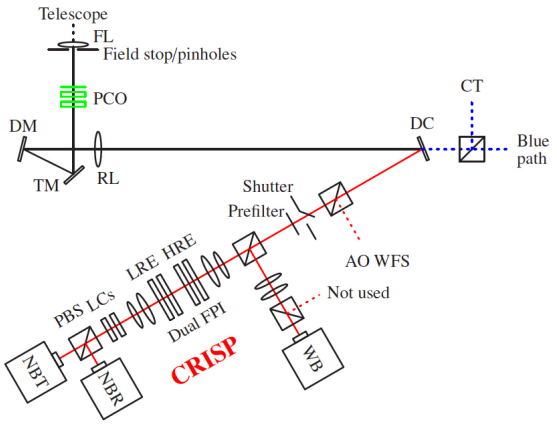

FIGURE 2.3: **CRISP.** Schematic of the CRISP optical setup located at the bottom of telescope at region A in Fig. 2.2. Symbol definitiions: FL = Field Lens, PCO = Polarization Calibration Optics (not in the beam during normal observations), TM = Tip-tilt Mirror, DM = Deformable Mirror, RL = Reimaging Lens, DC = Dichroic Beamsplitter, CT = Correlation Tracker, AO WFS = Adaptive Optics WaveFront Sensor, FPI = Fabry– Pérot Interferometer, HRE = High Resolution Etalons, LRE = Low Resolution Etalons, WB = Wideband, NBT = Narrowband Transmitted, NBR = Narrowband Reflected, LCs = Liquid Crystal modulators, PBS = Polarizing Beam Splitter. Image credit: (de la Cruz Rodríguez et al., 2015)

2.2 Imaging

One of the key uses of CRISP is as a spectropolarimeter; spectropolarimetry exploits the polarisation of light to measure physical quantities of the source. CRISP uses a series of polarising filters to gather intensity from each orientation of light and a four-state liquid crystal scheme combines and converts the polarisations states into a linear state that can be analysed (Schnerr et al., 2011). Light oscillates in all directions, its polarisation is dependent on factors that include interactions with fields (e.g. magnetic) and so by measuring the degree of polarisation information on the interacting fields can be inferred.

The polarisations of light are described by the Stokes parameters, I, Q, U and V, each component is attributed to a degree of polarisation. Parameter 'I', is the total intensity observed or can be thought as the summation of the polarised parts in all directions. Parameter 'Q', is the difference of the linear polarisation in the horizontal and vertical plane. 'U' is the linear polarisation intensity in the linear plane at 45 degrees. Finally, 'V' is the circular polarisation intensity.

Using the polarisation parameters it is possible to use inversion techniques to obtain information on source properties, such as the use of circular polarised light to inform on magnetic field. Furthermore it is possible to obtain temperature information from linearly polarised light that responds to scattering from particle interactions.

CRISP is also used for spectral imaging and spectroscopy; this technique makes use of the ability to tune the wavelength to precisely measure light from specific atomic transitions, for example the widely used H-α line. Recalling the details of spectroscopy, light can be separated into its constituent spectra by means of diffraction using a spectrometer, this is achieved by exploiting the fact that different wavelengths of light diffract at different angles and so the different 'colours' of light can be separated out. Due to particle and photon interactions, atoms in the solar atmosphere can be excited and de-excited causing transitions in the atomic energy levels. This causes energy to be released (or absorbed) in the form of photons with specific wavelengths attributed to the atomic transition and element they originate. As seen in the VAL model, Fig. 1.5, specific spectral line formations occur over a range of temperatures in the atmosphere and so by observing light from particular lines, we can reveal aspects of the solar atmosphere at those temperature locations.

2.3 Data reduction pipeline

In order to produce science-quality data, calibration is essential. In this section we will give an overview of the image reduction pipeline used to address seeing and instrument contributions to data artefacts and noise as described by (de la Cruz Rodríguez et al., 2015).

CRISP utilises a series of state-of-the-art components and optical arrangements to produce high-quality images, however all instruments introduce a certain level of noise into the resultant data and CRISP is no different. The use of the telecentric double FPI means having incredibly finely tuned images, but it also causes a field-dependent variation in the transmission profile of the reflected light, that is the profile of the reflective transmission train between the etalon. This is due to imperfections on the etalon influencing the phase difference of successive reflections between the etalon plates. This has the result of the central wavelength position of the transmission profile to vary over the etalon surface and shifting, these are known as cavity errors. The transmission profile is dependent on the quality of reflectivity of the etalon surfaces; high reflectivity corresponds to sharper profiles, which is the reduced spread of intensity over a wavelength range. This is a crucial quality for spectral imaging where the goal is to observe monochromatic light. Additionally, variations in the reflectivity coating of the etalon cause the width of the transmission profile to change along the FOV, these are known as reflectivity errors. It is necessary then to correct for these wavelength shifts to overcome the resultant artefacts that appear in the data.

Instrument effects are handled by the flat-field data, this includes the detector variations such as variant gain and distortions in the optical path. Flat-field correction is a standard technique to remove these imperfections from the resultant image, accounting for systematic errors. In the case of the SST, the flat-fields are made by averaging several short-exposure images while rotating the telescope in small circles around the solar disk centre. This has the aim of producing a spatially averaged quiet Sun spectral profile. However, this means that the average profiles will be affected by the cavity and reflective errors and cannot be used directly for image corrections. The manifestation of these errors will be a distortion of the profiles and so in order to remove them they must be categorised.

(de la Cruz Rodríguez et al., 2015) describes the technique employed to correct the flat-field, the process involves estimating a cavity error map and adjusting the spectral profile of the FOV by the shifts in the error map, bringing the spectral profiles to be consistent in each location. The cavity map is modelled using an iterative Levenberg-Marquardt scheme (Markwardt, 2009). The model is adjusted until it fits a time averaged uncorrected image of FOV profile. Using this map, a corrected flat-field is produced by subtracting the spectral variations and calculating the intensity percentage variation effect on the data (de la Cruz Rodríguez et al., 2015, Equation 3).

However, residual distortions can still remain as the averaged data is not free from atmospheric disturbances. This is overcome by employing a high-frequency filter which removes the small-scale fluctuations that make the largest contributions to distortions. The large-scale motions (low-frequency) are handled after the restoration of the wavelengths are complete.

The instrument darks are taken in a similar way to the flat fields except with the light path blocked from the telescope. The intention is to measure the electronic noise that is evident in the detectors. Once the noise levels are recorded they can be subtracted from the data at a later stage (Schnerr et al., 2011).

As stated, CRISP uses a combination of three cameras and these need to be aligned accurately. To do so, a pinhole array is placed in the optical path at an early focus. The purpose of the array is to form a image of a known distinct pattern that can be used to align each camera. The pinholes are of suitably small diameter such that solar structures are not evident, therefore the image formed by the pinholes is the same for each camera. The pinhole array is also used to measure image scale per pixel, something that can differ dramatically with changes on the optical table (where CRISP is mounted) and the wavelength being observed. The pre-filters used also have the effect of moving the focus and so also need accounting for in this manner. The pinhole grid pattern and spacing are measured in pixels using parameter fitting. After initial manual measurement, the

coordinates of the pinhole nearest the origin, the grid spacing in the two grid axis directions, and the rotation angle are all measured, these values are then used to correct alignment and scale issues.

Image restoration of wave-front aberrations is managed by the Multi-Object Multi-Frame blind Deconvolution (MOMFBD) method (Löfdahl, 2002, van Noort et al., 2005). The underlying assumption for this method is that the aberrations are isoplanatic, meaning that the point spread function (PSF) is constant across the FOV. To ensure this assumption is held, the processing is done on overlapping fields and so averages the profile. Each sub-field is low-pass filtered based on their individual signal-to-noise ratios and the PSF of the raw data is deconvolved using fast Fourier transforms, essentially removing the aberration contribution to the profile (Henriques, 2013).

In order to produce homogeneous time-series data, the wideband imaging camera is used to establish time-dependant corrections needed to remove aspects of remaining distortions unaccounted for by the adaptive optics and MOMFBD. These corrections are then applied to the narrow band images. These corrections also address issues of residual misalignment and image rotation due to how the telescope tracks Sun during observation.

Among these corrections, the rotation angles are calculated based on theoretical models of the telescope pointing and the position of the Sun in the sky. Images from the wideband camera are co-aligned using cross-correlation, small-scale cross-correlation methods are used to remove rubber-sheet motions that are evident at differing time-frames. These corrections are also added to the cavity map making a time-dependent wavelength correction. Other seeing effects include the changing elevation of the Sun in the sky causing variant intensity over time. This is compensated for by using computations of the mean intensity in the wideband channel.

2.4 The Helioseismic and Magnetic Imager

HMI is one of three instruments on board the space-based Solar Dynamics Observatory. It is the first instrument to provide continuous observations of the full solar-disk magnetic field in all orientations, (Stanford.edu, 2010). Observations are carried out in the Fe I 6173 Å line at a resolution of one arc-second and the produced data types are; dopplergrams of the solar surface velocity, continuum filtergrams (solar photosphere) and both line-of-sight and vector magnetograms of the photospheric magnetic field, (Stanford.edu, 2010). The HMI instrument makes use of the Stokes polarisations to measure

the components of the photospheric magnetic field and the data products are produces using the relevant inversion method.

HMI is a refracting telescope with an polarization selector, image stabilisation system and narrow band tunable filter, (Stanford.edu, 2010). The 4096 x 4096 pixel CCD camera allows for spatial sampling of 0.5 arc-second per pixel. Two identical cameras capture images in sequences of tuning and polarisation at a cadence of 4 s, (Stanford.edu, 2010). Each camera is dedicated to a specific data type; Doppler velocity, line-of-sight (LOS) magnetic flux, and continuum proxy images are taken with on camera every 45 seconds, while the vector magnetic field maps are taken every 90 or 135 seconds, (Scherrer et al., 2012).

In this study we use the HMI instrument to estimate the centre of an irregular shaped sunspot, however the data itself does not make up the bulk of the analysis. As such a detailed explanation of its optics and reduction pipeline is not described here but can be found in (Schou et al., 2012a,b).

3

Datasets and spectral line formation

Observations were carried out of the solar chromosphere using the H-α 6563 Å and Ca II 8542 Å spectral lines. These made up two datasets. The first, a disk-centre, quiet Sun time-series taken in H-α 6563 Å. The second, a disk-centre, sunspot time-series taken in Ca II 8542 Å. Further, Fe I 6173 Å data of the photosphere is used to support observations of the Ca II sunspot. Here, the spectral lines used to probe the atmosphere will be described along with the subtleties and implications of their formation. We will present the two datasets used in this research and we will discuss the inhomogeneities present in the data and the methodologies utilised to address them, and finally the models developed to estimate data noise and residual alignment errors.

3.1 Chromospheric spectral lines

3.1.1 The H-α 6563 Å spectral line

Light from H-α line-core is perhaps the most renowned of the chromospheric spectral lines due its vibrant brilliance as seen in observations. As seen during a total solar eclipse, its pinkish, reddish hue is what led to its naming, *chromosphere* - sphere of colour. On disk, the H-α chromosphere is most distinguished by its nest of fibrils, Fig. 1.10. Figure 3.1 displays the average spectral lines from the dataset from; left, the IN regions and right, the network regions. Over-plotted in red is a example Voigt profile determined from least-squares fitting. The units 'DNs' refer to the intensity data units as captured by the CCD uncorrected to photoelectrons.

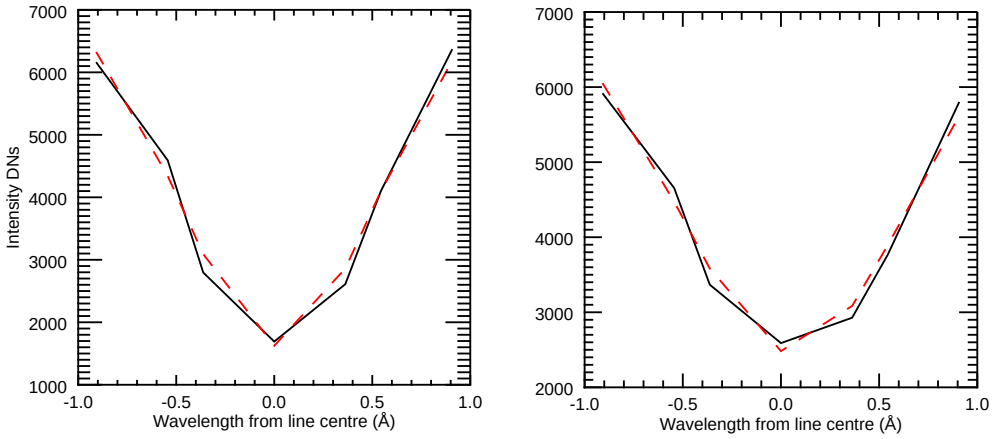

FIGURE 3.1: **H-α spectral profile.** Spectral profiles from the H-α dataset (black), over-plotted in red is an example fitted Voigt model. In the left panel the average spectra for the quiet Sun regions is plotted and in the right panel the average for the lower network region (as seen in Fig. 1.10).

The H-α line is part of the Balmer series of atomic transitions of the Hydrogen atom, specifically the transition of the electron from the third to second energy levels. Hot shocks in the atmosphere provide an ample means to ionise the hydrogen atom (Rutten, 2008). THe ionisation causes it to lose its electron, subsequent recombination and the following cascade of energy produces the H-α light (Rutten, 2010). As the chromosphere is prone to upward propagating shocks, H-α is readily formed there. Furthermore, collisions and radiative excitations also cause the promotion of an electron to the $n = 3$ level leading on to the production of H-α in the resultant de-excitation. As the former method is only due to slow recombination times, (Leenaarts et al., 2012), the latter method may be key.

The H-α line is sensitive to thermal broadening, this is due to its relatively small atomic mass (Cauzzi et al., 2009, see equation 1), meaning measurements of the Doppler widths of the line profile can reveal temperature information. (Leenaarts et al., 2012) revealed that temperature dependencies for the opacity of the line only exist for the low chromosphere and photosphere where conditions are close to local thermal equilibrium (LTE). The depth of the line (line core) is not dependant on temperature and therefore fluctuations in the line core are not the result of thermal perturbations but of density(i.e column mass).

As seen in the VAL3C model, Fig. 1.5, the H-α spectral line is not formed over a discrete atmospheric height. In fact, the core of the line spans over hundreds of kilometres in the range of 1200-1700 km from the Sun's surface and the wings of the line are formed much lower in the region 100-400 km, approximately in the photosphere. Interpretation then of the H-α can be difficult as it depends on the region that is being observed. Therefore

a reliance on numerical simulations to describe the formation and shape of the line has become a staple of the field. The problem arises with the difficulty of calculating these models and until recently computational power hasn't been available to produce full non-local thermodynamic equilibrium (NLTE) and 3D radiative transfer numerics necessary for simulating the chromosphere. However, the H-α line has been modelled using LTE calculations in the past and these models do describe the wings of the line quite well, (Rutten, 2007), this is likely due to the photosphere (LTE environment) being evident in the wings though it does not well represent the core.

(Leenaarts et al., 2012) describe the discrepancy between H-α synthetic data and observables, simulations using a 1D radiative transfer model showed granulation patterns in the line core, something that is not seen in observations. (Leenaarts et al., 2012) were able calculate full 3D radiative transfer and NLTE effects; the synthetic data was able to replicate the temperature correlations with line width for low atmosphere and the contrary in the upper atmosphere. The models were also able to produce the fibril patterns for the first time and were able to show their appearance to be aligned with enhanced chromospheric density and magnetic field direction. However, a plethora of granulation patterns could still be observed in the line core suggesting that the model is currently unable to reproduce the observed signatures. The paper concludes that the H-α line is well suited for observing the magnetic structure of the chromosphere because it has a significant amount of opacity in the low beta regime where magnetic field is the key structuring agent.

(Leenaarts et al., 2015) was able to produce fibril-like structures reminiscent to observations in terms of intensity contrast, time evolution, wave properties and Doppler shifts. Though it appeared the synthetic fibrils has a combination of properties previously observed in active and quiet region fibrils. As discussed in the later parts of Section 1.5.4 this simulation study highlighted inconsistencies with the field alignment of the fibrils with previous assertions.

It is evident that observations alone cannot be used to interpret the physics of the chromosphere and that numerical simulations of the H-α line have been crucial in the understanding of the features present there. It will only be with improved modelling techniques that will be able to full grasp the implications of the observables.

3.1.2 The Ca II 8542 Å spectral line

Ca II 8542 Å is part of a triplet of infra-red resonant spectral lines originating from the transition from the fourth energy level to the third of singularly ionised calcium (Cauzzi et al., 2008). Like the H-α line, the Ca II line shows a nest of fibril structures in line

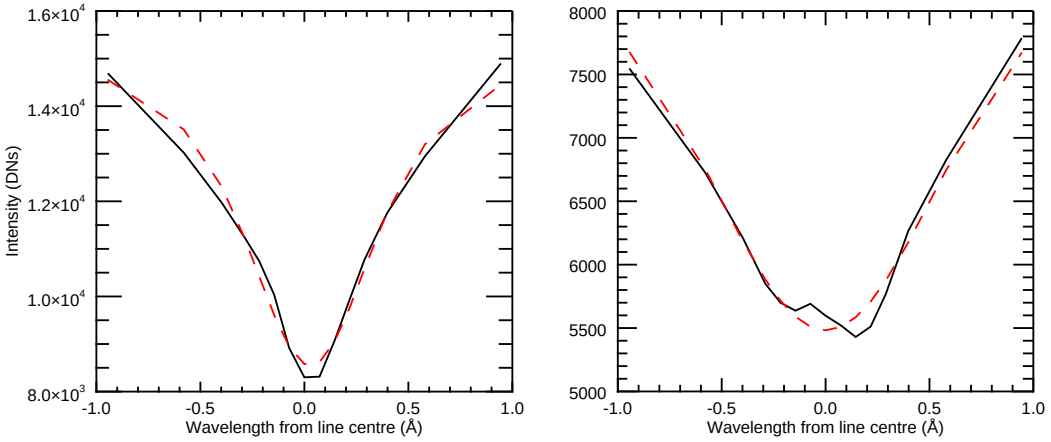

FIGURE 3.2: **Ca II spectral profile.** Average Ca II spectral profiles (black) with over-plotted Voigt profiles (red). In the left panel the average spectra is plotted for a region outside of the sunspot, in the right panel from a region in the umbra.

core images (though with less opacity) and in the wings convective patterns (reversed granulation-the reversal of granulation intensity contrast) of the photosphere are prevalent. The wings of the line are formed in the upper photosphere, LTE environment and the core of the line is formed in the NLTE chromosphere by radiative transitions. Ca II has a deep core, steep inner wings and shallow outer wings, Fig. 3.2. The inflection between the wings mark the sharp transition between the photospheric formation and the chromospheric, this quick transition is a reflection of the gap between the formation heights. However, this atmospheric gap in line opacity is not as large as it is in H-α, this is because the H-α transition requires more energy for the excitation, (Cauzzi et al., 2008). The line source function decreases with height with increasing electron temperature; in other words the opacity increases and this effect is steeper in the chromosphere. The result leads to the above discussed manifestations of the shallow wings decreasing in intensity and a steep deep line core.

Unlike the H-α line Ca II is more sensitive to non-thermal broadening due to its larger mass (Cauzzi et al., 2009, equation 1), and so can be used to determine velocity characteristics.

3.2 Observations

The observations used in this study were carried out and reduced by Vasco Henriques.

3.2.1 Quiet Sun H-α

The following summary of the H-α dataset is adapted from (Mooroogen et al., 2017).

The H-α observation is situated on the boundary of a coronal hole at the disk centre (Heliocentric Cartesian - X0", Y31.5"). The data was taken with the Swedish Solar Telescope (SST) using the CRISP instrument between 09:06 and 09:35 UT on 3^{rd} May 2013. The main sequence spectral scan includes the following wavelength positions from H-α line centre: $\pm$ (0.36, 0.54, 0.91) Å, corresponding to a range of ± 41 kms^{-1} in velocity. The cadence of the full spectral scan is approximately 1.3 s with 1150 frames, the spatial sampling is on the order of 0".06 per pixel and the resolution 0".16 (Mooroogen et al., 2017). Photospheric Fe I 6301 and 6302 Å spectral scans were also taken of the same FOV to obtain full Stokes profiles. These scans were taken intermittently with the H-α observations every five minutes, this then leaves 30 s gaps in the H-α time-series. LOS magnetograms were constructed using the Stokes V component (see, Kuridze et al., 2015). This dataset has also been used by (Samanta et al., 2016) who studied the the lifetimes of chromospheric structures and their impact on Fourier power spectra, and (Henriques et al., 2016) who found a correlation between RBE's and RRE's and SDO emission at coronal temperatures. In addition to the spectral data, full Stokes scans and Fe magnetograms exist; Dopplergrams, profile-minimum and line width data products were calculated from the line core. The methods used to produce these additional diagnostics will be discussed in the next section.

3.2.2 Sunspot Ca II 8542 Å

The Ca II observation is an active region sunspot close to disk centre N 9.25 W 4.50, taken with the CRISP instrument on the SST on 28^{th} July 2014 between 10:43 and 11:24 UT. The spectral scan is made up of fifteen wavelength positions in the range $\pm$ (0.942, 0.580, 0.398, 0.290, 0.217, 0.145, 0.073) Å from line centre. The data has the same spatial sampling as the H-α set, and in addition to the spectral imaging a full Stokes parameter scan also exists. This dataset has unfortunately a variable cadence and is missing two data frames over the total 79. However, with the use of pixel-to-pixel interpolation (using spline interpolation) the cadence is regularised to 30 s and data gaps filled to create a total of 81 frames. The 30 s cadence of this dataset is at the observational

temporal limit for useful time-series analysis, this is because of the fast propagation speeds of chromospheric wave dynamics, e.g Table 4.2. The relatively slow cadence is a consequence of the high number of wavelength positions measured for a full Stokes parameter scan, which introduces a delay from the optical chopper during measurement. In addition, profile minimum, Dopplergram and line width data products were produced (Fig. 1.13 bottom left and right panels). Co-aligned HMI field and continuum data was obtained to help diagnose the sunspot centre for radial measurements. The observation is a full-disk contiunum image and LOS magnetic field data derived from Milne-Eddington (ME) inversions (Bobra et al., 2014). The ME inversions are an approximation used to determine magnetic field properties from spectral line profiles (Centeno et al., 2014). The datasets were taken on 28^{th} July 2014 at 10:46:25 UT with the HMI instrument on-board SDO in the Fe 6173 Å line.

3.3 Noise estimation

Before a reliable analysis of the datasets can be undertaken an understanding of the data errors is required. In this section, we will describe the source of potential errors and the methodology used to address them.

3.3.1 Estimating the intensity errors

The reduction pipeline for the SST CRISP data goes to great lengths to ensure high signal-to-noise datasets. In Section 2 we highlighted some of the methods used to alleviate sources of noise and address systematic error. Whilst the utilisation of MOMFBD and de-stretching of the data make significant impacts on reducing atmospheric contributions (as described in Chapter 2), some level of uncertainty will remain. Furthermore, as discussed in Section 2 despite extensive work to account for the cavity errors, there will be residual uncertainties left in the data. Due to the extensive nature of the full CRISP pipeline it is impossible to propagate uncertainties through each stage of calibration. In an ideal scenario a statistical re-sampling method would be employed. This would work by modelling the noise correlated with the pre-processed data and repeat the reduction pipeline a number of times. This would facilitate an inspection of how those uncertainties are propagated through the pipeline and contribute to the variations in spatial location and intensity. Unfortunately, by current computational standards this method is impractical due to the sheer amount of processing time required for reduction on multiple datasets.

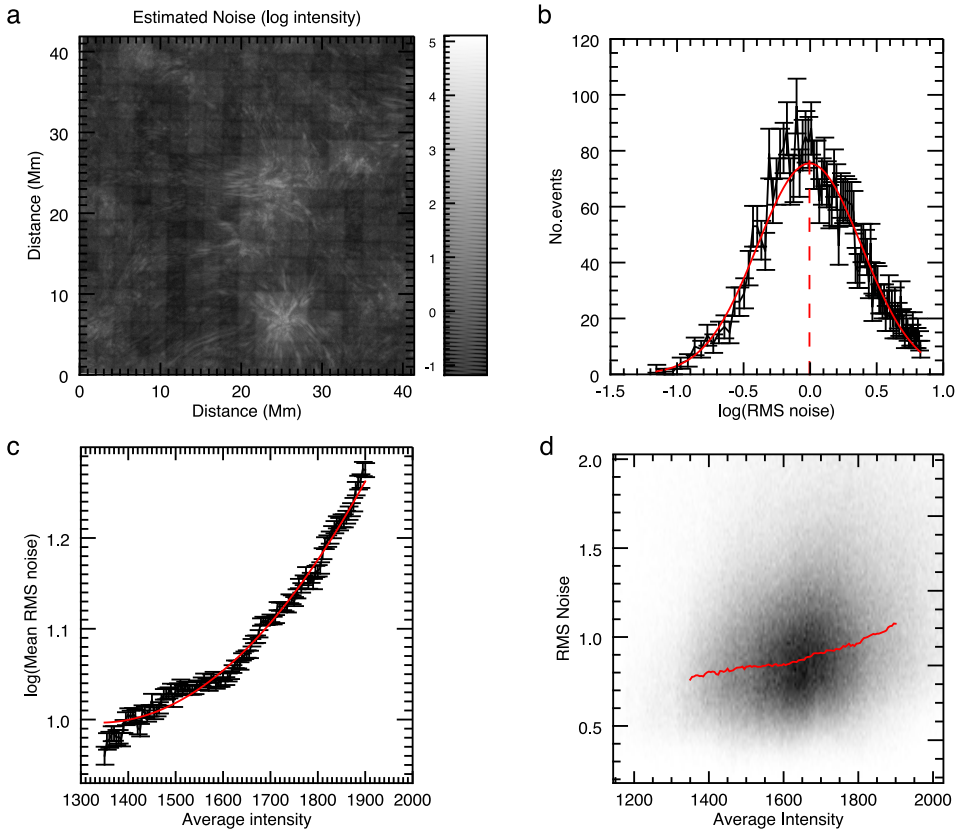

FIGURE 3.3: **Estimating Uncertainties-H-α Data.** This four panel figure depicts the stages of error estimation for the H-α dataset. Top left image (a) depicts the RMS noise estimate resulting from the multi-scale processing, the natural logarithm has been taken to aid in visualisation. Residual data features can be seen and the colour-bar highlights the level on intensity in natural log units. In the bottom right, the 2D histogram showing the correlation between the average intensity and RMS noise. The top right panel shows an example distribution of the log RMS noise from a single average intensity bin. The red line indicates the fitted mean. The bottom left plot shows the established relationship between the average intensity and RMS noise resulting from the fitted means of the RMS noise distribution.

In order to estimate residual uncertainties in the data we make use of multi-scale image processing with the aim of establishing a relationship between intensity of the data and noise. The method relies on the assumption that it is possible to estimate uncertainty on the measured intensity values from the noise in processed data. Though, it is recognised that this will not estimate existing systematic errors. First, we must establish an image that is representative of the 'noise' from the whole FOV. To do this, the data image is cropped to remove artefacts at the edges left over from the reduction pipeline and then filtered in space using a multi-scale filter underpinned by the à-trous algorithm with a 2D B3 spline filter (e.g., Starck & Murtagh, 2006, Stenborg & Cobelli, 2003). Then, unsharp masking is used on the data at the highest frequency scale. The intended goal here is to reduce the variations in the data to its lowest spatial scales and residuals treated as indicative of the data noise (Olsen, 1993). This procedure is repeated for forty

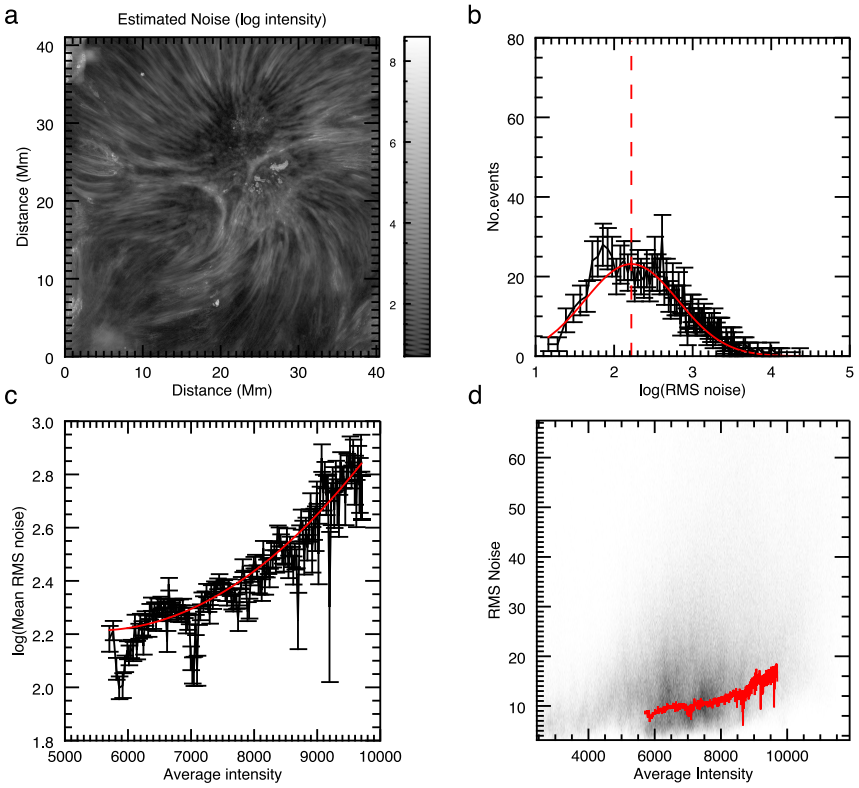

FIGURE 3.4: **Estimating Uncertainties-Ca II 8542 Å Data.** As with Fig. 3.3, this four panel figure shows the stages of error estimation for the Ca II dataset. The top left image (a) depicts the natural logarithm of the estimated noise.

successive frame in the time-series, the root mean square (RMS) of these frames is taken to estimate the standard deviation of the noise per pixel. Figures 3.3(a) and 3.4(a) show the estimated RMS noise for the the H-α and Ca II datasets respectively. Clear evidence of fixed pattern noise can be seen in the RMS noise, Fig. 3.3(a). This grid pattern is likely the result of small variations between the different MOMFB sub-fields, but is possibly made worse if a small number frames were taken during less favourable seeing conditions. These would have poorer resolution relatively speaking and a smoother intensity profile. Therefore, these regions would host less intensity variation and the average noise here would be reduced. The grid pattern covers a minimal area of pixels in the FOV and so the following noise analysis will not be largely affected. The pattern is not apparent in sunspot data, Fig, 3.4(a).

An average intensity image is also made from forty successive frames. Figures 3.3(d) and 3.4(d) show the joint probability distribution function (JPDF) of the average intensity and the RMS noise, a discernible trend between noise and intensity can be seen. The JPDF is made using the IDL HIST 2D function, the resultant distribution is a correlation map with density showing the number of times intensity values correlate by pixel over the original images.

To define this trend, the RMS noise values are binned as a function of average intensity and one-dimensional PDF slices of the RMS noise are taken, Figs. 3.3(b) and 3.4(b). The distributions show log-normal behaviour and the values of the mean and standard deviation are measured at each average intensity bin. In order to fit the log-normal distribution to the PDF, a Gaussian profile is fit to the values in log-space and the appropriate conversions are made afterwards. This method is used as the 'real' space distributions asymmetry led to difficulties in the fitting. The equation used to convert the log-space Gaussian distribution mean and standard deviation values is as follows:

$$\mu = ln\left(\frac{m}{\sqrt{1+\frac{v}{m^2}}}\right), \tag{3.1}$$

$$\sigma = \sqrt{ln\left(1+\frac{v}{m^2}\right)}, \tag{3.2}$$

where μ is mean of the PDF, m is the mean in log space, v is the variance in log space and σ is the standard deviation. These mean values are tracked along the average intensity bins through regions of the JPDF at high density. Figures. 3.3(d) and 3.4(d) highlight the tracked means in this region. Figures 3.3(c) and 3.4(c) show the average intensity versus the mean values of the RMS noise and a quadratic function is fit to this curve in order to establish a relationship between the quantities. The results of this fit give the parameters

$$ln(\sigma_I) = 8.20 \times 10^{-7} I^2 + 5.50 \times 10^{-4} I + 0.09 \tag{3.3}$$

for the H-α dataset, and

$$ln(\sigma_I) = 3.72 \times 10^{-8} I^2 - 3.36 \times 10^{-4} I + 3.00 \tag{3.4}$$

for the Ca II dataset, where I refers to intensity. These equations are used to determine the estimates of uncertainty of the measured intensity. They are approximately 0.1% of the intensity values, which is in line with expected noise estimates from theoretical derivations by for FPI instruments like CRISP (de la Cruz Rodríguez et al., 2012).

3.3.1.1 Multi-scale image processing - filtering

In the process of understanding the methodology of noise estimation we introduced the à-trous algorithm and unsharp-masking, here we will describe the details of those

techniques. The à-trous algorithm is an implementation of the wavelet transform that, like many other mathematical transforms, represent data as a set of orthonormal vectors, the sum of which equal the data. More descriptively, the wavelet transform separates data into constitute parts by frequency, the number of parts or *scales* can be chosen by the user. The advantage of this is one can remove redundant frequencies of the data and reconstitute the remaining frequencies. This is essentially compression utilising transforms. In the same manner this could be used to remove noise from the data or reveal hidden signatures within the data not obvious in the original dataset. These examples are from the signal processing perspective and the use of wavelet transforms are not limited to them. However, the described uses have the same thing in common, filtering, which is the implementation used in this work. Unlike the Fourier transform the 'shape' of the filter or filtering function h in a wavelet transform can be pre-defined. In a Fourier transform, the mathematical 'basis' (filter) is sinusoidal; the series that will make up the data will be derived from either sine or cosine series. Whereas in a wavelet transform, the basis is user defined depending on the type of data and needs of the user. An extensive look at wavelet analysis and basis selection can be found in (Torrence & Compo, 1998).

The à-trous algorithm is just one method of implementing a wavelet transform. It is a known stationary redundant transform meaning that the output has the same number of samples as the input. This is also known as having transformation invariance, which is a desired quality in order to reduce artefacts (decimation) in the transform (Starck & Murtagh, 2006). Other advantages of the à-trous are that it is an isotropic transform, meaning that the transform is the same at every pixel and known, thus making interpretation simpler and it is also computationally expedient. The à-trous algorithm allows hierarchical decomposition of a data image into a series of scales, with each scale retaining structures within a given pre-determined dimensional scale. This is analogous to passing the data through finer sieves at each scale. This can be described mathematically (Starck & Murtagh, 2006) as

$$C_{0,k} = C_{J,k} + \sum_{j=1}^{J} w_{j,k}, \tag{3.5}$$

where C_0 is the original image, subscript k refers to all pixels, J refers to the iterations, $C_{J,k}$ refers to the lowest scale in the transform and w is the wavelet transform of the data at each scale.

In Figure 3.5 the à-trous algorithm has been applied to a single frame of the H-α dataset. In each successive frame of the figure the ever increasing frequency scales can be seen, this is indicated by the apparent degradation of the image up to its highest spatial

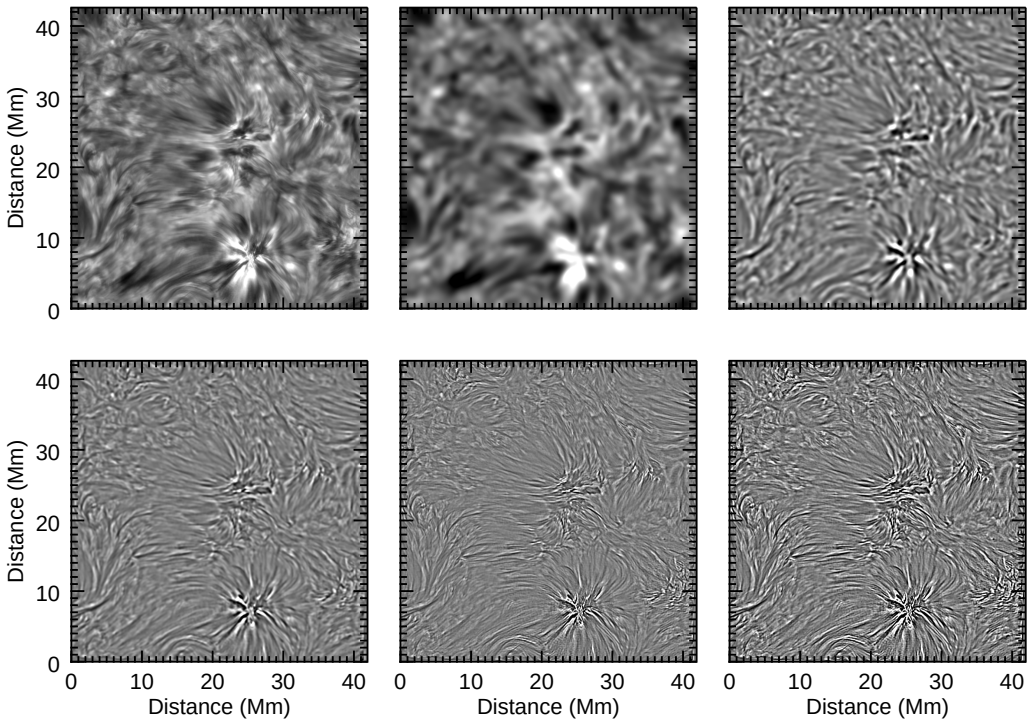

FIGURE 3.5: **The à-trous algorithm.** The à-trous algorithm acting on a single frame of the H-α dataset. In each successive image starting from the top left (which is the original data), the data is reduced up to its highest frequency. In this example five scales have been used and summing these scales would recover the original data. Images have been range clipped for visual clarity.

scale. In the example shown here, only five scales have been used, the summation of these images would recover the original image. To understand the implementation of the algorithm, first we will define the continuous wavelet transform (Starck & Murtagh, 2006)

$$W(a,b) = \frac{1}{\sqrt{a}} \int_{-\infty}^{\infty} f(x)\psi^*(\frac{x-b}{a})dx, \tag{3.6}$$

where $W(a,b)$ is the wavelet coefficient, ψ is the analysing wavelet, $a > 0$ is the scaling parameter and b is the positional parameter. Now, the analysing wavelet is the basis function, which can be chosen based on the requirements. The function ψ is dependant on the scaling function ϕ such that in the à-trous algorithm the chosen analysing wavelet is the difference between scaling functions of successive scales. This is shown in (Starck & Murtagh, 2006) as

$$\frac{1}{2}\psi(\frac{x}{2}) = \phi(x) - \phi(\frac{x}{2}), \tag{3.7}$$

the filtering function, h, as mentioned in the earlier discussion is derived from the scaling function. With those dependencies in hand we can now see the implementation of the algorithm as described in (Starck & Murtagh, 2006).

1. Initialize j to 0, starting with a signal $C_{j,k}$. Index k ranges over all pixels.
2. Carry out a discrete convolution of the data $C_{j,k}$ using a filter h, yielding $C_{j+1,k}$. The convolution is an interlaced one, where the filter's pixel values have a gap (growing with level, j) between them of 2^j pixels, giving rise to the name à-trous ("with holes").
3. From this smoothing (convolution of the functions) we obtain the discrete wavelet transform, $w_{j+1,k} = C_{j,k} - C_{j+1,k}$.
4. If j is less than the number J of resolution levels wanted, then increment j and return to step 2.

The set W will contain the wavelet transforms and the final scale, $[w_1, w_2, w_3, C_j]$ and h in our case is a cubic spline filter.

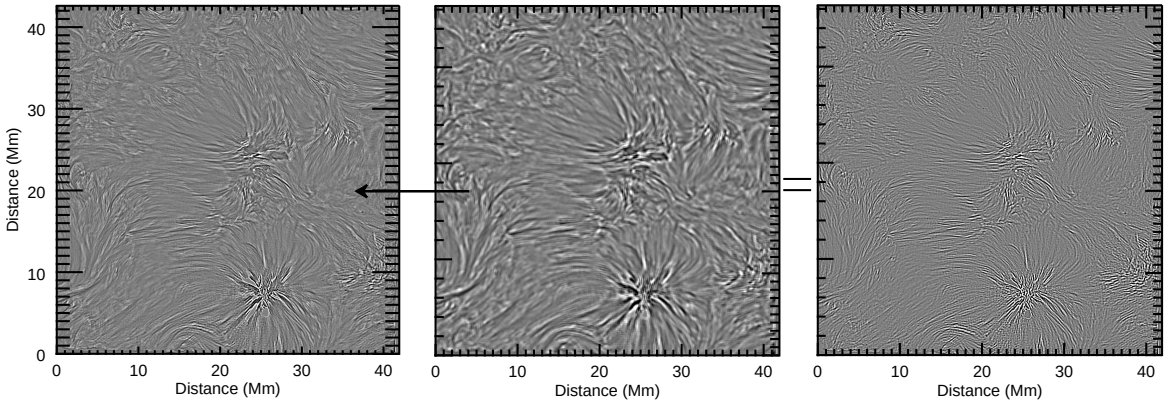

FIGURE 3.6: **Unsharp-masking.** Left most image in the panel is the original image (after à-trous, last image of Fig. 3.5). The centre panel is the smoothed image and the right most image is the result of unsharp-masking the lowest scale of the H-α image following the à-trous. Data has been clipped for visual clarity.

Also discussed in Section 3.3 is unsharp-masking, which is a standard image analysis tool widely used in a range of fields. Unsharp-masking is essentially a high-pass filter that enhances high-frequency components in an image. In this work we employ unsharp-masking as filtering tool and as a method of increasing contrast in time-distance diagrams for wave detection, see subsection 4.2.2. Simply put, the result of unsharp-masking is the subtraction of a blurred or smoothed image from the original image, see Fig. 3.6. In pseudo-mathematics the implementation is as followed,

$$g(x) = f(x) - f^{'}(x), \tag{3.8}$$

where $g(x)$ is the unsharped image, $f(x)$ is the original image and $f^{'}(x)$ is the smoothed or blurred image. Figure 3.6 shows the application of unsharp-masking on the result of the lowest scale of the à-trous. The smoothing used with this method is a simple box-car average.

3.3.2 Estimating misalignment error

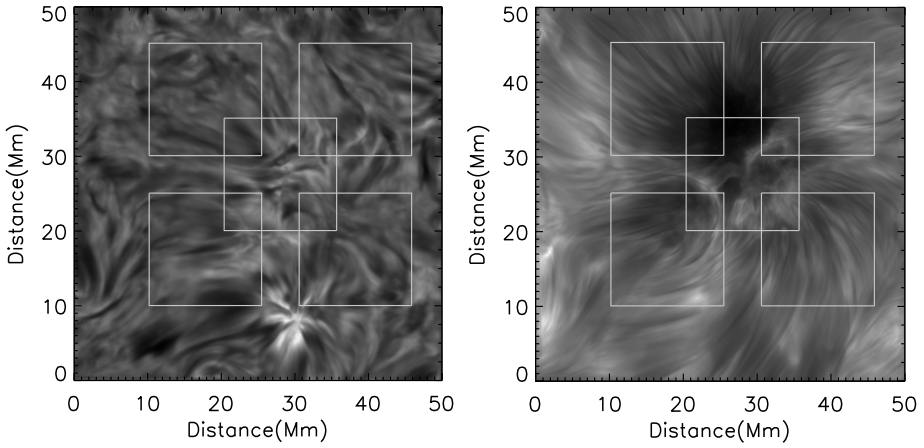

FIGURE 3.7: **Cross-Correlation Sub-Regions.** Two panel image showing the cross-correlation subregions defined in the H-α data (*left*) and the Ca II data (*right*).

In addition to intensity noise estimates, we also estimate residual frame-to-frame misalignment resulting from telescope motions or jitter. To do this, we employ cross-correlation routines to evaluate the shifts between the first frame with each successive frame. The routine creates a 2D correlation map utilising FFT, finds the maximum within this map and fits a 2D surface to achieve sub-pixel accuracy to return a vector of pixel shifts per time. In order to quantify this shift, we take five sub-regions of size (300 x 300) pixels from the FOV and perform the cross correlation on each region. e.g see Figure 3.7 for the specified in regions in the H-α and Ca II datasets. These relatively small sub-regions are selected as the cross-correlation requires unique features to 'lock on to', and a larger area would contain too much information. Multiple sections are chosen to build an average of the shift in the FOV, as a single sub-region would not be indicative of the whole image. This produces five time-series vectors that describe the pixel shifts in both the 'x' and 'y' directions.

The cross-correlation method is a measurement of the likeness of two sets of data, as a function of their displacement from one another. Conceptionally, we can consider two

functions f, g differing by some some shift (also known as 'lags') in x. We can use cross-correlation to shift g in the x direction until the closest match between g and f can be found. The resultant shifts can then be recovered. Mathematically, cross-correlation used in this manner is akin to convolution. The process essentially slides g over f in the x and calculates their product at each location. In this manner when the functions match, the convolution is maximised. Therefore it is possible to develop an algorithm that determines the maximum and hence the shift that produced it.

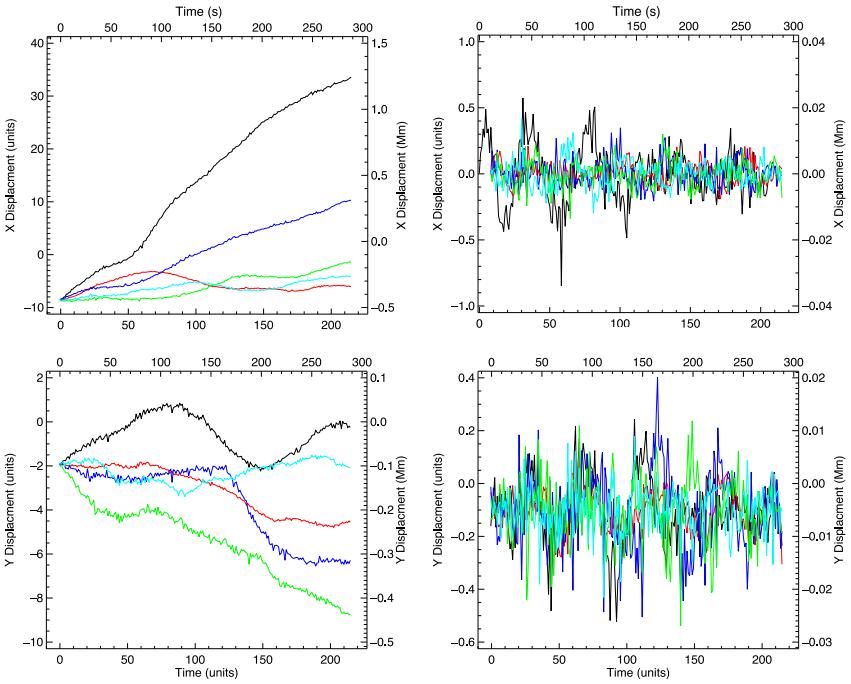

FIGURE 3.8: **Alignment Vectors-H-α.** Vector estimates for the error in data alignment for the H-α dataset. The left panels show the vectors for the x (*top*) and y (*bottom*) directions for the five cross-correlated sub-regions, the right panel shows the de-trended vectors accordingly.

Figures 3.8 and 3.9 display the estimated vectors resultant of the cross-correlation. In the left panel strong trends can be seen and it is likely that they are the result of physical dynamics. These motions could be the result of photospheric flows that push objects around, e.g., magnetic flux rising in inter-granular lanes in the internetwork that then are observed to migrate out to the network boundaries, which form large-scale magnetic flux features on scales of 30 Mm. The trends also show some oscillatory behaviour which is perhaps more apparent in the Ca II data. The residual motions are in opposite directions indicated by their oppositely directed gradients from the origin. This is a likely result of the radial flow from the sunspot in different sub-regions that can be seen in the time-series images. To account for these motions the vectors are de-trended by subtracting a 10 parameter polynomial fit, which ensures that we only include residual motions and do not include physical dynamics in the error estimation. The de-trended vectors can be seen in Fig. 3.8 and 3.9 right panels and there appears to be residual

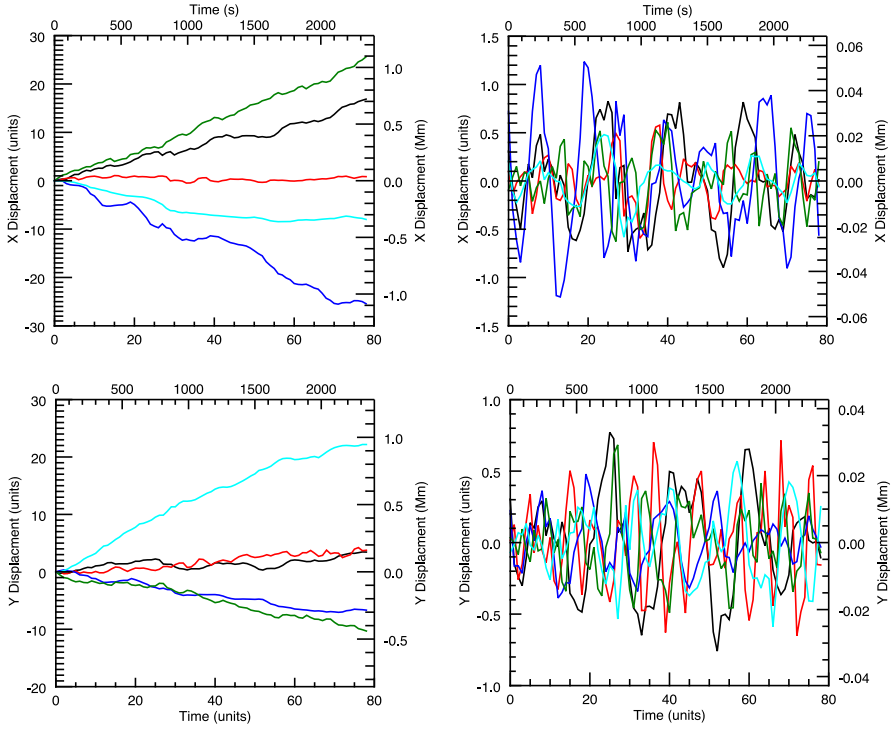

FIGURE 3.9: **Alignment Vectors-Ca II 8542 Å.** Estimates for the x and y error displacement vectors for the Ca II dataset. Left panels show the vectors for the five sub-regions and right panels show the de-trended vectors. In the left panel strong physical motions can be seen, in particular the oppositely directed flow from the five sub-regions shown in the right panel of Fig. 3.7. It can be seen that the two upper regions have motions in opposition to the two lower sub-regions and the centre region exhibits little motion. This is substantiated in the time-series image where it the outward flow from the sunspot can be seen.

oscillatory motion exhibited in the shifts. The RMS is taken over the five vectors for each direction (x and y) and in time to give two final values for pixel shift in each dimension. These are then added in quadrature to give the resultant average 'alignment error'.

3.4 Data products

Briefly mentioned in the above section, a series of data products were generated from the original datasets. Here we will discuss how those products are obtained and what these new diagnostics can tell us. For both the H-α and the Ca II dataset, the profile-minimum intensity has been estimated. This makes use of intensity measurements at the point of maximum absorption of the spectral line in replacement of intensity measurements of the rest wavelength of line core. These intensity measurements are used to overcome the effects of Doppler shifts of the line profile resulting from the dynamic nature of

the chromosphere. These Doppler shifts lead to problems when observing phenomena at fixed wavelength positions, mixing fluctuations in plasma conditions and velocities (Mooroogen et al., 2017). This is even more relevant for the Ca II observations where the spectral line is more sensitive to Doppler shifts than H-α. This makes evaluating the full evolution of fibrils difficult at fixed wavelengths, as the Doppler shift amplitudes are large enough to cover the full range (Rouppe van der Voort & de la Cruz Rodríguez, 2013). To measure the profile minimum, a pixel by pixel polynomial least squares fit to the spectral profile is carried out. Using this method both the intensity value of the minimum point and the wavelength position are measured.

Using the measurements of the wavelength positions, it was possible to create Dopplergrams by calculating the red shifts of the measured position and model wavelength of the line profile. This was accomplished by employing the standard Doppler formula,

$$v_{dopp} = c\frac{\Delta\lambda}{\lambda_{rest}}, \tag{3.9}$$

where v_{dopp} is the calculated Doppler velocity, $\Delta\lambda$ is the change in wavelength as measured by the fitted profile and λ_{rest} is the rest or model wavelength. The model wavelength used for the reference was taken simply as the laboratory value for either H-α 6563 Å or Ca II 8542 Å respectively, as such the resultant Dopplergrams give the relative velocities. In addition to the Dopplergrams, measurements of the spectral profile widths were made. The line width diagnostics can reveal different information depending on dominant line broadening mechanisms evident in the spectral line. In the case of H-α it has been discussed that the line wings are sensitive to temperature variations and that Ca II is sensitive to particle interactions. This means images created from these measurements can act as proxies for these diagnostics. Much like the profile-minimum, the spectral widths are fit on a pixel by pixel basis. However, here we employ a Voigt model,

$$V(x;\sigma,\gamma) = \int_{-\infty}^{\infty} G(x',\sigma)L(x-x',\gamma)dx', \tag{3.10}$$

where $G(x',\sigma)$ is a Gaussian profile, $L(x-x',\gamma)$ is a Lorentzian and x is the displacement from line centre. As it can be seen the Voigt distribution is a convolution of the Gaussian and Lorenz profiles meaning it takes into account both thermal and collisional broadening mechanisms respectively. These manifest in the parameters ,γ & σ, that refer to the collisional and thermal broadening mechanisms respectively in the Voigt equation. Both of these parameters contribute to the width of the line and then by

taking the σ parameter we can explore a temperature proxy whilst ignoring the collision contributions.

The difficulty in fitting these profiles arises from large shifts and enhancements in the spectral profiles spatially and temporally, these can be caused by large gradients in velocity or magnetic field in the medium. The result of this is a variation in profiles across the FOV and across time-frames. In Figures 3.1 and 3.2 the difference between the areas of stronger magnetic field (network/umbra, right panels) can be seen compared to the quiet sun regions. It is clear that both the intensity values and profile minimum position vary. Here, we have presented an average spectra of these regions, however on a pixel-to-pixel basis the variation is much larger. However, due to the large amount of pixels ($\sim$ 900 x 900 x 1000) the fitting cannot be handled manually on a profile to profile basis to account for each individual profile variation.

In the interest of automation, the wings of the profile are clipped and a rudimentary peak detector is employed to find the profile-minimum, as the profile shifts around. The detector simply finds the minimum point in the array and fits the profile around it. This method was chosen due to computational limitations on the speed of producing the data. It is found that over the majority of the FOV this method reasonably tracks and fits the profile. However, since the a-priori parameter guess of γ and σ are invariant, in regions where the profile varies significantly the fitting method routinely fails. This leads to discrepancies in these regions, though they are easily seen in the dataset and the positions of these are recorded in a separate array for posterity.

The limitation of the line width datasets stem from where on the profile the widths are measured. Currently the implementation measures the width around the profile core albeit with the wings cut off. However, this cropping of the profile does not account physically where photospheric contributions may lie and therefore the width measurements may not be solely chromospheric. Alternative methods using 'La Palma routines' (a host of codes for the La Palma observatory) based on a previously used lambda meter method, have been suggested by Rob Rutten in private communication. However, tests with these codes have not yet been carried out and mark an area of future and ongoing work.

4

Dynamics of internetwork chromospheric fibrils: basic properties and MHD kink waves

Fibrils are an understudied, omnipresent feature of the chromosphere that have been seen to act as MHD wave guides. The role of MHD oscillations, in context of solar atmospheric heating, suggests that these ubiquitous features may participate significantly in the energy propagation through the atmosphere. As such, they are features worthy of further study. In Sections 1.3, 1.4, 1.5.4 of Chapter 1 and Chapter 3 we set out the necessary theoretical background required to interpret the results of an investigation. In this chapter and Chapter 5 we will present and discuss the results of two statistical studies carried out on the H-α and Ca II datasets, both of which have been introduced in Section 1.5. As the research on the H-α data is presented in (Mooroogen et al., 2017), interpretation and discussion will mirror that of the paper.

4.1 Observations of IN fibrils

Utilising the high-resolution SST we aim to provide a comprehensive analysis of the nature of fibrils in the H-α internetwork. IN fibrils are observed to form away from the kilogauss, network flux; these fibrils are seen to support oscillatory behaviour that we interpret as MHD kink waves. We measure the parameters of these waves (amplitude, period and phase speed/propagation speed) and exploit them to perform magneto-seismology, which allows us to examine the variation of plasma properties along the wave-guides. Further, we employ FFT to determine if significant multi-frequency components exist in these waves and attempt to formulate an average power spectra of the quiescent H-α

chromosphere. We then compare these average spectra to previous determinations as a method of examining propagation in the atmosphere.

Figure 1.10 in Section 1.5 revealed the FOV of the quiescent H-α dataset. Approximately fifty fibrils were identified for investigation from this FOV away from the network areas (rosettes). These fifty were subsequently narrowed down to twenty eight fibrils based on their signal-to-noise quality in the time-distance diagrams. Specifically, their ability to be tracked by the employed code. It is important to note that of the twenty eight there exist only nine that are distinctly separate features. Due to gaps in the datasets as discussed in Section 3.1.1, the total time-series is split up into five minute sections and tracked fibrils are treated as new features in each of these sections. This is because the dynamics cannot be established within those data gaps and to avoid assumptions we simply treat them as new features.

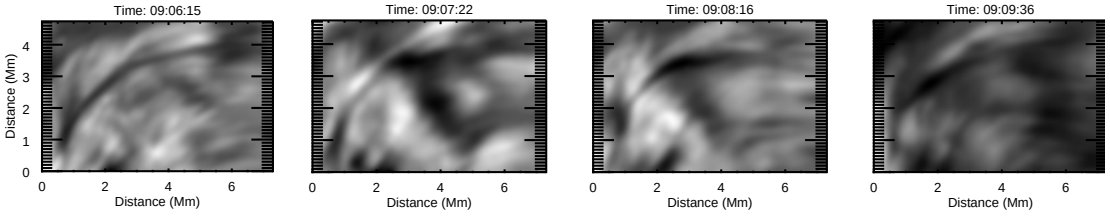

FIGURE 4.1: **Observation of fibril aligned plasma flow.** The left hand panel shows an isolated IN fibril from the H-α dataset, this fibril can be identified at (8,20) Mm in the full FOV in the line core image of Fig. 1.10. In the next panel, a parcel of plasma has formed at the upper-right end of the fibril, significantly broadening the apparent width of the feature. In the subsequent panels the dark plasma parcel appears travel along the axis of the feature (from upper right to lower left). Image recreated from (Mooroogen et al., 2017).

Interesting to note, in the time-series we observed what appeared to be an example of the flow of absorbing material along the length of an IN fibril post the feature's formation, Fig. 4.1. The time-sequence of this event begins at 09:06 and the fibril in question has pre-existed for an unknown length of time. At 09:07 a dark plasma feature has appeared in the upper-right end of the fibril and over the next few minutes begins to propagate along the feature, tracing out its central axis. However, this feature does not exhibit a line-of-sight velocity signature in the Doppler shifts or the line wings. Neither did it appear to leave a signature in line width data, although as noted in Section 3 our determination of the widths is currently limited. As an absorption feature, distinguishing its self contained edges from the rest of the fibril was difficult, making it near impossible to track this parcel through individual frames. As such an estimate for its velocity was unattainable, however crude estimates put it at 10-20 km/s, (Mooroogen et al., 2017). We suggest that this observation serves as support for the presence of a guiding magnetic field existing over an extended time period.

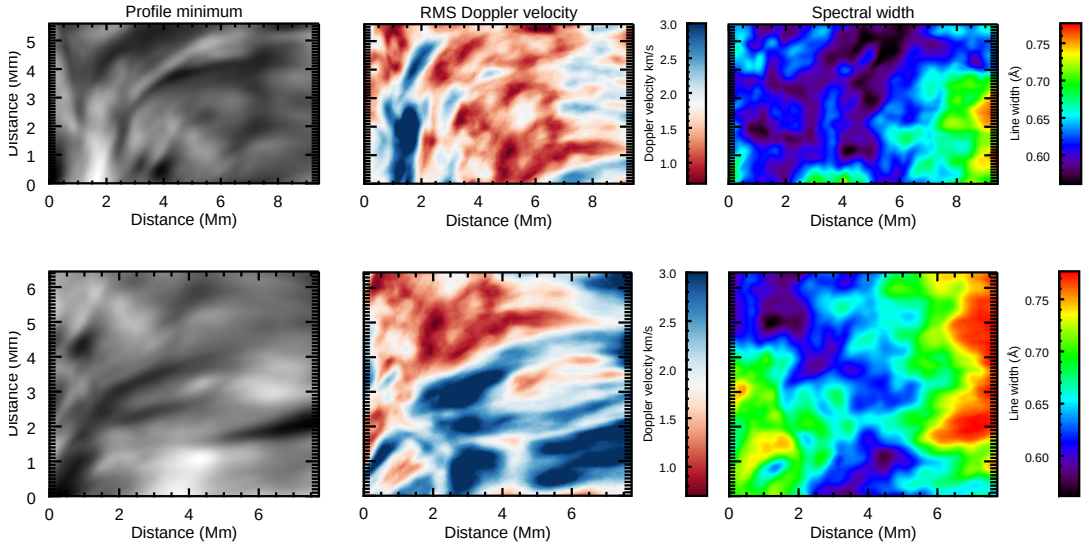

FIGURE 4.2: **Co-spatial fibril diagnostics.** From left to right the images show co-spatial diagnostics of the profile minimum, RMS Doppler velocity and line width for two different IN fibrils (top and bottom panels).

In the course of this research we have employed both LOS Doppler shift measurements and line width measurements to support our observations. These were used to examine both the transverse waves and features such as the above discussed plasma flow. Specifically, we searched for periodic variations in Doppler velocity along the axis of the IN fibrils and enhancements in line width that may act as proxy for heating events. While variations in Doppler velocity were seen in the time-distance diagrams, the periodicities observed could not be disentangled from the ambient plasma, second panel Fig 4.3. Further, applying a running mean subtraction to the data unfortunately did not remove the bulk plasma flow to reveal hidden signitures. However, we did find that RMS images of the LOS Doppler shifts show velocity field enhancements that appear to trace out the fibrils, second panel Fig 4.2. This indicates motion in the LOS component and possibly suggesting the existence of flows along the fibril.

The case for the line width appears less consistent, in the top right panel we see an elongated region with width $\sim$ 0.64 Å surrounded by a much darker area with width closer to 0.5 Å. This elongated region is approximately aligned with the fibril seen in the profile minimum (top left) and shows width enhancement relative to its immediate surrounding. However, the remaining areas in FOV show much larger width, which are not apparently correlated with features in the profile minimum. Comparison with the spectral line wing images (not shown here) showed no correlated features. In the other line width image (bottom right), there appears to be no significant enhancement aligned with the fibril in the FOV. Though again, we see regions of relatively larger widths

apparently separated by a relatively low-width parting.

Figure 4.3 displays the three diagnostics in co-spatial time-distance diagrams, transverse displacement of the fibril can be seen in the profile minimum (top). Interestingly, the Doppler velocity width and line width are very well correlated, suggesting that the line width may be a better proxy of bulk motions rather than temperature. However, it is not possible to distinguish the the oscillation, present in the profile minimum data, from the ambient medium.

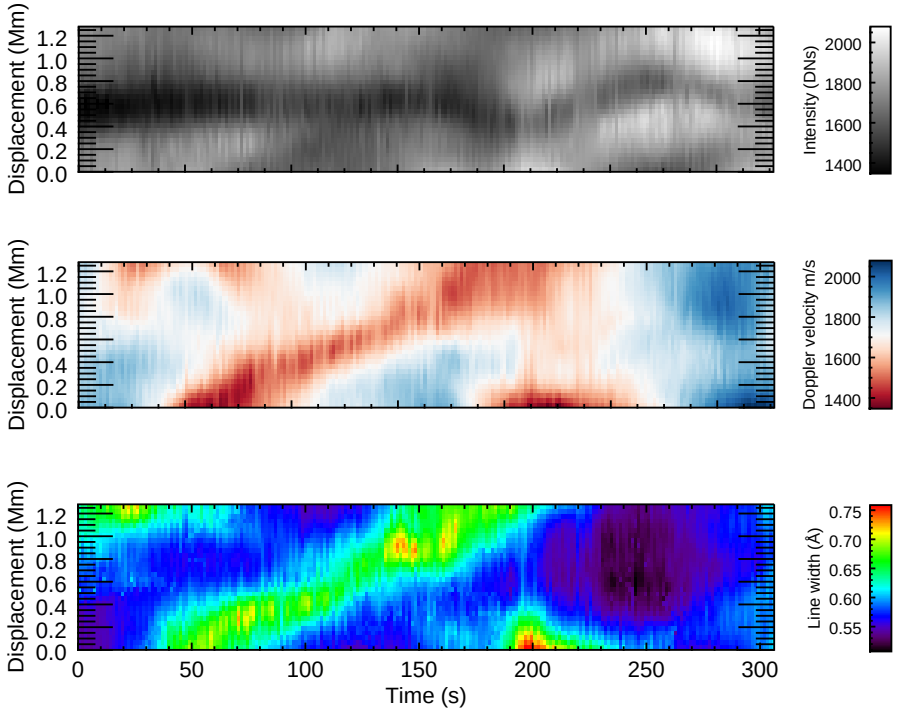

FIGURE 4.3: **Co-spatial time-distance diagrams.** Three panel figure displaying the so-spatial time-distance diagrams of an IN fibril. From top to bottom, profile minimum, Doppler velocity and line width.

4.2 Measurement of kink waves in IN fibrils

4.2.1 Time-Distance diagrams with the linear method

In order to measure oscillations in fibrils we must be able to track their position in time; to do this we create time-distance diagrams. As the name suggests these are two dimensional images of the feature, displaying their transverse displacement in time. This process starts with the identification of a fibril and then applying a cross-cut perpendicular to the feature's axis. This area is one pixel in width and can vary in length depending on the feature size and how much background context needs to be captured.

With the area defined, the data at this location in every time frame is extracted and a new image is formed with the dimensions (x, t) where t is time and x is displacement. Each pixel in time of this new image will contain a slice of length x equal to the cross-cut length.

The extension of this is to create many time-distance diagrams along the length of the structure to examine the propagation of waves. When making multiple cross-cuts, we first place a guideline along the central-axis of the structure, this guideline defines the central position from which the series of equidistant cuts will be made. A subtlety in guideline selection arises from the fact that these features evolve in time. For instance, if the guideline is placed while observing the the first frame, the location of the feature will change in subsequent frames and the guideline will be off axis. Therefore care must be taken when selecting the location. To overcome this, an average of the images is taken over the desired time-range, so that the displayed image (guide image) shows the average location of the feature. This ensures the dynamics is captured within the cross-cuts.

In the early stages of this research we used a routine called *diag slit* developed in IDL. This routine only used linear guidelines that were placed manually by the user, we refer to this technique as the linear method. Here, a guideline is placed along the central-axis of the fibril/feature and the cross-cuts are calculated perpendicular to this line. This can be seen in the left panels of Figure 4.4. The guidelines placed on the fibrils and the subsequent calculated cross-cuts are indicated by the white over-plotted lines. In the right panel we see the resultant time-distance diagrams, the height of which is equal to the length of the cross-cut and the horizontal length equal to the number of time frames used. However, fibrils can appear with a host of shapes, most exhibiting some curvilinear manifestation. This meant that the fibrils had to be measured in sections, this can be seen in Fig. 4.4 where the cross-cuts do not span the whole feature. This code was mainly used with the H-α data.

The linear cross-cuts were applied to the data with a separation distance of two pixels with the aim of minimising feature location overlap whilst still observing the dynamics. Further, using close intervals for the cross-cuts ensures that we are capturing the evolution of the wave when assessing propagation. Transverse waves are identified in the time-distance diagrams and are diagnosed as kink waves. This is shown in the examples in Fig. 4.4 where the quasi-periodic transverse displacement of the central axis is apparent. The time-distance diagrams were then processed using the semi-automated Northumbria University Wave Tracking code (NUWT). Here, the central axis of the transverse wave is tracked to develop a 1D time-series, right panels Fig. 4.4.

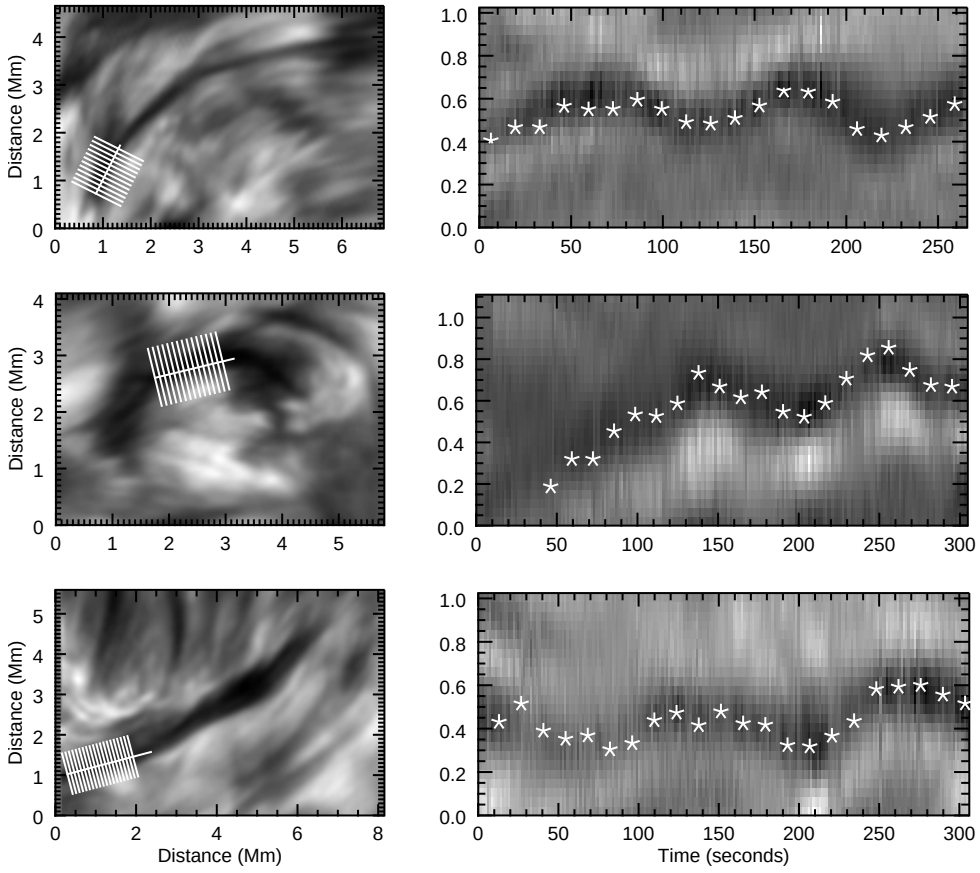

FIGURE 4.4: **Linear cross-cuts application using *diag slit*.** In the left hand panels a series of fibrils can be seen isolated in a subsection field-of-view of the H-α dataset, placed on the fibrils are the cross cuts (in white). Perpendicular lines show where the cuts are made and the guideline is axis-aligned. In the right hand panels we see the subsequent time-distance diagrams for a single cross-cut, the transverse nature of the kink waves readily visible. Over-plotted as white crosses are the tracked central-axis positions from the NUWT code, not all positions are plotted for clarity.

4.2.2 The Northumbria University Wave Tracking code

The Northumbria University Wave Tracking code (NUWT) is a purpose built routine in IDL used for tracking and measuring oscillations. The purpose of the code is to convert the oscillations observed in the 2D time-distance diagrams into 1D time-series signals. Once converted, the amplitude and periods of the waves in the time-series can be measured. For the measurement of the waves a sinusoidal model is assumed, and depending to which implementation of the code is used either a least-squares fitting (Markwardt, 2009) or Fourier analysis (FFT) is applied to determine the wave parameters. Both of these methods will be discussed as their use arises. First we will explore the conversion from a 2D to a 1D signal.

NUWT applies a simple feature tracking algorithm using a 'crawling' detector that relies on intensity gradients to search for local peaks, with the aim of tracking the central-axis

of the displaced feature. Peaks are defined as maximums in local intensity, found within a user specified search-box. To be identified as a peak, the found maxima must adhere to the criteria that the slopes either side of the peak meet some gradient value. This gradient value is set a-priori by the user. This value will be different to each dataset and some testing is required to settle on an appropriate value. Set too low and the routine will include noisy samples within the data, set too high and the routine will not find any peaks, hence this is essentially a cut-off threshold.

The location of the peaks can be measured in two ways; the first, a coarse method simply takes the location position of maximum intensity in the search box with a given error of $\pm$ 0.5 pixels. The second method employs least-square fitting of a Gaussian to the cross-sectional, which allows for sub-pixel resolution estimates of the peak location. The fitting is underpinned by the estimates in intensity formed by our multi-scale image processing techniques and alignment error. The latter method is used in the research.

Once a peak is found the search-box 'crawls' over the time-distance diagram to the next local peak, any peaks that are found are 'stitched' together based on their proximity (this criteria can also be modified by the user). The default search box is five pixels in space and four in time, this allows for small jumps in time. Joined peaks then become threads that trace out the displacement of the feature's central-axis in time. If no peak is found then the thread is said to be finished. The routine is capable of 'jumping' gaps in time if successive threads are only separated by small distances. These gaps are filled by replacing the sections with values of the previous peak and assigning a whole pixel error value. The large error values give it less weighting in the least-squares fitting when determining the wave parameters. This method should only be used with data gaps and should be used with caution. In the right hand panels of Figure 4.4, the white stared points show the locations of the tracked peaks along the features central-axis, not all points are shown here for visual clarity.

As well as setting the gradient, the minimum thread length can be defined. This establishes the smallest number of joined peaks that can be considered a thread to be passed on for wave measurement. To assist in the detection of waves, unsharped-masking can be applied to the time-distance diagrams if the contrast of the data features require enhancing. However, this is cautioned against as it will change the accuracy of the sub-pixel error measurements. Early versions of the NUWT code were semi-automated, meaning it only facilitated manual measurements of the wave parameters utilising user-guided least-squares fitting of the time-series and this method was used throughout the H-α research. Further details of the code can be found in (Morton, 2014, Morton et al., 2016, 2012a).

With the central-axis of the feature translated into a 1D signal, measurements of the wave parameters can be carried out. We assumed a sinusoidal model to characterise the individual displacement time-series $((x_i, t_i), i = 0, 1, 2...)$ apparent periodic nature. This model is described as,

$$\hat{x}(t_i) = a_1 + a_2 t_i + a_3 sin(\frac{2\pi}{a_4 t_i} - a_5), \tag{4.1}$$

where a_3 is the amplitude, a_4 is the period, and a_5 is the phase. The linear terms represent any potential long-term drift of the fibril over the course of the quasi-periodic motion, (Mooroogen et al., 2017). The amplitude and period parameters are extracted from the fitted model and the resultant co-variance matrix gives their uncertainty values. Figure 4.5 shows a tracked time-series signal with error-bars, over-plotted with a sinusoidal model using parameters measured using the NUWT code. Visual inspection and the χ^2 statistic is used as validation of the fit, this of course can lead to user-bias. Further, the limitations of the use of χ^2 to validate fitting in this manner are known and will be discussed in Section 4.3. Aside from the limitations of the statistical qualification, there is the question of whether the chosen model upholds for every thread or feature. Though the specified model can be changed, once it has been set it is fixed for all threads found. The risk here, is that important dynamics could be missed by the model, some features may exhibit multi-period waves for example. However, as a manual process these concessions are made in favour of being able to form a statical study, given the time it take to perform the measurements. Nonetheless the necessity for an automated measurement system is apparent, with the advantages of being unbiased, reproducible and facilitates easier testing between input parameters.

From the least-squares fitting the wave parameters, displacement amplitude and period are measured. The velocity amplitude, that is the speed of the transverse motion, was calculated from the measured parameters with the following standard equation,

$$v = \frac{2\pi\xi_{wm}}{P_{wm}}, \tag{4.2}$$

where v is the velocity, ξ_{wm} is the weighted mean of the amplitudes and P_{wm} is the weighted mean of the periods. For the purpose of summarising the measurements, weighted means (weighted by their uncertainties) were taken of the measured proprieties for specific features. Simply put, each fibril measured had many cross-cuts applied and therefore many time-series were made each with their own parameter measurement.

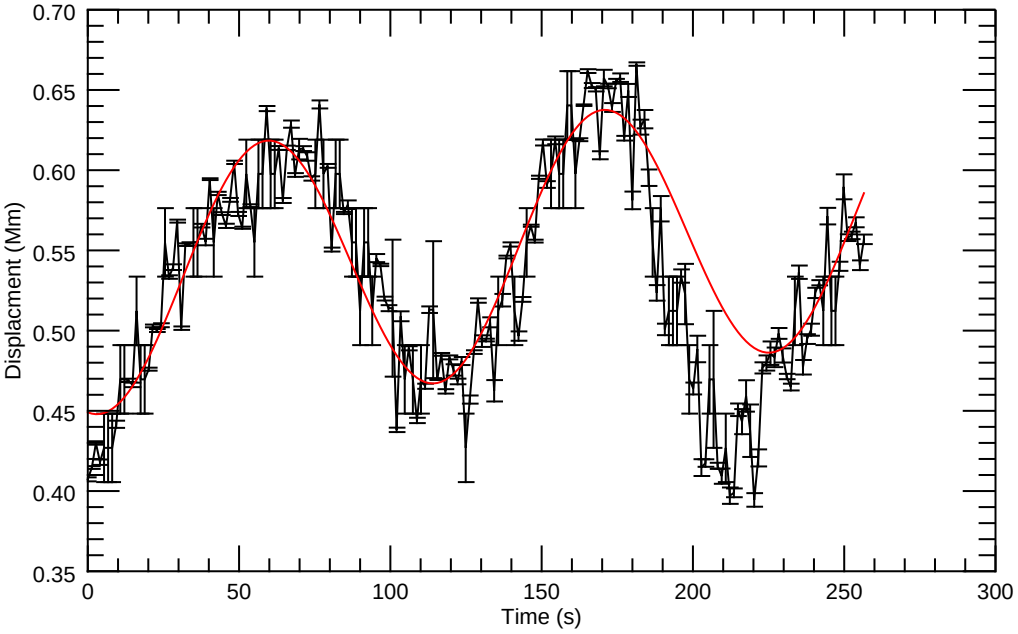

FIGURE 4.5: **Manual Fitting with NUWT.** Example result of the least-square fitting with the NUWT code. The tracked time-series exhibits transverse periodic displacement (black), error-bars from the Gaussian fitting are shown over-plotted. Also displayed is the reconstructed sinusoidal model (red) using the measured parameters from the manual fitting. It can be seen that the model resides within the limits of uncertainty in most cases, but does not capture the full signal.

To avoid labelling each measurement as a new feature we group the time-series measurements from a single feature using the weighted mean. The formula for the weighted mean is given by,

$$Wm = \frac{\sum x/\sigma_x^2}{\sum 1/\sigma_x^2}, \tag{4.3}$$

where Wm is the weighted mean of some parameter, x is some measured parameter and σ_x is the uncertainty on that parameter.

The average results of these measurements can be found in Table 4.2 and the full results can be seen in Table 4.3 of Section 4.6.

4.2.3 Measuring the propagation speed

As discussed in Section 1.5 and highlighted in Table 1.1 measurements of the phase speed of waves supported by fibrils have been limited and mostly coarse. However, with the high temporal resolution of the H-α data we have an opportunity to present a comprehensive estimate. The propagation speed is an important quality and helps determine

the type of wave we observe, i.e. whether is faster or slower than the local sound speed. To determine the phase speed we have employed cross-correlation using a method similar to that of (Gaskell, 1987) & (Welsh, 1999) and we estimate the uncertainty on the value using bootstrapping.

Cross-correlation (or in this case lag-correlation) is implemented on the successive 1D time-series along a feature obtained from the NUWT tracking code, Fig. 4.6. The shift vectors or *lags* inform on the difference in time of the associated waves and with knowledge of the series separation distance (defined as the distance between cross-cuts), the speed can be determined.

In detail, this process comprises a two stage cross-correlation method. First, the time-series are brought into phase by correlation and then summed to form a reference series. In this stage, the middle series is used as the series to which all other series are correlated against - prior to the summation. This is to ensure that it is neither too dissimilar from the proceeding or preceding series.

After the first stage, the second cross-correlation is implemented to determine the lags between the series and the reference. In this method, when the reference time-series is correlated with it's counter part in the second stage (i.e the middle series), the results are a near zero lag. These lags are then plotted against they're relative separation distances dictated by cross-cut separation and the gradient of this line indicates the phase or propagation speed, e.g. left panel Fig. 4.7.

However, a subtlety arises in that not all time-series along a feature can be used, this is a result of imperfections in the time-series. For instance, it is possible for the tracking routine to be unable to detect peaks at the same location in each time-distance diagram; possibly due to variations in signal-to-noise in subsequent time frames. This would lead to gaps in the time-series making successive series unsuitable for correlation. In these cases, we can choose which set of series to use, omitting the undesired series.

An example time-series set is depicted in Figure 4.6. Ten time-series are shown with cross-cut separation distance of 2 pixels (85 km). The propagation of transverse wave can be seen moving upwards in the y-direction of the plot between series one to seven (indicated by solid red line). The red dotted lines show the time range in which the correlation is applied; in this example series three to seven have been used in the correlation. The top three series are omitted from the correlation where it appears the wave has under-gone damping and the bottom two omitted due to subtle variations in the signals appearing as large phase speeds.

It is acknowledged that this procedure makes the assumption that there is no significant curvature of the fibril perpendicular to our view of it. Curvature of this manner would

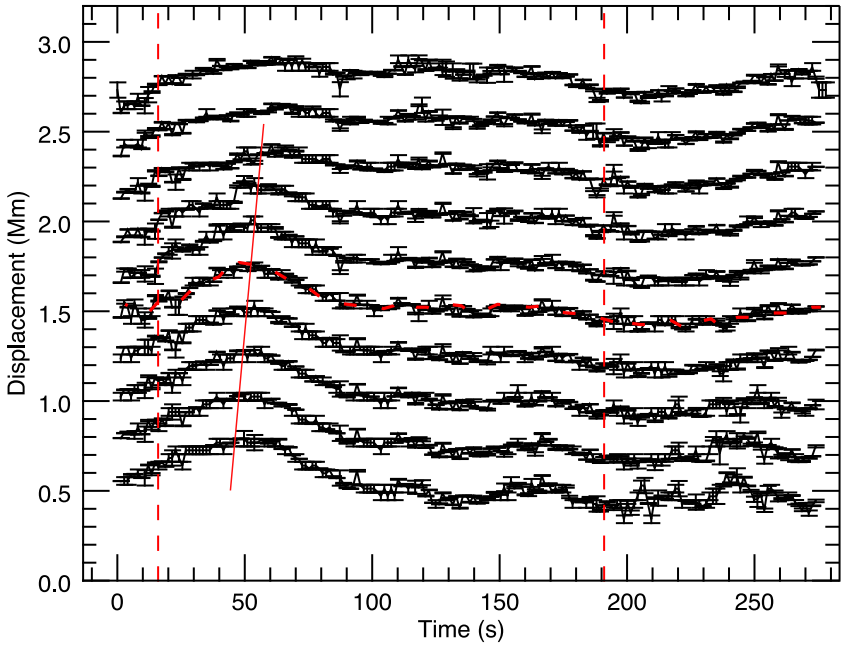

FIGURE 4.6: **Displacement time-series.** An example set of time-series taken from a single IN fibril. Each series corresponds to the measurement of the location of the feature central axis as tracked from a time-distance diagram. The relative displacements are shown at separations of 85 *km* along a fibril feature. The associated uncertainties can be seen in the error-bars. The verticle red dotted lines show the subjective time interval used for cross correlation. The solid red line indicates the direction of propagation on the first peak. In this example five time series are used for the correlation and the 'middle' time series is indicated by overplotted red dotted line. Plot adapted from (Mooroogen et al., 2017).

lead to an underestimate of the propagation distance leading to a slower phase speed measurement (Mooroogen et al., 2017). It must also be highlighted that shorter sections of the time-series are selected for the correlation, this is to ensure that neighbouring peaks that could be associated with counter-propagating waves (e.g., Morton et al., 2012a) do not influence the results. A further nuance lies in the observation of large variations in position away from the 'local average' at certain data points in the time-series. These variations appear to occur over all time-series along a feature where the data quality drops in that location. We interpret these excursions as seeing variations in the dataset (Mooroogen et al., 2017). This further impacts the time-series location chosen for the cross-correlation, as they will cause spurious results. Thus this process is rather subjective and later studies will require a more objective methodology, or perhaps a pre-processing of the time-series to prepare the data more adequately for correlation (Mooroogen et al., 2017). Despite it's subjectiveness, the results are reproducible if one uses the same time-series and correlation locations.

In order to assess the errors on the resultant lag-values, we employ the parametric

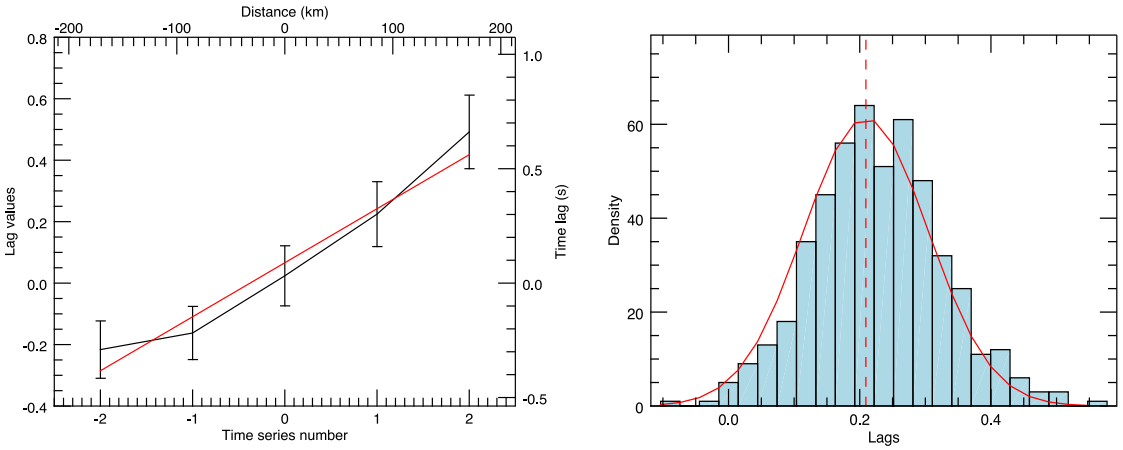

FIGURE 4.7: **Lag plot and bootstrap implementation.** The left panel plot shows the lag values as a function of time-series position. The middle time-series number corresponds to the reference series that is always close to a lag of zero. The red line shows a linear fit, the gradient of this line represents the propagation speed. The right panel shows an example distribution of lags as determined from the bootstrapping process of two correlated time-series. The red curve signifies the fitted Gaussian with a mean indicated by the vertical dashed line. The mean and standard deviation values of the Gaussian are used as the lag-value and uncertainty respectively. Plots recreated from (Mooroogen et al., 2017).

bootstrap re-sampling technique discussed in (Andrae, 2010, Andrae et al., 2010). This method is particularly useful when the underlying mathematics of an analysis has many complicated steps, making propagating uncertainties analytically difficult.

The bootstrap methodology allows us to include the heteroscedastic nature of the measurement uncertainties, σ, that we assumed to be normally distributed about the measured location, $\mathrm{N}(x_i, \sigma_i)$ (Mooroogen et al., 2017). The premise underlining the re-sampling method is to establish the distribution of an estimator in order to determine the estimators reliability, for example, standard errors and confidence intervals. Parametric re-sampling makes use of an estimated or theorised distribution of the uncertainties in the dataset. Monte-Carlo simulations are used to create artificial signals by randomly selecting values from this distribution. This removes the reliance on simplified assumptions that are needed to obtain an approximate analytic formulae needed to propagate uncertainties through convoluted operations (Mooroogen et al., 2017). Non-parametric re-sampling, does not make use of an uncertainty estimate or model of the data, instead Monte-Carlo methods are used to randomly re-select with replacement values from the processed data in order to form a 'new' sample dataset. By re-sampling from the data, the data becomes the parent population and each sample a new measurement. From this a distribution can be formed and the uncertainties inferred. Both methods are used in this research and their use becomes clearer in context. In the case of the propagation speed measurement, parametric bootstrapping is used. Later when examining the

average power spectra density non-parametric bootstrapping is used.

Here, we wish to estimate the lag-value, and understand the influence that the uncertainties of the measured locations have on this value. The application of the bootstrap methodology is to generate repetitions of the time-series with alternate values of measurement noise (established with Monte-Carlo simulation) and cross-correlating these re-sampled series. The resultant lags from this process build up a distribution, the mean and standard deviation of this distribution make up the lag and error for that single correlated series, right panel Fig. 4.7. The list of steps as described in (Mooroogen et al., 2017) are as follows;

1. Generate random noise for each displacement time-series data point (t_i, x_i) from a normal distribution, $\mathcal{N}(0; \sigma_i)$.
2. Add this random noise to the original time-series, creating a re-sampled time-series with a different realisation of the data noise.
3. Generate five hundred replicates in this manner for each time-series.
4. Cross-correlate the five hundred reference signal replicates with its counterpart from different spatial locations.
5. Establish a distribution of time-lags from the five hundred correlations, calculating the mean lag-value and its standard deviation.

The measurements of the propagation speed revealed that it is apparently constant with height across all measured features, this can be seen by the example plot in Fig. 4.7 and indicated by the linear fit without need for a higher polynomial model.

4.3 Statistical qualification

In Section 4.2.2, the concept of statistical qualification had been broached in the context of the NUWT code. Here, we will discuss the limitations of χ^2 for comparison, and examine the suitability of Equation 4.1 as a model whilst introducing the Kolmogorov-Smirnov and Runs test. Furthermore, in anticipation of the coming discussion of the automated NUWT code in Chapter 5, we also introduce the Anderson Darling and Ljung-Box tests.

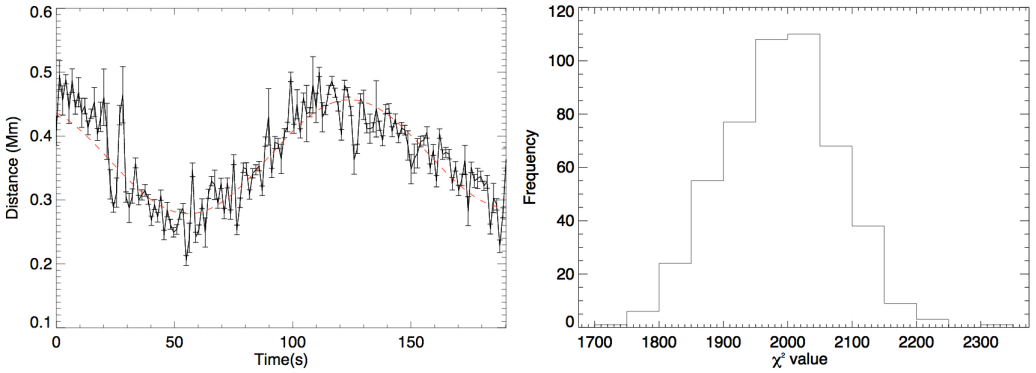

FIGURE 4.8: **Variability of χ^2.** Left panel displays an example displacement time-series of a IN fibril from the H-α dataset. The 141 data-points show the tracked position of the central-axis of the feature with error-bars over-plotted. The red dashed line overlays the best fit line as determined by least-squares fitting of the model in Equation 4.1. The right panel shows the distribution of χ^2 values resulting from 500 realisations of noise added to the time-series. Plot recreated from (Morton & Mooroogen, 2016).

4.3.1 Subtleties of χ^2

Standard model fitting practise is to examine the residuals between the test model and the data by inspecting the often revered χ^2 value resulting from some iterative least-squares algorithm designed to minimise χ^2. This can be described by

$$\chi^2 = \sum_{i=1}^{N} \left\{ \frac{y(t_i) - f(t_i, a)}{\sigma_i} \right\}^2, \tag{4.4}$$

where f is the model, N is the number of data points of $y(t_i)$ with standard deviation σ. A widely used approach to model comparison is then to compare single values of the reduced χ^2, $\chi^2_{red} = \chi^2/DOF$ (where DOF is the degree of freedom), of varying models and to choose the model with the smallest value. However, the limitations of interpreting the χ^2 value are known and as described in (Andrae et al., 2010), hence it is not always suitable method of model comparison for non-linear models.

In (Morton & Mooroogen, 2016) we highlighted the variability of the χ^2 value that is dependent on the noise within the signal. To demonstrate this, we show an example time-series (left panel Fig. 4.8) from the H-α dataset exhibiting near sinusoidal transverse displacement. This time-series has been fitted with a sinusoidal model, Equation 4.1. For each data-point of the original time-series we generate new values by randomly sampling from a Gaussian with distribution width equal to that data-points given uncertainty, (Morton & Mooroogen, 2016). From this re-sampling method, new time-series are created to realise a further five hundred time series. These new time-series are related in shape but with different values of noise, mimicking the influence of random

error on a natural measured signal. We perform the fitting using the same test model on these new series, the right panel in Fig. 4.8 displays the resulting distribution of χ^2, (Morton & Mooroogen, 2016). As discussed in Section 4.2.3, and noted in (Morton & Mooroogen, 2016), excursions from the local average in the data-points exist in the time-series. These excursions will impact the procedure and it may result in the over-estimation of χ^2, at least in this example. Figure 4.8 clearly displays the dependence of the χ^2 value on noise, as such deriving a conclusion on the suitability of a model from a single measurement is not enough. However, comparing the means of similar distributions, from the re-sampling of different test models, would provide a more appropriate method of validation.

It is clear then, that though inspection of χ^2 is informative, alone it can produce erroneous conclusions when comparing models. In the next subsection we will discuss methods that can be used to adequately test and compare models that are used in this work alongside χ^2 inspection.

4.3.2 A test of randomness

A powerful method for determining the suitability of a model to an observed dataset is to examine how the residuals compare to a model of the expected data noise. The assertion states that if a model well-represents the observed data then the residuals should follow a normal distribution, i.e. they should be displaced randomly about the mean. This is an assumption we make based on the type of data, in general the model used depends on the expected distribution of error. The test for randomness is therefore an important facet of data analysis.

The non-parametric one sample Kolmogorov–Smirnov (Lilliefors, 1969) test exists to examine the parity of one dimensional continuous probability distributions. This allows the comparison of a data sample (empirical cumulative distribution function, ECDF) with a reference probability distribution (cumulative distribution function, CDF), in this case a normal distribution. This test relies on the null hypothesis that the ECDF is from the theoretical CDF and calculates the maximum deviation between the two as the test statistic. This essentially estimates the probability for the 'true' model to produce a residual equal to that of the maximum deviation, (Morton & Mooroogen, 2016). Small values of probability then suggests that the null hypothesis is false, in other words that the residuals are not from the normal distribution.

Similarly, the Anderson-Darling (Stephens, 1974) test operates under the same methodology with differing implementation. The Anderson-Darling test performs better in the presence of outliers as it gives more weighting to the tails of the distribution. The

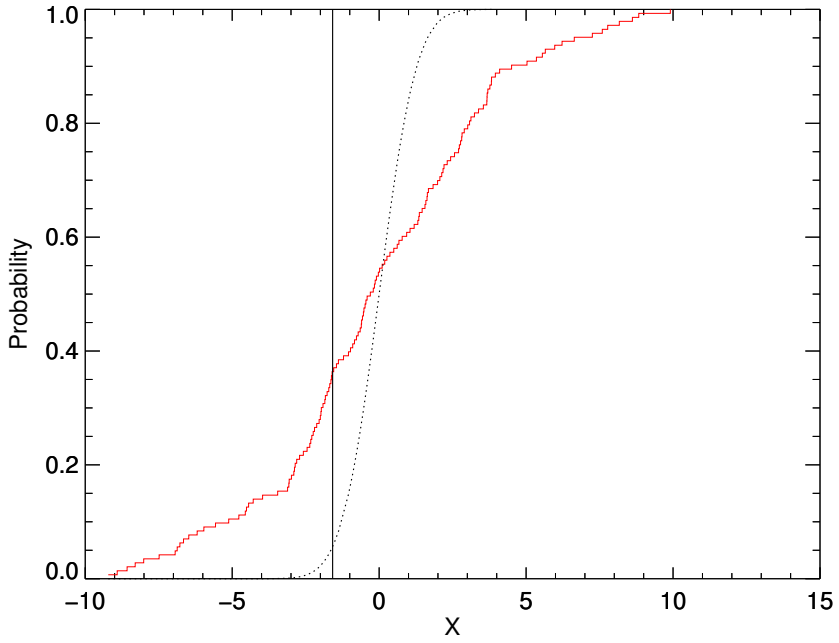

FIGURE 4.9: **Kolmogorov–Smirnov one sample test.** Test result from the Kolmogorov–Smirnov one sample test, comparing the residuals of the least-squares sinusoidal fit of the IN fibril from Fig. 4.8 to the normal distribution as a test for randomness. The red curve shows the CDF of the normal distribution, the dotted line the ECDF of the residuals. The vertical line shows the location of maximum displacement.

Ljung-Box test (Ljung & Box, 1978) however, tests the overall sense of randomness by employing cross-correlation, essentially correlating the the time-series with itself (autocorrelation) and examining if the resultant lag is different from zero. In this case the model will be assumed to be a good representation of the test data if the autocorrelation is zero, random data has a maximum lag at zero.

The Runs Test is an easier implemented test for randomness, it tests the hypothesis that a binary population resembles random sampling and hence test that the sample is from a binomial distribution. This requires the test residuals to be converted into a binary sample based on their distribution about the mean (zero), e.g. positive values set to one and negative values set to zero. The test calculates the weighted difference in the observed number of runs and predicted number of runs. Here a 'run' is defined as having consecutive values in the sample, for instance a sample of (1111001111110000011) would have five runs. Mathematically the test is given by,

$$Z = \frac{R - \bar{R}}{\sigma_R}, \tag{4.5}$$

Where R is the observed number of runs, $\bar{R}$ is the predicted number of runs and σ_R is the standard deviation of the number of runs, defined as,

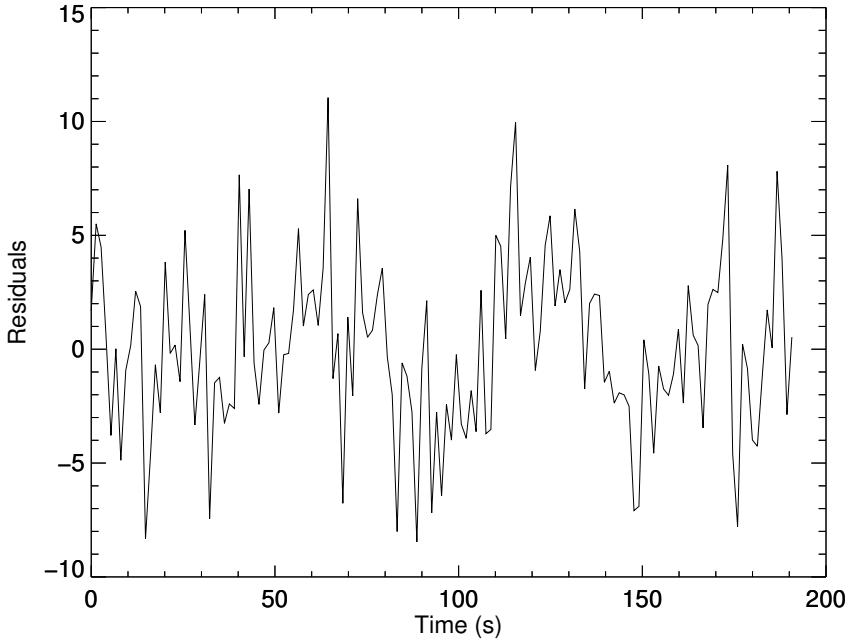

FIGURE 4.10: **Residuals.** The residuals shown here are calculated as the difference between the data sample (time series as shown in Fig. **??**) and the test model (equation 4.1). Oscillatory behaviour can be seen throughout indicating the applied model is inadequately capturing the dynamics.

$$\bar{R} = \frac{2n_1n_2}{n_1 + n_2} + 1, \tag{4.6}$$

and

$$\sigma_r = \frac{2n_1n_2(2n_1n_2 - n_1 - n_2)}{(n_1 + n_2)^2(n_1 + n_2 - 1)} \tag{4.7}$$

where n_1 and n_2 refer to the number of each binary point (i.e. the total number of 1's or 0's). The test rejects the null hypothesis if Z is larger than 1.96, i.e. a 5% significance level.

The one sample KS test and Runs test have been employed here to assess the suitability of the sinusoidal model for the manual fitting, Fig. 4.9. Here it can be seen that the residuals ECDF (dotted line) deviates (maximum deviation shown by the vertical line) significantly from the CDF (red line) with a probability of 8×10^{-11}. The curves would would be same (not realistic) if the model perfectly represented the data. Similarly the Runs test produces a probability of 1×10^{-10}. Here, we tested the model shown in Equation 4.1, and found that the criteria of normality was not met. Further tests are required to examine alternate sinusoidal models, for example double and triple sine

functions possibly with linear and quadratic functions. We can see in Fig. 4.10 oscillatory behaviour in the residuals indicating the provided model does not capture the full dynamics, further highlighting the possibility of non-sinusoidal displacement.

Without an alternative model to turn to we pursue with sinusoidal function with the knowledge of it's limitations as a caveat in interpretation. It may be that alternative, non-parametric methods such as empirical mode decomposition or principal component analysis can provide better inspection. Alternatively, as the least-squares fitting depends on the errors, the poor fit could be a result of an underestimation of the uncertainties provided by the alignment error and multi-scale processing. However, in the case of the Fourier analysis where the uncertainties do not play a role, the signal measurement from a low cadence dataset is likely to be missing dynamics.

4.4 Fourier analysis

It was established with the use of KS1 statistics that a single sinusoidal function does not best represent the dynamics of the measured signal, hence we turn to Fourier analysis to assess the possibility of multi-periodicity of the IN fibril kink waves. In this section we set out the methods used for this investigation, and we begin with some background of Fourier analysis.

Much like wavelet analysis, the Fourier transform (FT) decomposes a signal into its constituent frequencies, however with sinusoidal basis functions. It is often used in signal-processing to convert a time-series into frequency-space. Mathematically, it is formally defined as,

$$\hat{f}(\nu) = \int_{-\infty}^{\infty} f(t) e^{-2\pi i \nu t} dt, \tag{4.8}$$

where $f(t)$ is a real function in the time domain t and $\hat{f}(\nu)$ is the Fourier transform of $f(t)$, a complex function in frequency domain ν. At $\nu = 0$ the Fourier transform is simply the integral of $f(t)$ and therefore is the average of $f(t)$. Recalling the discussion on filters in subsection 3.3.1.1, conceptually the Fourier transform filters a signal to determine the frequencies that form it.

In order to plot the power of the Fourier transform, as it is a complex function, we must plot $|\hat{f}(\nu)|^2$, this is known as the spectral power and is described as the energy contained at each frequency. The spectral-power-density (PSD), a unit often quoted, can be defined as the spectral-power per unit frequency. Figure 4.11 displays an example PSD for a displacement time-series of an IN fibril. By extracting the signal, $\hat{f}(\nu)$, at

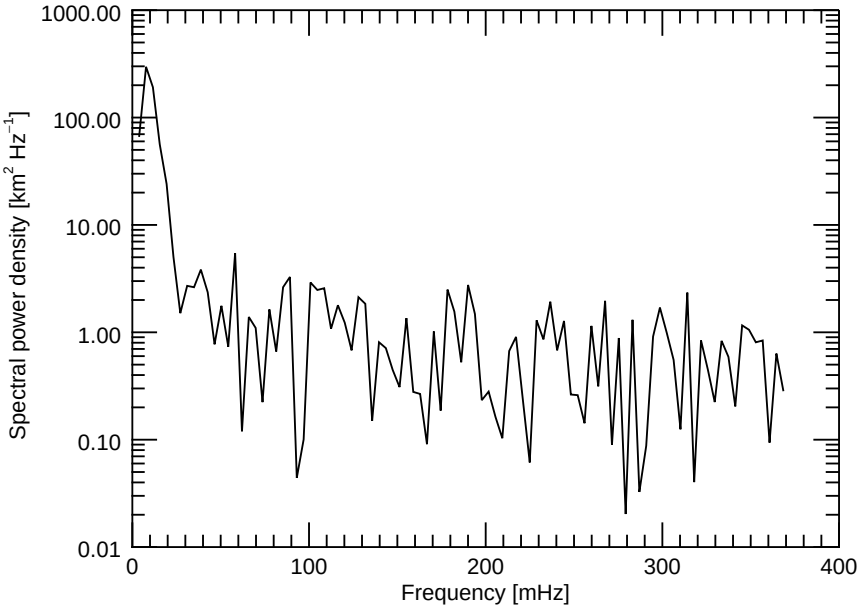

FIGURE 4.11: **Power spectral density plot.** Displayed here is the PSD for a displacement time-series of a signal IN fibril, the y-axis is plotted on a log scale. Peak power (large spike) can be seen at the lowest frequencies and the flatter part of the spectrum at higher frequencies is indicative of white noise.

the frequency bins where power is largest, a time-series signal made up of the primary components can be created omitting the 'redundant' frequencies. The flat part of the spectrum, at the higher frequencies is distinctive of white noise.

In Figure 4.12 we see an example time-series and examples of its frequency components as extracted via the Fourier transform. The red-line over-plotted on the top image shows the summation of the frequency components reconstructing the signal. In the subsequent panels we see the existing sine waves at different frequencies in the signal.

The fast Fourier transform (FFT) is a computational method to implement the FT expediently, and there are a few computational subtleties that go along with it. Spectral leakage is the manifestation of spectral power 'leaking' into neighbouring frequency bins. This occurs due to the finite frequency resolution of the discrete FFT. The FFT assumes the measured signal is continuous but it is in fact a finite measured time-interval. When this measured interval is limited, such that the sampling rate misses a full period, sharp discontinuities arise. The FFT juxtaposes the measured signal at these discontinuities and the FFT signal becomes spread out amongst the discrete frequency bins. A simple method to prevent leakage of the average from the zero frequency bin is to subtract the mean of the signal before taking the Fourier transform (Heinzel et al., 2002).

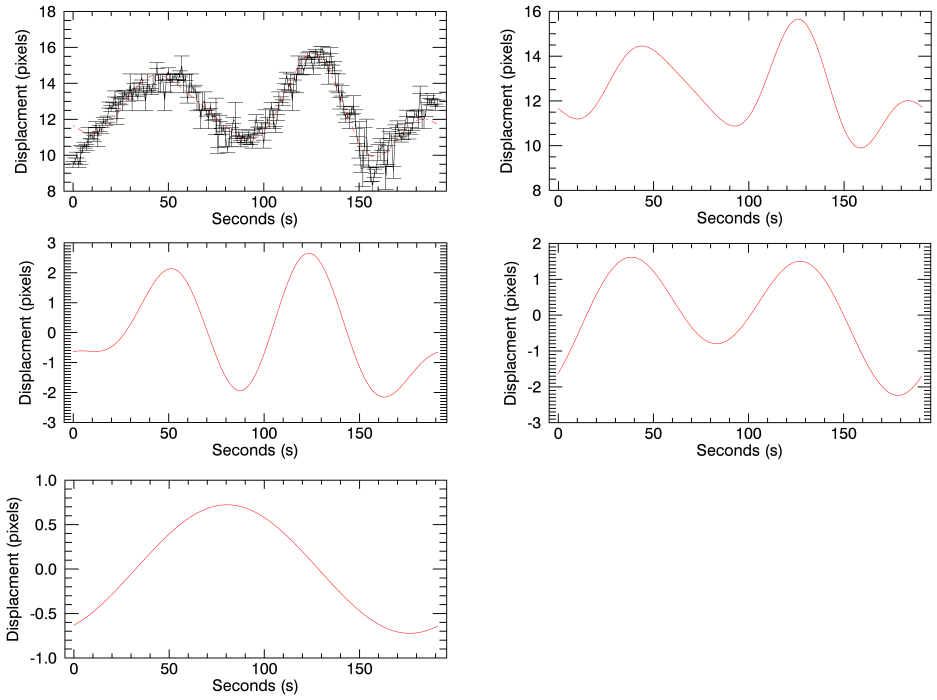

FIGURE 4.12: **Fast Fourier Transform.** Top panel depicts the displacement time-series from an IN fibril with error-bars as calculated from the multi-scale processing. Over-plotted in red is the reconstructed signal using only the the first four frequency components from the Fourier transform. Each successive plot shows the same reconstructed signal with a single frequency component removed, at each level the highest frequency is removed until the final plot shows the frequency that holds the highest signal power. The PSD of this signal can be seen in Fig. 4.11.

Moreover, a widely used method to overcome leakage is windowing, which essentially reduces the discontinuities at the signal edge to zero. As such, the type of window chosen to accomplish this depends on the shape of the measured signal and where these discontinuities exist.

Another technique used in FFT analysis is zero-padding; this technique adds a series of zeros at the end of the time-signal to increase the number frequency bins that appear more closely spaced in the resultant signal. Though this does not boost the FFT resolution, it creates a signal that is smoother in appearance and may help visually identify peaks. Zero-padding can also be used to increase performance speed of the FFT, however it can also increase spectral-leakage and should be used with care.

4.5 Multi-periodicity in IN fibrils

With the necessary background of Fourier analysis in hand, we continue on to test for non-sinusoidal behaviour and the possibility of multi-periodicity.

TABLE 4.1: Colour list for Fig 4.13

Colour	Distance (km)
Black	-
Blue	85
Green	171
Orange	256
Gold	342
Sky blue	427
Pink	512
Purple	597
Brown	683

Figure 4.13 (middle panels) show over-plotted power spectral densities for a set nine time-series from three different IN fibrils (top to bottom respectively). Each PSD corresponds to a time-series from cross-cuts placed at increasing heights. As such, each curve colour (from black to purple) corresponds to an increase in height along the feature, from endpoint to fibril centre. The order the colours are shown in Table 4.1 and the distances are given to the nearest km, as measured from the first placed cross-cut. The left panel images show the fist time-series from the set of nine, that correspond the to PSD's (black curves). The fitted model from Equation 4.1 is over-plotted on the time-series and the PSD of this model can be found over-plotted in the middle panels (both in red). In the case of the model PSD, a white noise component is added to form an artificial signal. This is calculated by randomly re-sampling about the estimated time-series uncertainty.

In each PSD plot, power appears to be distributed across a number of bins; this can be seen from the downward slope that proceeds the peaks (0-1 mHz). This could be interpreted as a signature of a power law with an apparent red noise spectrum. If the kink waves were indeed single period waves, we would expect the Fourier transform to appear as a single peak with additional noise.

In order to asses the significance of this slope, we can compare the PSD's with a model that represents an artificial signal. In this case, the model is that of Equation 4.1 with an added white noise term. The parameters of the model are given by the least squares measurements from the manual NUWT code. With this, we can test how well our assumed mode of a single period sinusoid represents the dynamics of the real signal.

The employed method follows that of (Vaughan, 2005). First, we take the ratio of the power spectra and the model power spectra, if the model is a good fit of the data the ratio should follow a χ^2_2 (subscript denoting degrees of freedom) distribution. Therefore, large variations of the ratio would indicate that the model is a poor fit and that there is less probability that the peaks found occur by chance. Here, we have defined this dimensionless ratio as the function f, and it is plotted in the right hand panels of

Fig. 4.13. Explicitly, f is the ratio of the first PSD (black curve, which represents the first time series in a set) and the single period model given by Equation 4.1 (with noise) multiplied by a factor of two. From the f plots, large variations can be seen in the 0-1 mHz region and this could suggest multiple frequency components or indicate non-linear behaviour.

As the ratio f follows a χ^2_2 distribution we can estimate the probability that these variations will occur given the assumed model, (Vaughan, 2005). Here, we can define a confidence limit on the ratio f for a value at a given frequency as the probability that f is larger than the critical value by chance, given that the null hypothesis is true. The null hypothesis is defined as the circumstance that the observed variation cannot be distinguished from noise. At a 95% significance level the critical value for a χ^2_2 is 5.99, the largest peaks in the 0-1 mHz range of the first and third panels exceed this value however the middle panel does not. This means that for the top and bottom panels, the probability that the large peaks in f will occur given the null hypothesis is less than 5%. However for the middle panel where the peak has a value of 4.8, the probability is only 9%. At the very least the ratio shows that a sinusoid plus noise model in not a good description of the observed displacement.

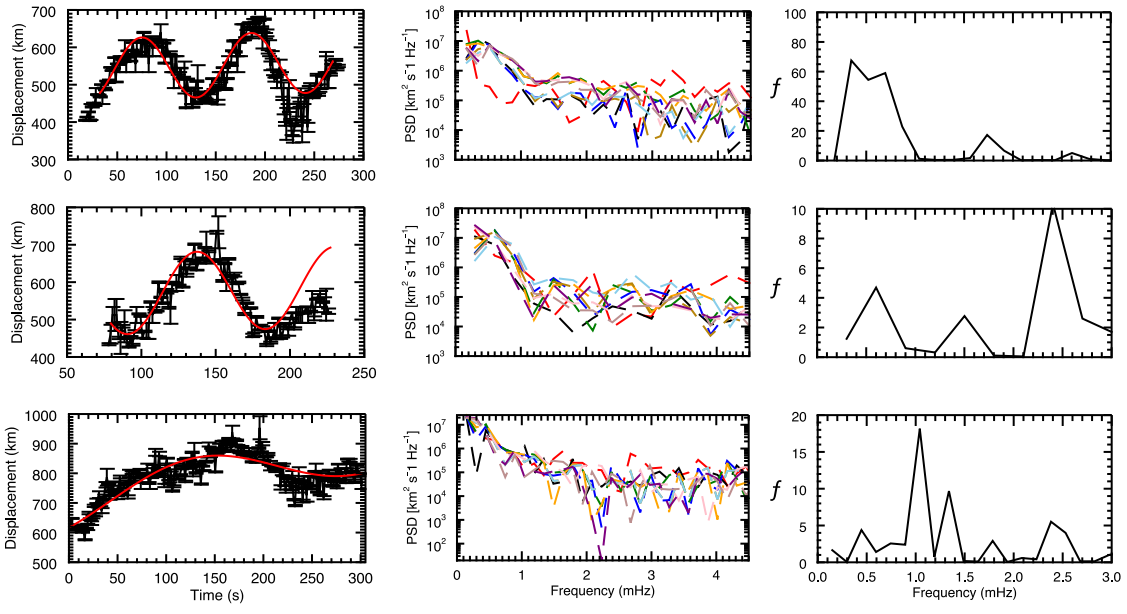

FIGURE 4.13: **Multi-periodicity in IN Fibril.** In the left panels, example time-series from IN fibrils with over-plotted least squares fit (red) from Equation 4.1. Middle panels, PSD's of the time-series (left) and subsequent time-series along the same fibril. The PSD's are coloured from black to purple in order of height along the fibril, see Table 4.1. Over-plotted on the PSD's (in red) is a model PSD of a single period sinusoid of Equation 4.1 with additive white noise. Finally, the right panels show the ratio (f) of the PSD (black curve) and the PSD model line.

Often kink waves are modelled as mono-periodic waves, including early parts of this research where sinusoidal fits had been applied to the time-series to extract parameter estimates. If the evidence presented here are in fact signatures of multi-periodicity, then the single period sinusoid model is missing important dynamics. Moreover, if this behaviour turns out to be prevalent amongst other chromospheric features, it would potentially lead to the underestimation of energy flux, with the single sinusoid only capturing a fraction of the total power.

An additional feature observed in the second and third PSD plots of Fig. 4.13, is that there appears to be a reduction in power (seen in the amplitudes) with distance along the fibril. This is possibly an indication of wave-damping, though in the top panel there appears to be some level of amplification with the purple PSD above the black.

4.6 Results

4.6.1 NUWT results

Histograms in Figure 4.14 summarise the results of the measured properties. The distributions of the displacement amplitude, period, velocity amplitude and the phase speeds can be seen. It is important to note when interpreting the histogram that the spatial resolution per pixel in the dataset is 42 km and Nyquist period is 2.7 s.

The amplitude and period measurements (and hence velocity amplitude) are the results of the weighted means from each feature. The amplitudes and period distributions appear asymmetrical, this resembles the distributions of transverse waves found in a host of studies, (Morton & McLaughlin, 2014, Morton et al., 2015, 2013, 2014) in a variety of atmospheric regions. Gaps appearing in the period distribution could possibly be filled by further measurement.

The average and standard deviations of the distributions can be found in Table 4.2, in general these results appear consistent with previous fibril measurements as seen in Table 1.1. However, the propagation speeds are greater than those measured by

TABLE 4.2: H-α average wave properties (Mooroogen et al., 2017)

	Mean	Median	Standard deviation
ξ (km)	85	78	43
P (s)	128	122	43
v (km/s)	4.22	4.21	1.6
Propagation speed (km/s)	446	399	338

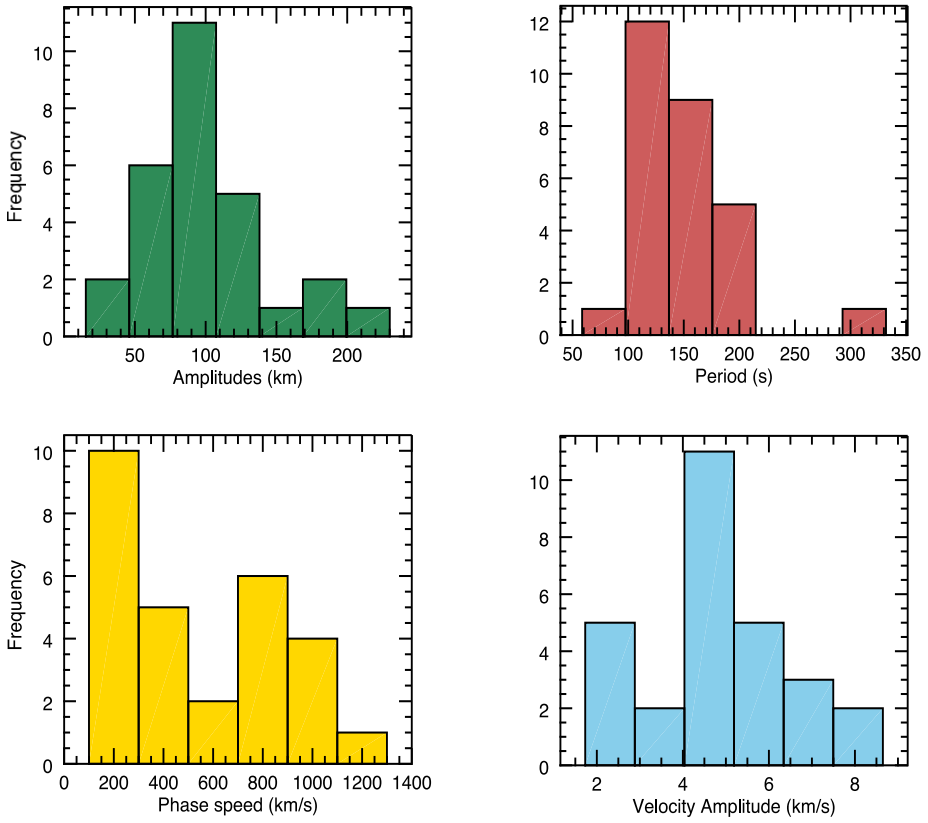

FIGURE 4.14: **IN fibril parameter histograms.** Histograms showing the weighted means of the displacement amplitude, periods, velocity amplitude and the total distribution of the phase speeds of the twenty eight measured fibrils. Plot recreated from (Mooroogen et al., 2017).

(Jafarzadeh et al., 2017b) in slender active region Ca II fibrils and also our measurements of fibrils in the Ca II sunspot super-penumbra, subsection 5. We have also measured phase speeds in excess of 500 km/s, which is substantially large compared to the local Alfvén speed (10's of km/s). This value has an equally large error associated with it, and could be spurious due inhomogeneities in the time-series such as fixed artefacts as discussed in Section 4.2.3. Alternatively, large values could indicate either large magnetic fields or low density regions (relative to those that would produce lower phase speeds).

4.6.2 Average power spectral density of the quiescent H-α chromosphere

In both studies, H-α and Ca II, we estimate the average power spectral density of the kink waves evident in each dataset, developing what we call a chromospheric power spectra. To do this, we create scatter plots of the PSDs from the displacement time-series of

every unique fibril feature available in each set of data. Prior, we take the derivative of the displacement time-series to produce a PSD of the horizontal velocity power spectra, this is to make the results comparable to measurements of (Morton et al., 2014) and (Stangalini et al., 2015). To establish the average of the combined PSDs, the data is separated into frequency bins and an average of the power in each bin is calculated. The choice of bin width should be that so any evident peaks in the combined spectra are not 'blurred' out, this process requires some testing.

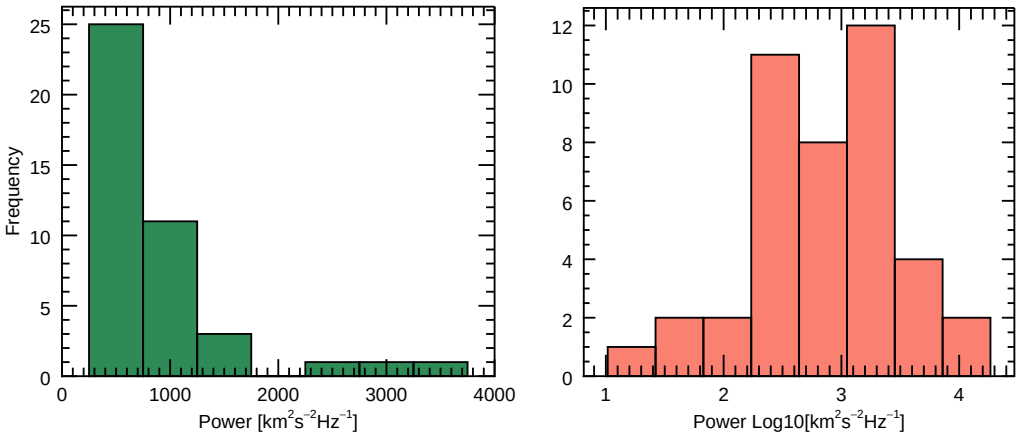

FIGURE 4.15: χ^2 **distribution of power.** Left panel shows the χ^2_2 distribution of power within frequency bin 0.29-0.30 Hz of the combined PSD scatter plot. The right panel shows the logarithmic base ten of the same distribution, notice the change in spread of data.

The distribution of power in each bin follows a χ^2 distribution that is approximately lognormal, left panel Fig. 4.15. Calculating the mean of this distribution would put weight of the average into the tails, due to the small sample size. To overcome this, we take the logarithm (base 10) of the power to re-distribute the data, see right panel Figure 4.15. The arithmetic mean is then calculated and subsequently converted back into 'real' space to form the average power in that frequency bin. However, this method is subject to a constant bias as discussed in (Vaughan, 2005), and requires a linear correction before conversion from log-space. With this method we have assumed that the distribution of PSD points does indeed follow a χ^2_2 distribution, though this has not been statistically confirmed. In this instance a two sample Kolmogorov–Smirnov would be appropriate to test this hypothesis and will be carried out in future work. A final caveat to establish is that we have employed an equal frequency bin width in which to form our average, and it is clear that more data points exist in the higher-frequency regions. Therefore, the spectral averages may be better estimated in the high-frequency range than the low-frequency.

We repeat the procedure for each frequency bin and an average PSD is formed. To estimate the error of these average points we turn to parametric bootstrapping. In this context we wish to establish an uncertainty of the mean value of power within a certain frequency bin range. The implementation of this bootstrapping technique is as follows; first we randomly re-sample data with replacement from the log distribution of power, we do this five hundred times. This produces five hundred lists of PSD points from that frequency bin, the arithmetic mean is then taken of each list revealing five hundred means. Then, the standard deviation of the distribution of those means is calculated and forms the error for the average power of that frequency range.

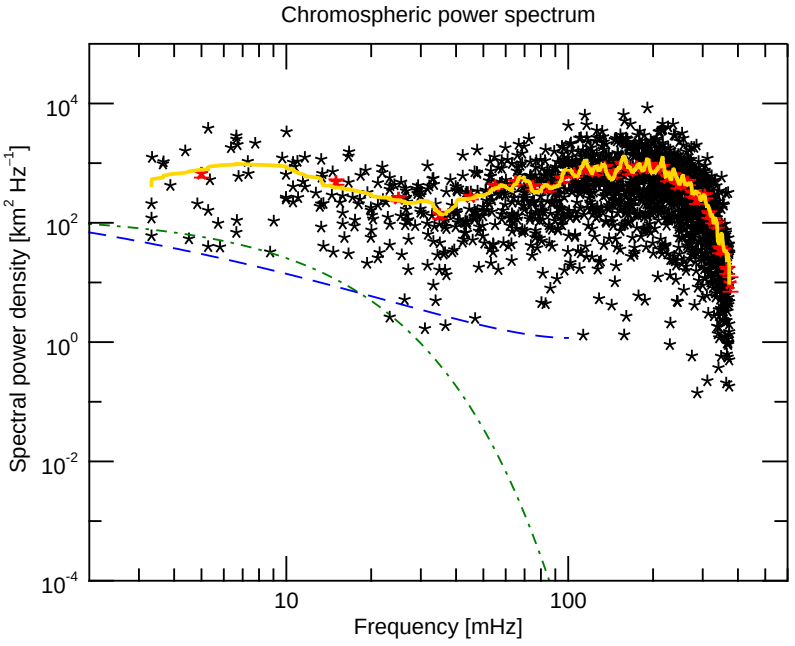

FIGURE 4.16: **Average chromospheric power spectra.** Depicted here is the velocity PSD scatter plot from time-series of nine IN fibrils shown in black. The over-plotted red points show the calculated average of the PSD from respective frequency bins, the gold curve shows a smoothed line through the scatter plot. Plotted on the same graph are the two velocity PSD of the quiet sun photosphere from (Chitta et al., 2012).

Here, we present the average PSD for the wave power in the quiescent H-α chromosphere as measured in this dataset. Figure 4.16 shows the horizontal velocity power spectra scatter plot (black), which is the combination of PSDs of time-series from the nine unique fibrils. The average power spectral density with associated error-bars is over-plotted in red, this is calculated from combined frequency bins of width 10 mHz. The gold line is a smooth trend, calculated using a Gaussian kernel of with nine. Majority power can be found at the lower frequencies before a subtle downward turn as the spectra reaches the 40 mHz mark. At the higher frequencies the PSD takes a rapid downward turn. Studying the average power spectra density can be an insightful tool when compared

to PSD in other layers of the solar atmosphere, especially when assessing the transport of non-thermal energy through these layers. As such, we compare our PSD for the H-α chromosphere with velocity PSD's from, (Chitta et al., 2012), of quiet H-α photospheric bright points. (Chitta et al., 2012) present two curves, each resultant of different fitted functions to the PSD data, a Lorentzian model (green) and a function that is described as, 'sum of the true correlation of solar origin' (blue).

The (Chitta et al., 2012) PSD curves display power approximately a factor of ten smaller than our chromospheric PSD. This suggests an amplification in power from the photosphere to the chromosphere. Such a result is readily explained by the gravitationally stratified density profile of the atmosphere, where we would expect amplitudes to increase with height. If the chromospheric PSD had been less than that of the photospheric, we could perhaps conjecture that damping had occurred. However, it may not be possible to single out damping in this manner when the datasets are not correlated from a single observation and without further knowledge of atmospheric parameters. (Stangalini et al., 2015) noted similar amplification in power from photospheric (Fe I 6300 Å) and chromospheric (Ca II H 3969 Å) quiet sun velocity PSD.

4.6.3 Magneto-seismology

The exploitation of magnetically-guided wave parameters to infer physical properties of the local plasma is not uncommon and kink waves have been employed readily to attempt this (e.g., Guo et al., 2015, Morton, 2014, Morton et al., 2012b, Pant et al., 2015). However, magneto-seismology relies on a set of theoretical assumptions that may not be suitable in all regimes, though it is not always clear where this is the case. Therefore, caution is required when interpreting the results, despite this it remains useful to compare observations with current theory to aid in our understanding. Recalling (Verth et al., 2011), we can utilise the properties (amplitude and phase speed) of the magnetically-guided kink waves to understand the variation of the local plasma density and magnetic field strength. To do this we first refer to the WKB solution (method for approximating a solution of differential equations) to the wave equation governing a kink wave propagating a stratified flux tube under the thin flux tube approximation, (Mooroogen et al., 2017, Morton et al., 2012b), given as,

$$\xi(z) = C\sqrt{\frac{c_k(z)}{\omega}}R(z), \tag{4.9}$$

where $\xi(z)$ is the displacement amplitude as a function of height (z) along the feature, $c_k(z)$ is the phase speed or kink speed as a function of height, ω is the angular frequency,

$R(z)$ is the radius of the flux tube and C is a constant. This solution relies on the assumption that the longitudinal changes in the plasma and magnetic field strength are small compared to the wavelength, we recognise that this may not be the case for chromospheric wave-guides. Further assumptions underpinning Equation 4.9 are the notion of hydrostatic plasma and zero wave damping. Following the methods in (Morton, 2014) we derive from Equation 4.9 the following relations, describing the relative evolution of the normalised radius, plasma density and magnetic field strength in a stratified flux tube.

$$\frac{\langle\rho(z)\rangle}{\langle\rho(0)\rangle} = \frac{\xi(0)^4}{\xi(z)^4} \tag{4.10}$$

$$\frac{R(z)}{R(0)} = \sqrt{\frac{c_k(0)}{c_k(z)}}\frac{\xi(z)}{\xi(0)} \tag{4.11}$$

$$\frac{\langle B(z)\rangle}{\langle B(0)\rangle} = \frac{c_k(z)}{c_k(0)}\frac{\xi(0)^2}{\xi(z)^2} \tag{4.12}$$

These relations depend entirely on the displacement amplitude and phase speed, where ρ is the plasma density and B is the magnetic field strength. As previously stated and shown in Figure 4.7 the measured phase speeds were determined to be constant over height (z) leaving the phase speed terms in Equations 4.10 to 4.12 as unity. This leads to the relations to be entirely dependent on the measurements of the displacement amplitude. However, in a hydrostatic atmosphere density is stratified, hence in a vertical flux tube density will drop off exponentially. As such, depending on the true nature of the IN fibrils these quantities will be reliant on the fibrils inclination to the vertical. If we consider a loop-like (semi-circular e.g. Dymova & Ruderman, 2006) structure for the fibril in a hydrostatic atmosphere then the density variation looks like,

$$\rho(z) = \rho_0 exp\left(-\frac{L}{\pi H}cos(\frac{\pi z}{L})\right), \tag{4.13}$$

where z is the distance along the loop, H is the scale-height and L is the loop length (Mooroogen et al., 2017). Stratification of density in this manner will lead to upward propagating waves exhibiting an amplification and downward propagating waves showing attenuation, reflected in the relation of Equation 4.10.

Figure 4.17 depicts the magneto-seismology inversions for the density profiles (Eqn 4.10), the two plots separate the profiles by the direction of wave propagation. Waves that were observed to propagate away from an observed fibril endpoint (upward) are shown

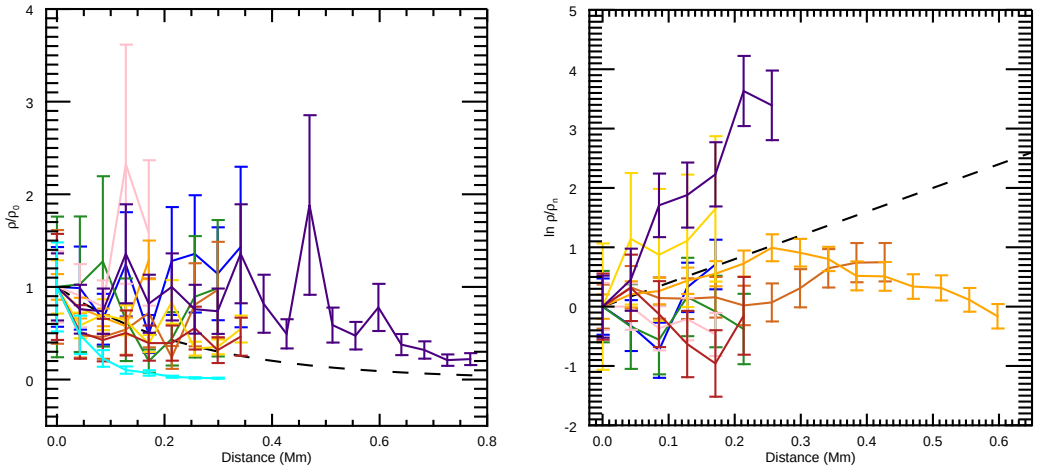

FIGURE 4.17: **Magneto-seismology inversions: Density profiles.** Profiles shown here display the relative change in density along the length of the IN fibrils as given by Equation 4.10 (relative to the first data point i.e. the amplitude measurement from the initial time-series at the base of the fibrila). Each solid curve represents a density profile calculated for a time-series using their amplitude values. The dashed line represents a model chromospheric density profile with scale height 250 km. The profiles are separated into two plots depending on the direction of the propagation towards (right) or away (left) from a feature foot-point assuming a shallow loop-like structure. To do this the curves in the right plot were re-ordered by normalising them to the last value of relative density in each respective profile. This is represented by the subscript n on the right axis. The subcript 0 on the left plot axis is to signify that the profiles adhere to equation 4.10. Plot recreated from (Mooroogen et al., 2017).

in the left panel, where as waves observed to the propagate towards an endpoint (downward) are shown in the right panel. The cross-cuts (and therefore the displacement amplitudes) were all measured from the direction of the ends points towards the fibril centre. However, it was found that some of the waves propagated in different directions (either towards the fibril centre or away), this was determined from the phase speed gradient.

In order to compare the profiles from oppositely propagating waves, we re-order the measurements. The profiles in the right hand panel were normalised by the last value of relative density in each respective profile, this is represented by the subscript n in the y-axis of the right plot. This essentially changes the reference point of measurement from the endpoint of the fibril to the centre. The profiles were then reversed so that the measurements start from the endpoints. Reversing the profiles in this manner has allowed us to display the profiles in the same direction as the left hand plots, i.e. along the height of the feature towards the centre of the fibril. The downward propagating profiles are also plotted as the natural logarithm of the relative profiles to aid in visual clarity due to the large variability in the profiles.

With the assumed shallow loop-like geometry of the IN fibrils, we interpret the approximate centres of the fibrils to be higher in the atmosphere relative to the endpoints. Therefore, while discussing profiles that propagate away from an endpoint we are assuming an ascension in the atmosphere and the opposite for those propagating towards an endpoint.

A model exponential density profile is over-plotted (black dashed line) with a scale-height of 250 *km* (Uitenbroek, 2006). This line represents the maximum density variation in the atmosphere at this scale-height according to the model in Equation 4.13. Figure 4.18 displays the inversion profiles of the flux tube radius and magnetic field strength (Eqns. 4.11 and 4.12). As discussed earlier, these relations are dependant on the measured displacement amplitudes of the profiles and are proportional to each other. The profile colours are consistent with those of the density plot.

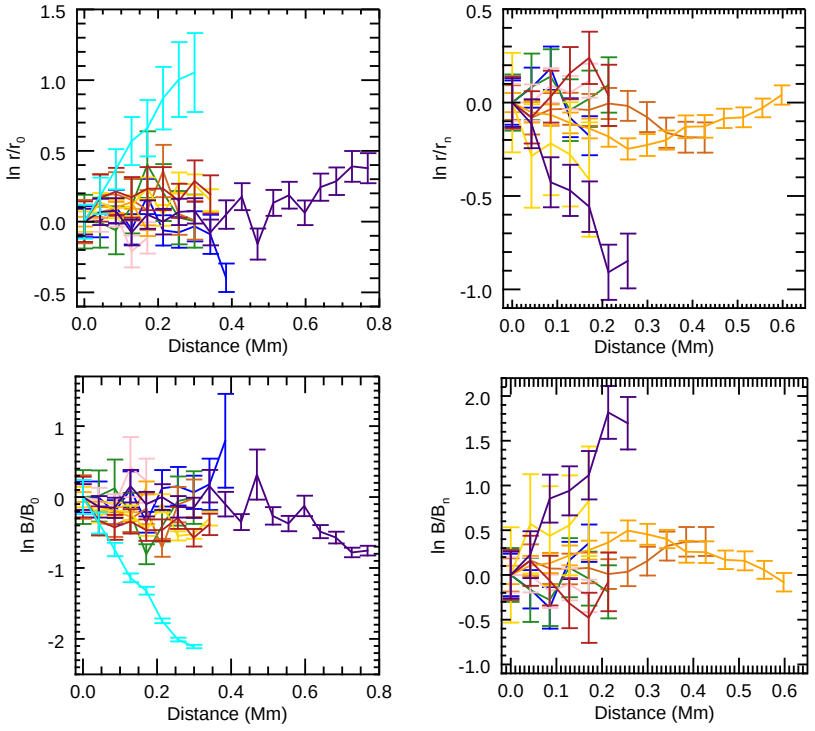

FIGURE 4.18: **Magneto-seismology inversions: Flux tube radius and magnetic field profiles.** In this four panel plot the relative flux-tube radius (top) and relative magnetic magnetic field strength (bottom) are separated into two denominations in the same manner as the density profiles. The profile colours are consistent for the measured IN fibrils in the previous plot.

Despite the large variability, the profiles indicate a trend in the wave amplitudes with height. This suggests some level of vertical stratification in density and magnetic fields of the IN fibrils and ambient plasma rather than being horizontal features in the chromosphere. In both sets of plots, the upward and downward propagating, there exists some

correlation of the inversion profiles with the model line from the hydrostatic density profile. The pink and blue inversion profiles in Fig. 4.17 left panel (upward propagating) indicate that density is increasing with height along the feature. These curves appear to oppose a vertically gravitationally stratified atmosphere, where we would expect decreasing density. However, this is more likely a signature of damping attenuating the propagating waves along the wave-guide. Kink-wave damping has been previously observed in spicules by magneto-seismological profiles in (Morton, 2014) and a more recent example can be seen in (Morton & Mooroogen, 2016). If the waves are being damped, then the observed displacement amplitude measurement are smaller than otherwise would be measured, leading to the apparent increase in the density profiles and a decrease in the flux-tube radius. In this scenario, the density of the fibrils and external atmosphere would be more stratified than the seismology profiles of Fig. 4.17 would seem to indicate. Figure 4.6 of Section 4.2.3 shows what appears to evidence of damping in the H-α IN fibril time-series data, following the peaks at the 50 s mark we can see a decrease in the amplitude as the wave propagates along the feature. In Fig. 4.13 of Section 4.5 we observed a decrease in PSD power as a function of height along a fibrils, a result that would coincide with the behaviour of the profiles here. This possible evidence of damping is also evident in 'downward' propagating waves (right panel Fig. 4.17); most notably in the yellow and purple profiles, where perhaps significant damping has artificially enhanced the perceived density.

The cyan coloured profile, noticeable in the 'upward' propagating plots (left Fig. 4.17) and the gold profile in the 'downward' plots (right Fig. 4.17), both show what appears to be evidence for highly stratified fibrils. These profiles exceed from the model line in the opposite direction to that of perceived damped waves signifying that they may have undergone additional amplification than expected with the model scale-height. It is unclear what could cause such amplification. However (Morton, 2014) presented evidence for rapid amplification of propagating kink waves along a spicule, and showed the necessary density profiles required to achieve them involving a combination of internal and ambient densities. Though, it should remain evident that all changes in amplitude are relative to the initial amplitude measurement per profile.

The variation in the profiles make it difficult to determine the density gradients along the wave-guides. Possibly a more comprehensive inversion method is required to exploit the wave parameters for magneto-seismology, perhaps a more developed model with additional information about the plasma or some form of Bayesian analysis. However, for now we have provided measurements of the profiles variations by fitting an exponential following the model of Equation 4.13. From this fit we aim to determine the density scale-height, though we acknowledge that this measured value will include the influence of internal and external variations in density and the possible effects of the above discussed

TABLE 4.3: H-α Measured fibril properties

Index	ξ (km)	P (s)	v (km/s)	C_k (km/s)	Scale height	av no.	Plot legend
1	33±1	130±1	2.59±0.08	961±307	-842±1014	10	blue
2	28±1	107±2	2.57±0.16	405±252	593±933	8	green
3	23±2	118±3	1.30±0.11	51±11	-	5	-
4	86±2	109±1	8.70±0.23	89±12	-	6	-
5	53±1	67 ±1	7.67±0.21	960±353	-2232±9903	8	brown
6	54±2	80 ±1	7.01±0.29	622±275	-276±251	5	pink
7	86±1	134±1	6.82±0.12	788±236	-	9	-
8	82±1	103±1	8.83±0.12	303±61	-4613±23738	5	orange
9	118±1	123±1	11.08±0.12	939±111	-	9	-
10	118±1	123±1	11.08±0.12	400±41	475±173	9	gold
11	102±2	273±4	3.94±0.09	161±19	692±722	9	red
12	171±3	180±1	10.90±0.22	-489±218	172±62	5	orange
13	169±3	144±2	13.06±0.31	100±17	-	5	-
14	82±3	90±1	5.24±0.21	-732±197	-2103±10772	6	blue
15	74±1	114±1	7.34±0.09	-677±35	601±176	11	gold
16	186±3	162±2	13.30±0.26	749±141	-	7	-
17	60±1	106±1	6.36±0.13	-845±382	-380±271	5	green
18	51±2	81 ±1	7.15±0.21	325±41	-	10	-
19	62±1	88 ±1	8.40±0.22	249±29	-	9	-
20	69±2	192±5	3.81±0.16	78±15	-	5	-
21	79±1	108±1	6.62±0.09	1077±178	552±98	14	purple
22	100±1	153±1	7.12±0.07	-701±46	-3688±2906	15	brown
23	78±2	157±2	5.52±0.17	55±8	-	6	-
24	153±2	180±1	9.38±0.11	127±21	-	9	-
25	31±2	95 ±1	2.99±0.16	-139±35	128±102	5	red
26	94±1	144±1	7.42±0.13	-214±38	-235±134	6	pink
27	71±2	105±1	7.65±0.18	-171±20	70±9	7	purple
28	75±1	122±1	6.49±0.14	85±5	69±7	8	cyan

Uncertainties on displacement and periods have been rounded to nearest integer value, or rounded up to 1 if less than 0.5. Table recreated from (Mooroogen et al., 2017).

damping or amplification. The results of these measurements can be found in Table 4.3 where it can been seen that not all of the twenty eight fibrils measured were used to determine the scale-heights. This was due extreme variability and large error-bars making model fitting difficult and even more difficult to interpret. As such, the IN fibrils indicated by the dashed lines in table are not included in the magneto-seismology plots for visual clarity. The table also lists the colour-code that can be used to cross reference the measured values to the magneto-seismology profiles.

4.6.4 Discussion

In this chapter we have explored and measured the basic properties of IN fibrils in the H-α chromosphere, with the aim of laying the groundwork for understanding their

formation and transport of energy. In the intensity time-series we have observed fibrils to appear, disappear and reappear over time scales of 5-10 minutes indicating regular but not sustained deposition of energy. This cycle of visibility is currently unclear, however it may be result of a thermal non-equilibrium state where the IN fibrils continuously experience stages of heating and cooling. Studies of coronal loop behaviour have used similar explanations (Klimchuk et al., 2010). As an example scenario, one can imagine an initial deposit of energy along a magnetic field that heats the local plasma, this may lead to H-α visibility via postponed Saha-Boltzmann extinction (Rutten, 2016, 2017). This heating could cause the up-flow of denser material from lower regions of the atmosphere, leading onto further enhancement of H-α extinction (Leenaarts et al., 2012). If the fibril then cools and condenses, the plasma would leave the magnetic flux tube reducing the density. Both of these effects would cause the H-α opacity to drop and the fibril would disappear, another heating event could cause this cycle to repeat.

A heating mechanism like this may require a prevailing magnetic flux-tube that is, on the necessary time periods, continuously present and supports plasma that is denser than the ambient atmosphere. However, this may not be always the case in a partially ionised chromosphere based on theoretical reasoning, (Martínez-Sykora et al., 2016). Though, our observations of dense flowing material along an IN fibril would suggest the existence of a magnetic guide for the plasma. Relevant to this topic is the discussion on fibril alignment from chapter 1 subsection 1.5.2, where agreement for alignment was seen by (Asensio Ramos et al., 2017) and also, with earlier measurements of (Schad et al., 2013).

Furthermore, the observed presence of kink waves supported by the fibrils requires an over-dense flux-tube, with a magnetic field perpendicular to displacement vector. The fact that fibrils are observed in H-α may suggest that the features are denser than the surrounding plasma and existence of propagating kink waves along the fibril axis further supports the notion that the features trace the magnetic field. An extension to the discussion of fibril misalignment is continued in (Mooroogen et al., 2017).

We have observed the transverse displacement of the fibril axis in time-series that we interpret as the kink wave. The measured parameters, displacement amplitude and period, reveal that the behavioural properties are similar to previous fibril properties measured as shown by comparing results in Table 4.2 with Table 1.1. In regards to the phase speed measurements, we find no variation in phase speed as a function of distance along the IN fibril. From the phase speed values we are able to obtain a rudimentary estimate of the local Alfvén speed, and therefore the magnetic field strength of the fibrils in the upper chromosphere. Using the equation for kink speed (propagation speed) that links the plasma quantities and the Alfvén speed given as

$$c_k^2 = \frac{2B^2}{\mu_0(\rho_i + \rho_e)} = v_A^2\Big(\frac{2}{1+\zeta}\Big), \tag{4.14}$$

where μ_0 is the magnetic permeability of free space, $\zeta = \rho_e/\rho_i$ and the subscripts (i, e) refer to the internal and external plasma quantities, we can make an estimate for the magnetic field strength. We make the assumption that $B_i \approx B_e$, and estimate chromospheric densities as 10^{-9} - 10^{-10} $kg\ m^{-3}$ along the fibrils from simulations of Leenaarts et al., 2012. These values result in magnetic field strengths in the range 3-200 G, using the larger values for the phase speed (500 km/s) would lead to strengths of 25-200 G. While maintaining that this is a crude estimate, the lower ranged values would seem reasonable, however it is unclear if the larger values would exist in the IN chromosphere. In particular, the LOS magnetic field strengths shown in Fig. 1.10 do not show strengths resembling the upper magnitude in or around the foot-points of the fibril. However, it should be noted that the magnetograms have had no stray light corrections applied which could lead to underestimation of the field strength by up to a half. This would affect isolated magnetic elements via the stray light contributing to the Stokes V profiles of surrounding non vertically-magnetised regions Narayan, 2011, e.g. ME inversions. Although, these larger magnetic field values are far greater than those estimated for spicules that are typically associated with stronger network magnetic regions Centeno et al., 2010, e.g. $\sim$ 50 G. A more recent study (Asensio Ramos et al., 2017) estimates median values of $\sim$ 60 G in plage regions (where fields should be greater than IN) in observations of Ca II 8542Å.

The large values of propagation speeds presented here do however have larger error bars associated with them, which would account for some of the spread in the distribution of speeds. Standing modes existing in the IN fibrils from counter propagating waves may present another explanation, this would lead to spurious measurements of the phase speed. (Okamoto & De Pontieu, 2011) also presented large phase speed measurements for spicules that, akin to these, require an explanation.

By exploiting the measured fibril parameters (displacement amplitude, phase speed) we have been able to infer the physical parameters of the local plasma using magneto-seismology. The results showed evidence for variation in the displacement amplitude as a function of height. Furthermore, the displayed profiles of Fig. 4.17 showed both amplification and damping of the propagating waves. The amplification is not at odds with theoretical model of vertical density stratification of the plasma, when considering the variation of internal and external plasma. Measurements of the density profiles are an average of the internal and ambient plasma density, therefore variations in the ambient plasma density will contribute to the measured profile gradients, (Morton, 2014). Observations and simulations have shown fibrils to rise up out of the neighbouring 'bulk

chromosphere' and breach somewhat into the corona. 3D simulations (Leenaarts et al., 2012) found fibrils to exist up to heights considered coronal. Thus, it is likely that there would be large variations in the external density during this transition from the chromosphere to the corona. This would cause signatures of the ambient density variations to be more pronounced, masking the effect of the internal density stratification. However, it is not clear how one could de-couple the combination of density effects from the observed profiles without some additional information.

In summary, while some deviation is apparent from the theoretical model, some of the magneto-seismological profiles of Fig. 4.17 do correlate with scale-heights of a vertically gravitational stratified atmosphere. Those that display amplification away from the local average suggest support for the notion of external plasma dominating the behaviour. It is expected that kink waves will experience some level of damping during propagation, and due to the total dependency on amplitude, found in this study, the inversion profiles reflect this. Interpretation of the magneto-seismological results must be approached with caution due to the theoretical assumptions (see above) that underlie it.

We have provided the first measurements of IN fibril properties however we recognise the caveats of our investigation. The use of linear-guide cross-cuts to obtain time-series measurements have meant we have obtained a incomplete picture of the full propagation across individual fibrils. This in turn will impact the magneto-seismology profiles where foot to foot measurements may have been enlightening. With a new curvilinear guide, as used in the Ca II research, such a measurement could take place and so revisiting the dataset may be worthwhile. Further, the use of some sort of binary tracking technique as used by (Gafeira et al., 2017b) would enable a larger statistical survey. However, even with a larger sample of IN fibrils any issues with poor signal-to-noise will prevent measurement. In the course of the study, a large canvassing campaign was carried out across the dataset, as such a binary mask method may not reveal new opportunities. Although, its implementation would relieve the laborious task of candidate selection and enable regressive testing.

As previously discussed the method of determining the phase speed is likely to introduce bias due to the subjective measurement locations specified by the user. Finally, it is possible that we are underestimating the uncertainties on intensity from our multi-scale method, though they appear in-line with expected levels of Fabry-Pérot instruments the results from the KS1 test suggests that either our test model is inadequate or that the uncertainty measurement that underpins the least-squares fitting is underestimated. On this point, we have observed evidence for multi-periodicity in our PSD plots, this would lend support to assumed model being incomplete. Therefore, further investigation here is needed to determine a more appropriate model.

5

Observational evidence of kink waves in super-penumbral fibrils

In this second study, we present observations of Ca II 8542 Å that reveal, for the first time, kink waves supported by chromospheric fibrils in the super-penumbra of a sunspot. The discovery of these kink waves may have important implications for the propagation of Alfvènic waves into coronal active regions, where kink waves have been readily observed (e.g., Aschwanden & Schrijver, 2011, Morton & McLaughlin, 2014, Tomczyk et al., 2007).

We present findings that these kink waves may be the result of mode-conversion of upwardly propagating, 'low-frequency' magnetoacoustic waves. Recalling the discussion in Chapter 1 Section 1.4.3, these waves propagate into the atmosphere in the presence of inclined magnetic fields via the ramp effect. From our knowledge of sunspot magnetic topology, we understand that field inclination is ordered near vertically in the umbra and gradually more inclined towards the penumbra. We establish the existence of low-frequency waves in the super-penumbra and infer this as a result of the inclined magnetic field, lending credence to the theoretical picture.

Further to the discovery of kink waves in the super-penumbra, we measure their properties, displacement amplitude and period using the automated NUWT code. Moreover, we determine the distributions of the properties to provide a record for comparison to fibrils in the other atmospheric regions with differing field strengths. Estimates of the propagation speed are made using the cross-correlation method, as described previously, and we relate the displacement amplitudes with radial distance from the sunspot umbra.

5.1 Evidence for the ramp effect

5.1.1 Magnetoacoustic oscillations

In Chapter 1 we presented the FOV of the Ca II dataset, Figure 1.13. We displayed a four panel figure of the Ca II profile minimum, intensity -0.942 Å from line core, the LOS Doppler velocity and line width diagnostics. Here in Figure 5.1, we present a close up view of the super-penumbral fibrils. Over-plotted is a cross-cut guideline to a super-penumbral fibril extending from the umbra outwards. In the lower panels the co-spatial FOV is shown with the guide position over-plotted in both Doppler velocity and line width, only the upper third of the sunspot is shown. In the Doppler image, the colour scale shows blue motion towards the viewer and red away. Motion appears to be towards from the umbra and away from the viewer in the penumbra, possibly as a result of a flow. However, red coloured regions in the centre of the umbra would also suggest some down flow. In the line width image, enhancements can be seen along the super-penumbral fibrils indicated by the red regions. It is unclear what broadening mechanism is dominant here, it is possible that the relative enhancement is due to shock heating (shocks are observed at the base of the fibrils, Fig. 5.2). However, the umbra should be cooler in respect to the ambient plasma and therefore the width enhancement could be non-thermal in origin either Doppler, collisional or possibly magnetic. As discussed in Chapter 3, the Ca II is susceptible to non-thermal broadening.

The three main panels of Fig. 5.2 show the resultant time-distance diagrams from the cross-cut applied in Fig. 5.1, each showing a different diagnostic as labelled. In the top panel the transverse displacement about the central axis of the fibril can be seen, this is perhaps clearest in the 19-30 minute interval. Although the wave appears to broken into segments, the cadence of the data set is, as mentioned in Chapter 3 Section 3.2, 30 s and it is likely that we are missing dynamics of the wave. The subsequent panels show the co-spatial time-distance diagrams for the data products. The Doppler velocity (middle panel) shows no direct correlation with the fibril axis shown in the profile minimum. However, red-blue in phase periodicities can be seen throughout, indicating a LOS velocity component that is probably associated with the running penumbral waves. The line width image does appear to show correlation with signatures of the fibril axis of the profile minimum. The central red region that shows width enhancement relative to the ambient medium is approximately aligned with the fibril central axis. However, this feature seems to expand in time at approximately 26 minutes. It is possible that this indicates some level of heating along the fibril that diffuses over time. However, this depends on the dominant broadening mechanism at work, as discussed above.

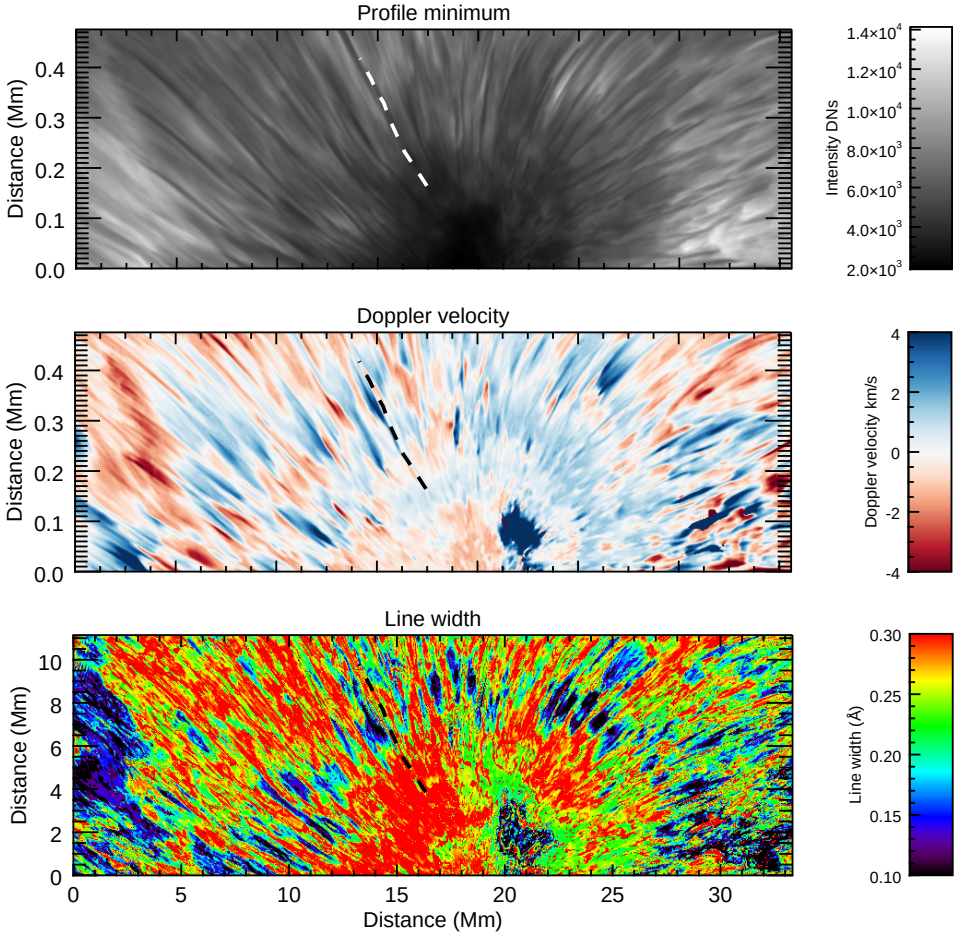

FIGURE 5.1: **Ca II fibril selection in co-spatial data diagnostics.** Co-spatial FOV subsets showing top 8 Mm of the sunspot in profile minimum, Doppler velocity and line width. Over-plotted on each panel is the curvilinear guideline placed along a super-penumbral fibril and used to create time-distance diagrams. The LOS velocity is clipped at $\pm$ 4 km/s and the line width $0.1 > w < 0.3$.

At the base of this fibril, where the super-penumbra meets the umbra we observe shocks (but also seen in multiple fibrils), this is indicative of compressible waves propagating into the atmosphere and shocking as density falls off, causing amplification of the wave (Parker, 1964). The tell tale signs of shocking are seen by the classic sawtooth pattern, this can be seen in the spectral image (right most panel) of Figure 5.2. Previous observations have found shocks at the base of the fibrils and have linked the shocks to the fibril formation (Chae et al., 2014).

Magnetoacoustic waves in the form of running penumbral waves can be seen throughout the time-series. In Fig. 5.3 we display a cross-cut taken horizontally through the sunspot to visualise these oscillations. In the resultant time-distance plots, Fig. 5.4, we see the profile minimum, LOS Doppler velocity and line width diagnostics, aligned co-spatially from top to bottom respectively. Alternating red-blue bands can be seen through centre of the Doppler image, and this is correlated in the line width data. However, the line

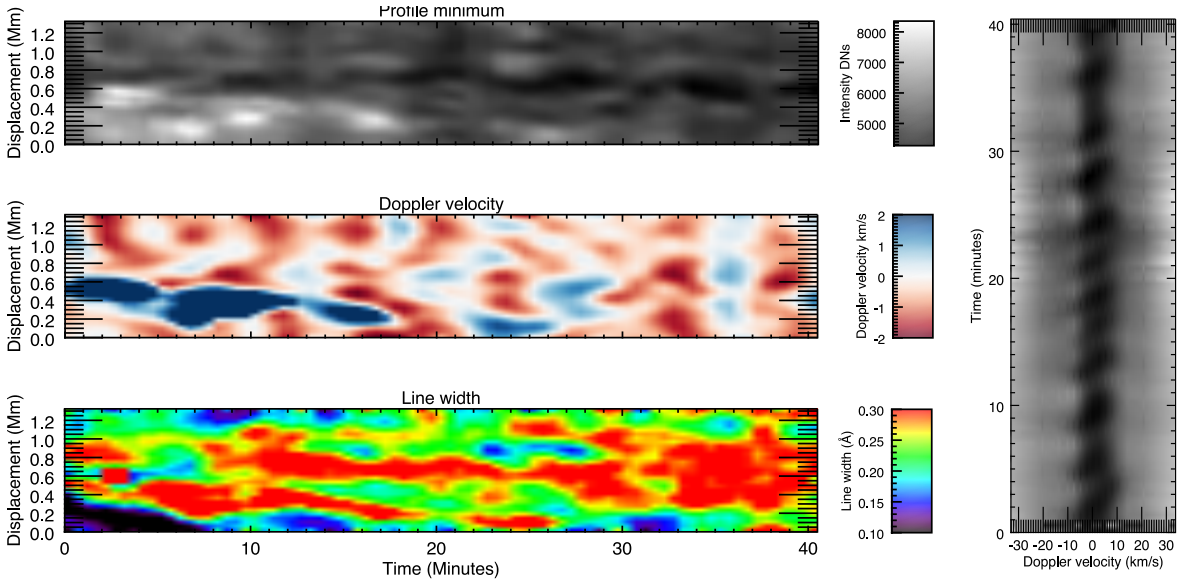

FIGURE 5.2: **Co-spatial time-distance diagrams.** Spatial-temporal diagrams displaying the co-spatial relations between the measured data products can be seen in the three panels. Evidence of transverse displacement can be seen in the profile minimum, though this signature is not reflected in the Doppler velocity. The line width data appears to show some semblance of the fibril central axis, this can be seen as the red region through the centre of the image. The velocity data is clipped between $\pm$ 2 km/s for visual clarity, and the line width data at $0.1 < w < 0.3$. To the right of the three (x, t) panels, a (v, t) image can be seen of the Ca II spectra. A sawtooth pattern can be seen throughout the spectra which is indicative of shocks.

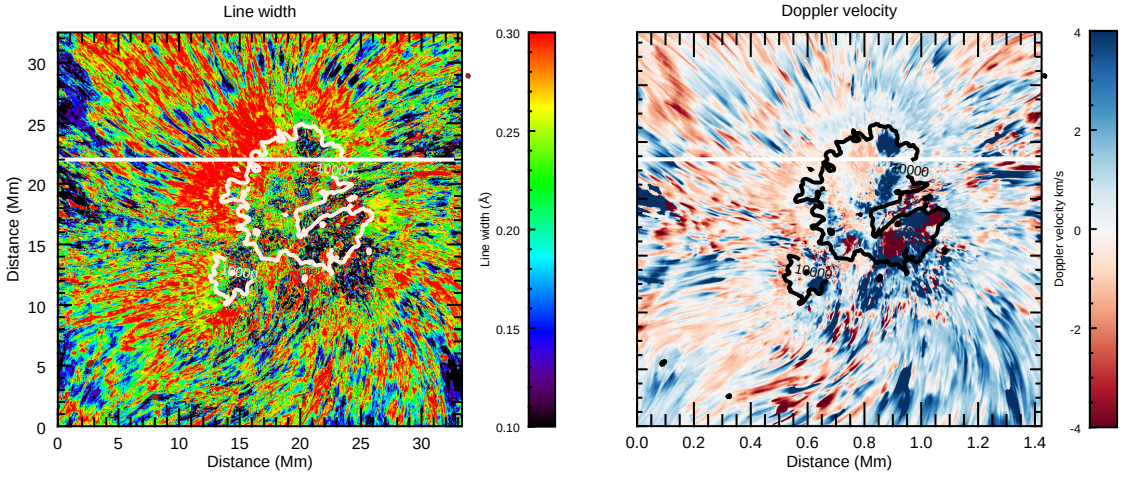

FIGURE 5.3: **Trans-sunspot cross-cut of line width and Doppler velocity.** Full FOV images of the line width and Doppler velocity (*left* and *right* respectively). Overplotted in white is the trans-sunspot cross-cut used to investigate the magnetoacoustic signatures, contours of the umbra are shown in white and black.

width periodicity is less so at 10-15 Mm, where the width is enhanced. This gap appears to correlate with a decrease in amplitude in the LOS Doppler velocity and possibly indicative of shock heating. As we have seen, the umbral regions show both shocks and width enhancement. We suggest a scenario in which the line width is sensitive to velocity

perturbations in the 17-20 Mm region, and is thermally broadened in the presence of a heating event i.e. shock (10-15 Mm). However, this interpretation is subject to the assumption that the measured widths represent the broadening in the core, and not contaminated from the photosphere as discussed in Chapter 3 Section 3.4.

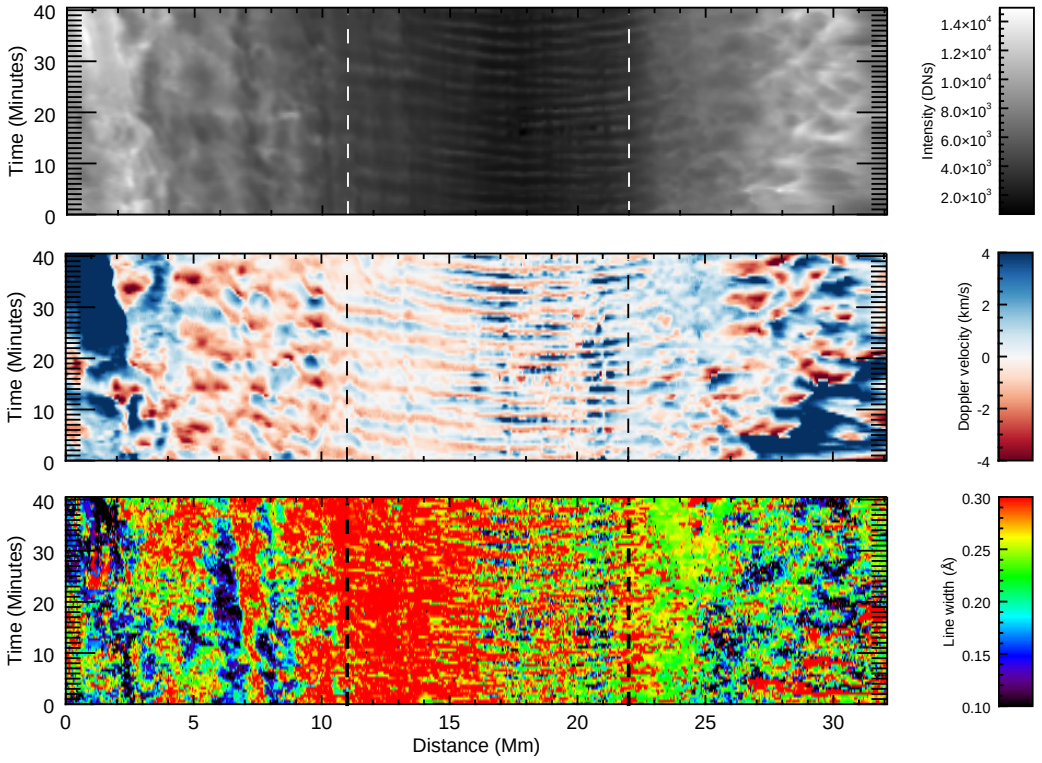

FIGURE 5.4: **Co-spatial time-distance diagrams of magnetoacoustic oscillations.** Trans-sunspot time-distance diagram (from the cross-cut shown in Fig. 5.3) of the profile minimum, Doppler velocity and line width (from top to bottom respectively) showing evidence of magnetoacoustic oscillations. This can be identified by the alternating ridged pattern most evident near and through the umbra (area between vertical dotted lines).

This central area corresponds to the umbra (indicated by vertical dotted lines) and it is clear from the images that there is a prominent LOS velocity component in this region, estimates place these oscillations peaking at around 5 mHz. This was determined by taking four 1D data slices at between 10-15 Mm and passing the resulting oscillatory signals into a Fourier transform, Fig. 5.5. In the left panel we display the four LOS velocity time-series over-plotted, these signals appear mostly in phase however at varying values of velocity. In the right panel the average PSD, resultant of the four time-series is plotted, a clear peak can be seen at approximately 5 mHz. From this frequency value we attribute the signals to the upward propagating magnetoacoustic waves. The oscillatory signatures gradually fall off towards the edges of the umbra and are not as readily visible in the penumbral regions. This is an indication of the vertical magnetic field orientation

in the umbra, directing magnetoacoustic waves (at or above the the cut-off frequency) into the LOS. Thus, in the penumbral regions, where the field is more inclined, the velocity component of the magnetoacoustic waves is *out* of the LOS and so periodicities are weaker there. This would correlate with the theoretical picture of the sunspot magnetic topology and wave propagation discussed in Chapter 1 subsection 1.4.3.

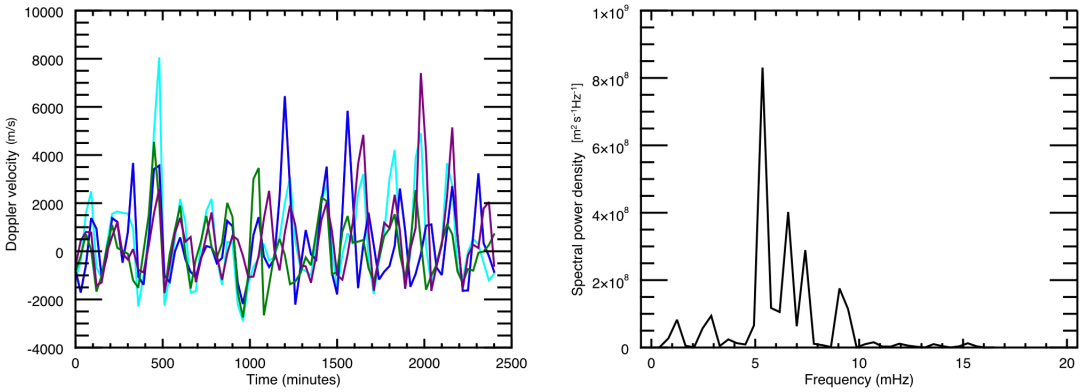

FIGURE 5.5: **1D Doppler signal and Fourier Transform.** Time-series data of four 1D slices through the umbral region shown in Fig. 5.4 (*left*). Peak oscillations can be seen at 5 mHz in the subsequent average PSD of the signals (*right*).

Figure 5.6 reveals co-spatial time-series (taken at 17 Mm, Fig. 5.4) of the Doppler velocity (solid line) and line width (dashed line). The LOS Doppler data has been normalised and reduced by a factor ten to allow plotting on the same scale. From visual inspection the signals appear to be in phase at some locations, though from these plots alone it is hard to draw any clear correlations. The use of cross-spectral analysis to examine the phase and coherence would be valuable in this instance. However, due to the sub-optimal conditions of the line width data-set and its possible photospheric contaminations we have refrained from performing that analysis here.

5.1.2 Magnetic field inclination and magnetoacoustic power

In Chapter 1 we have laid the theoretical groundwork to discuss the relationship between magnetoacoustic wave propagation and magnetic field inclination. We established that due to the increasing inclination of magnetic field, leading to a reduction in the cut-off frequency, one should expect peak low-frequency magnetoacoustic power in the penumbra. With the aid of 2D Fourier analysis, we have demonstrated this effect by displaying the distribution of frequency at peak power of the magnetoacoustic waves in and around the sunspot. However, we note our assumption that the power evident in the images is resultant of magnetoacoustic modes mainly from the prevalence of running penumbral waves, this agrees with the picture seen in (Jess et al., 2013).

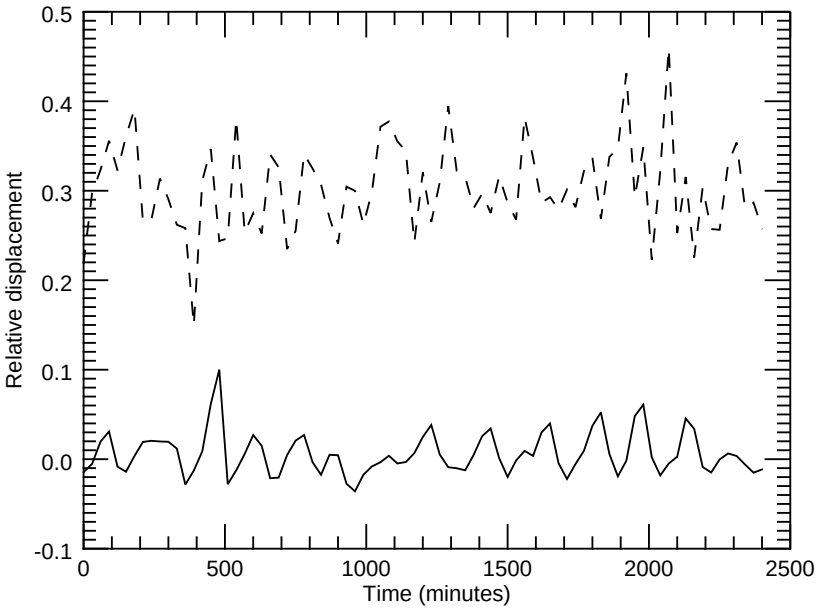

FIGURE 5.6: **Doppler signal and Spectral width time-series.** Time series data of the LOS Doppler velocity (solid line) and spectral widths (dashed line) taken at 12 Mm in Fig. 5.4. The Doppler time-series has been normalised and reduced by a factor ten for scaling.

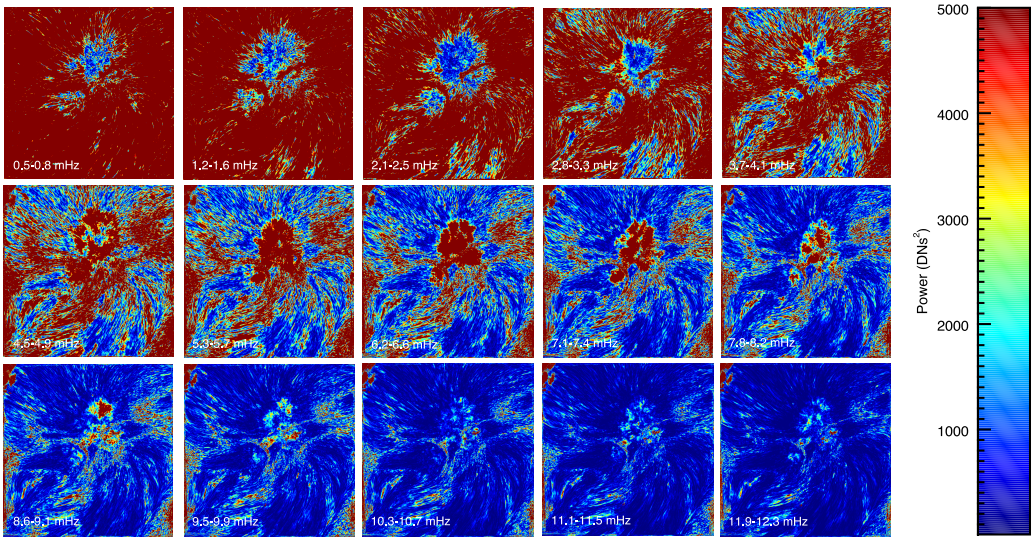

FIGURE 5.7: **2D FFT of Ca II sunspot.** Fourier transform plot of the sunspot intensity dataset, each plot (from left to right) shows the power at a given average frequency, frequency increases with each successive plot. It can be seen that with increasing frequency power moves from the super-penumbra into the umbra.

Utilising standard Fourier practises, as established in Chapter 4 Section 4.4, we produce 2D power maps of the Ca II profile minimum data at increasing frequency scales. Figure 5.7 shows these power maps at increasing frequency from left to right. The displayed power in each image is averaged over two frequencies bins up to approximately 12 mHz. The total sequence of the power map images creates a three dimensional array of (x, y, ν)

where ν is frequency. With this array in hand, we determine the frequency value where the power is maximum on a pixel-by-pixel basis across the FOV. It is then possible to create a 2D image showing the frequency distribution of the sunspot at maximum power. We extend this method to include transforms of the velocity and line width datasets, Fig. 5.8. This allows us to establish relationship between the radius of the sunspot and the frequency range of the diagnostics of the magnetoacoustic waves.

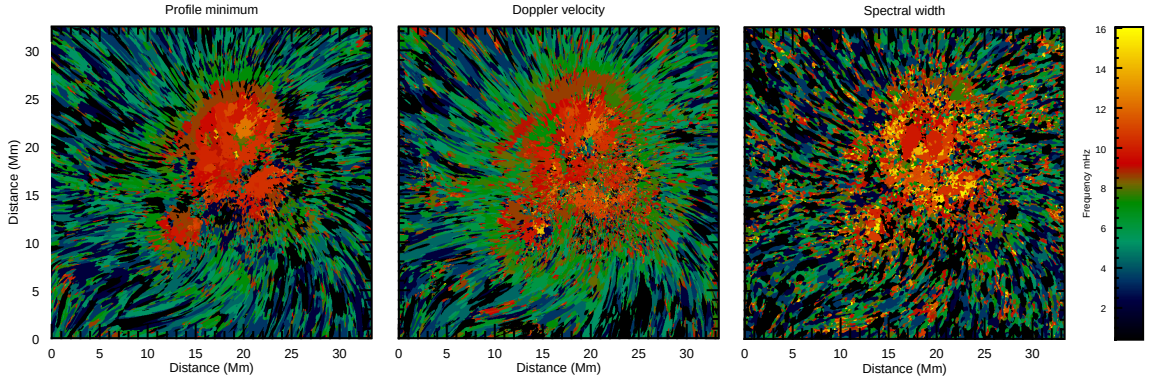

FIGURE 5.8: **Maximum power frequency of Ca II sunspot.** Each pixel represents frequency at which that location exhibited maximum power in the Fourier transform for each diagnostic. From left to right, profile minimum, Doppler velocity and line width of the Ca II sunspot. The colour bar shows the frequency level in mHz.

In figure 5.8 the resultant, maximum power frequency plot for the profile minimum, Doppler velocity and line width is respectively presented. In the umbral sections of each diagnostic, higher-frequency magnetoacoustic power (orange-yellow) can be seen, with the strongest signature visible in the profile minimum. This high-frequency power rapidly falls off into penumbra where a wealth of low-frequency power (blue-green) dominates the rest of the FOV.

The line width data is expectantly noisier than the other data products likely due to the difficulties in determining the width from a spatially/temporally varying profile, as discussed in Chapter 3 Section 3.4. As such, a low-pass (Gaussian) filter has been employed to reduce the (spatial) high-frequencies. Further examples of the relationship between magnetoacoustic power and field inclination can be seen in Figure 5.7; here, the power at increasing frequencies is shown from left to right in each sub-image. Greater power can be seen in the penumbra at lower frequencies and in each consecutive image (moving to higher frequencies) the power increases in the umbra.

So far we have described the inference of the sunspots field inclination based on assumed knowledge of its topology. However, we now attempt to approximate this inclination via magneto-seismological inversion using Equation 1.19 described in Chapter 1. We supply the value of the peak periods using the maximum power frequency map of the profile

minimum, converting necessarily from frequency to period. To determine a model temperature to use in the equation we have employed the Stefan-Boltzmann law assuming LTE,

$$j = \sigma_B \theta_K^4, \tag{5.1}$$

in a similar method as described in (Löhner-Böttcher, 2016), where j is the radiative power, σ_B is the Stefan-Boltzmann constant and θ_K is the temperature. It is possible for a far more accurate temperature map of the FOV to be calculated from inversions of the Stokes parameters, for instance with the NICOLE code (Socas-Navarro, 2015). The Stokes parameters are available for this dataset, however due to computational expense we have opted for the expedient approach. Without a specific value for the radiative power we calculate the temperature map relative to a suitable atmospheric model, invoking Equation 5.1 and using the measured intensity of the data as a proxy for j. The formula for the temperature estimate is then,

$$\theta_K^4 = \frac{j}{j_r} \theta_{K,r}^4, \tag{5.2}$$

where the r subscript refers to a reference value of intensity and temperature determined from a chosen model. The computational process is to calculate this equation for every pixel in the FOV.

To formulate the reference intensity, a single intensity value is chosen from the temporal average FOV, for this we have utilised a pixel in the upper right corner in a quiet sun region (outside of the penumbra). The corresponding reference temperature is obtained by referring to an appropriate quiet sun atmospheric model. In this case, we have first established a formation height (where $\tau = 1$) of the reference intensity by extracting a value from quiet sun 3D simulations of Ca II 8542Å, (de la Cruz Rodríguez et al., 2013). This formation height ($\sim$1330 km), is then used to retrieve a temperature value from the quiet sun model of (Maltby et al., 1986), see Fig. 5.9 for model. This method however relies on the assumption that the formation height model is adequate for the selected quiet sun region, it is unlikely that all regions of the 8542Å quiet sun are formed at the same height. Further, this approach relies on that the two employed models are commutable and that the measured intensities are a suitable proxy for radiative power. However, (Cauzzi et al., 2009) explains that Ca II 8542Å brightness is a good indicator of temperature. Our estimate also exhibits a systematic error imposed by the selection of the reference pixel. Moreover, a simple but important point raised in (Löhner-Böttcher, 2016) is that the dependency on temperature in Equation 1.19 is far smaller than that of

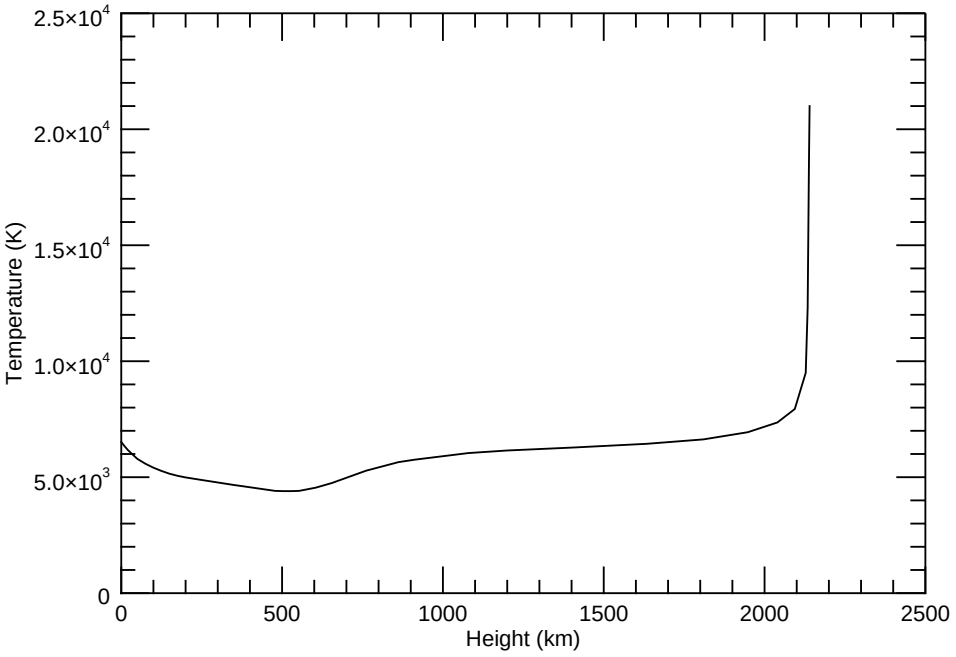

FIGURE 5.9: **Quiet sun Maltby model.** Maltby quiet sun model recreated from (Maltby et al., 1986). The curve is plotted as a function of atmospheric height, the 'solar surface' (Temperature at 5000 Å) is designated by the origin. Recognisable is the familiar temperature profile for a hydrostatic atmosphere, gradual temperature decrease until the minimum in the photosphere that the gradual increase into the chromosphere before the steep rise at transition region heights.

the peak periods, this is due to the square root in the formula. Therefore, approximations of the temperature will not impact greatly on the value of the LOS inclination relative to the peak periods.

Figure 5.10 shows the estimated temperature (left) and LOS inclination (right). The temperature map is expectedly similar to the profile minimum data as it is only mathematically different by a normalised scaling factor. As we can see in the LOS inclination map, the angle to the vertical increases from the umbra to super-penumbra, as indicated by the colour map. However, a large portion of the umbra is unmapped, here, the inner part of Equation 1.19 exceeded the cosine range leaving them undetermined. As such areas of the umbra angle estimation resulted in 'NAN' values, for the sake of plotting they have been set to zero angle. It is unclear the cause of this discrepancy, either the temperature estimation is far removed (too high) or perhaps the umbra regions exhibits enhanced periodicity. This serves as an example of how the variation of atmospheric properties and indeed the dynamics (magnetoacoustic oscillations) can affect the inference of the inclination angle. Utilising an alternative model to describe an umbral pixel as the reference could alleviate this issue (effectively lowering the temperature estimate),

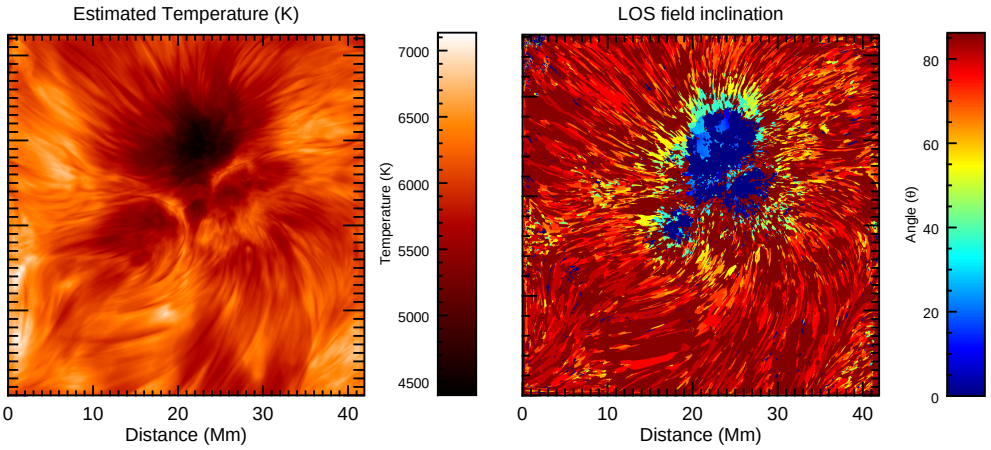

FIGURE 5.10: **Estimates for temperature and LOS field inclination.** Two panel figure depicting the estimated temperature map (left) and LOS magnetic field inclination (right). The inclination image is clipped to the range 45-75 degrees for visual clarity, areas or zero angle indicate the under-mapping of the umbra due to break down of the inversion techniques. However, enough remains to identify the distribution of inclination angles, showing larger inclination to the vertical evident in the super-penumbral regions.

however without a formation height to apply to the Maltby model another method is needed.

(Henriques et al., 2017) utilise the Stoke parameters from the same Ca II dataset to perform non-LTE inversions and obtain temperature information. From these estimates we can obtain a temperature model of the umbra. It is then possible using equation 5.2, with the umbral parameters as the reference, to obtain a full FOV temperature estimate. With this, a field inclination map derived from an umbra model can be produced, Fig 5.11. The umbral model inclination map was again subject to the same issue of exceeding the cosine range. However, to a lesser degree than before as can be seen by the smaller zero angle region in the umbra of Fig 5.11. This result supports the notion that the periodicity in this region is enhanced and inferring the inclination angle from the wave propagation is limited.

Nevertheless, blue areas can be seen dominating the remaining umbra in Fig 5.10 and Fig 5.11, correlating the inclination inversion image with the maximum power map provides further evidence supporting the ramp effect.

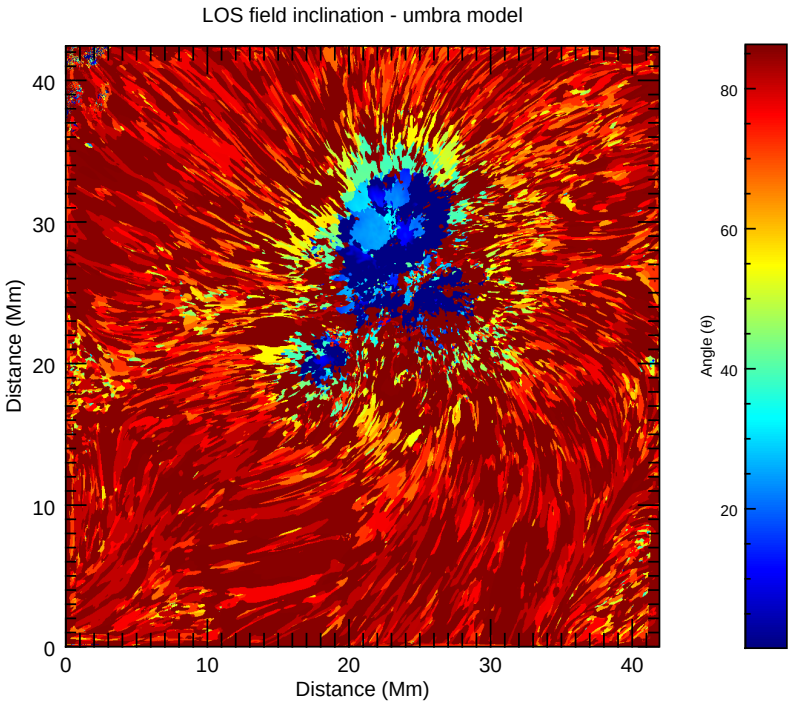

FIGURE 5.11: **Estimates for LOS field inclination using umbra model.** LOS inclination estimate as determined using the umbral reference model. As with Fig 5.10, areas of the umbra remain unmapped and are highlighted with an angle of zero. However, it can be seen that this is less so than the quiet sun Maltby model.

5.2 Kink-waves supported by super-penumbral fibrils

The tracking and measurement of the super-penumbral fibrils differ from that of the IN fibrils in two distinct ways. Firstly, the development of the spline slit code enabled the use of curvilinear guidelines. As the name suggests, this method would fit a cubic spline to manually selected guide-points, then as before perpendicular cross-cuts were calculated and placed accordingly. This method ensures that we are able to follow the distinct shape of individual fibrils, allowing better examination when analysing propagation. Further, we employ the use of radial cross-cuts, these allow the production of time-distance diagrams as a function of radius form the sunspot centre. The second, is the manner of measurement; advances in the NUWT code now facilitate fully automated parameter estimation using FFT. In the following subsections we will discuss the changes in methodology and highlight the nuances that coincide with them.

5.2.1 Time distance diagrams with spline slit and the radial method

Figure 5.12 shows an isolated FOV of fibrils in the Ca II sunspot super-penumbra, the manually selected guide-points to which the spline is fitted can be seen on a selected fibril (white stars, left panel figure). The result of the cubic spline fit provides the curvilinear

guideline, this is shown as the white line passing through the selected points. Cross-cuts normal to this line are then calculated and applied, shown here as white perpendicular lines in the right hand panel. For this example only five guide points have been shown and a large separation distance is chosen between the cuts for visual clarity.

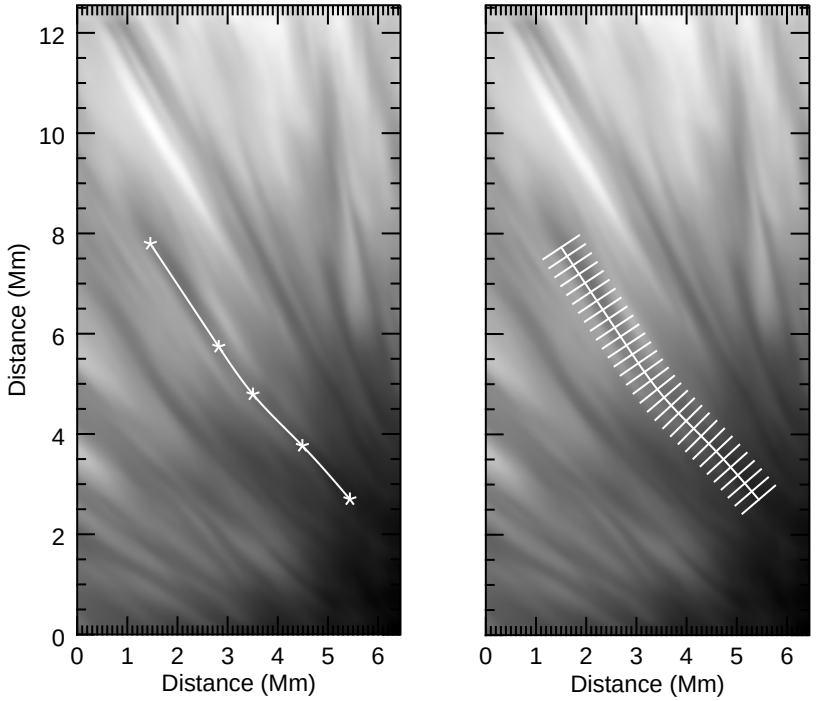

FIGURE 5.12: **Spline slit cross-cuts application.** Left panel figure shows the manually selected guide points (white stars) and the resulting spline fit can be seen overplotted. In the right panel, the cross-cuts normal to the guide-line is shown along the fibril structure. For clarity a small number of guide points and a large separation distance is chosen.

An important caveat of the spline slit code is that the spacing set between the cross-cuts will not be the exact spacing in the resultant vectors. This is due to the spline fitting of the curved feature being calculated to the nearest pixel. To overcome this, the code has an optional feature that over-samples the spline fit. This increases the point density, and by using a linear approximation for the distance between the spline points, cumulatively sums the inter-spline point distance until the desired spacing is reached (Mooroogen et al., 2016). The higher the factor of oversampling the more accurate the linear approximation and therefore spacing estimate will be. On this point, a large oversample rate will increase the running time of this code. Factors of two to three are used for an optimum balance between computational expense and accuracy. An oversampling of two would mean an increase of 10^2 spline points (Mooroogen et al., 2016). An estimate of the resultant spacing can be recovered from the routine, all geometries are known.

The second method for creating time-distance diagrams is dubbed the radial method. Like the previous method, cross-cuts are placed along a feature perpendicular to the central-axis. The difference here however, is that the cuts are in a circular fashion around a common centre. Each successive slit is then at larger and larger radii meaning that each time-distance diagram is of difference size. This method was specifically designed to inspect the Ca II sunspot dataset as the fibrils fan out radially from the umbra. The circular slits ensure that many fibrils are captured, Fig. 5.13, and also help to establish relationships with the measured properties with radii from the umbra.

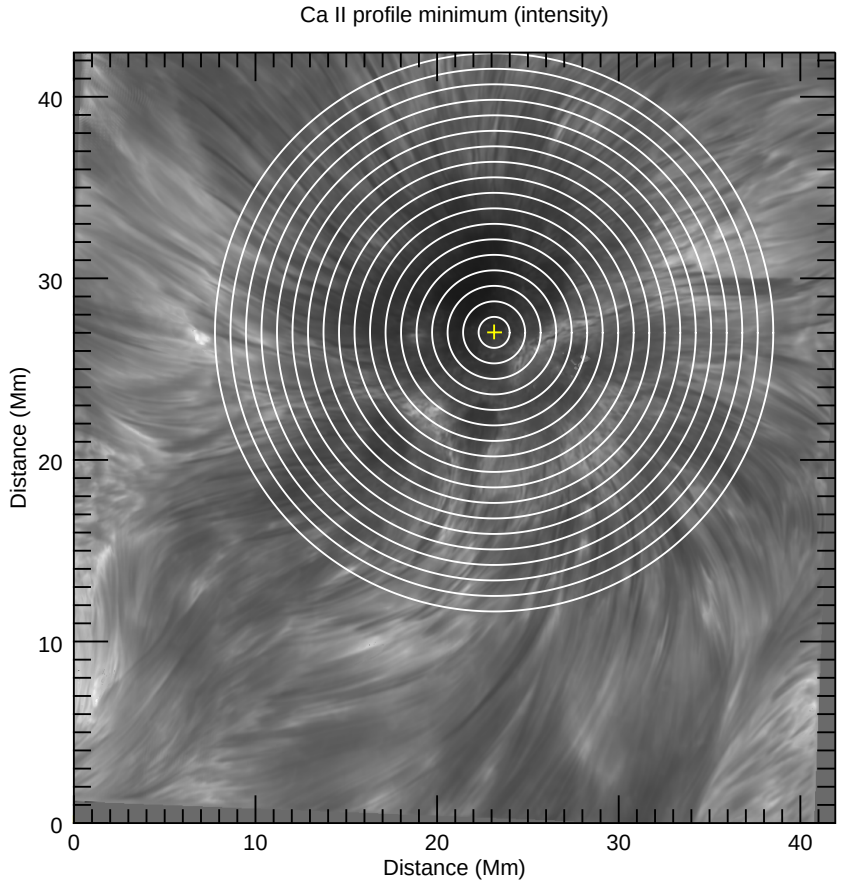

FIGURE 5.13: **Radial cross-cuts application.** Profile minimum image of the Ca II sunspot with circular cross-cuts displayed in white, location of maximum LOS magnetic field marked in yellow.

To create the time-distance diagram in this manner, first the co-ordinates of each point on the desired circle are calculated from the predetermined radii using standard circular formulas. However, whole pixel values cannot be used at these co-ordinates to capture the data at these locations due to the circular nature of the slit. These co-ordinates then serve as pixel locations where the the original dataset is to be interpolated. Since the interpolation is over small distances it is assumed that errors in the data estimates

will be small, moreover the effect of the interpolation will be smaller at points nearer or at whole pixel values.

In order to define the centre point from which the radial cross-cuts are made we have used the point of strongest magnetic field in the sunspot umbra. Figure 1.13 highlighted the irregular shape of the sunspot umbra, if we recall it comprised of three separate umbras of differing sizes, partitioned by a light bridge. This would make taking a barycentre uneven towards the greater core. As such, the decision was made to determine the location of the point of strongest magnetic field. Unlike the H-α dataset, photospheric magnetic field data was unavailable from CRISP, so we employ co-temporal and co-spatial SDO HMI data described in Section 3.

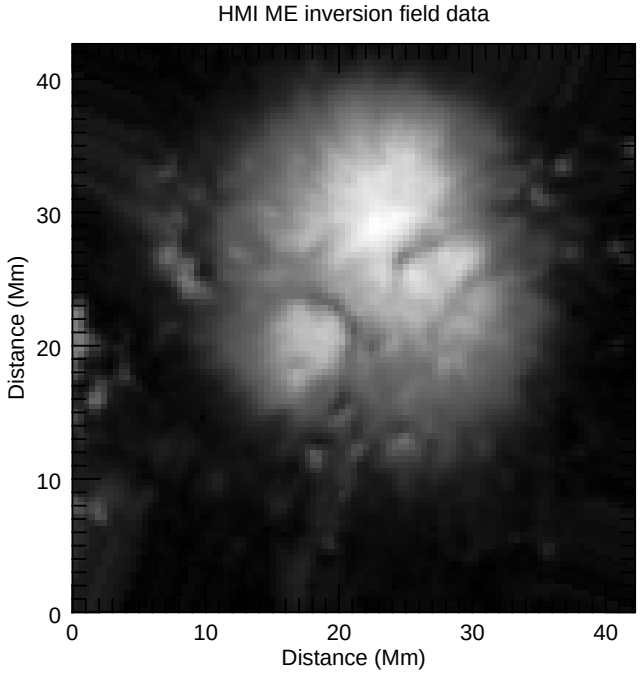

FIGURE 5.14: **HMI line-of-sight magnetic field data.** Line-of-sight of magnetic field data (ME inversions) taken with the Solar Dynamic Observatory Helioseismic and Magnetic Imager.

The line-of-sight magnetic field data from HMI is used to determine the location of maximum magnetic field strength, Fig. 5.14. However, mapping the co-ordinate location from the HMI dataset to the CRISP dataset is non-trivial. The two datasets have different resolutions and orientations, it is here we can employ cross-correlation. Visually, the HMI line-of-sight (LOS) data and the CRISP profile-minimum data are too dissimilar to perform correlation, an intermediate step is needed. First, we need two images from each instrument that are comparable, for this the photospheric wing image of the CRISP data and the white-light photospheric image from HMI is taken, top right Fig. 1.13 and

right panel Fig. 5.15 respectively. The CRISP data is degraded in resolution to match that of the HMI data. In Figure 5.15 the similar photospheric images can be seen, in the left panel the degraded CRISP wing data is depicted and the difference in relative orientations between the datasets is evident.

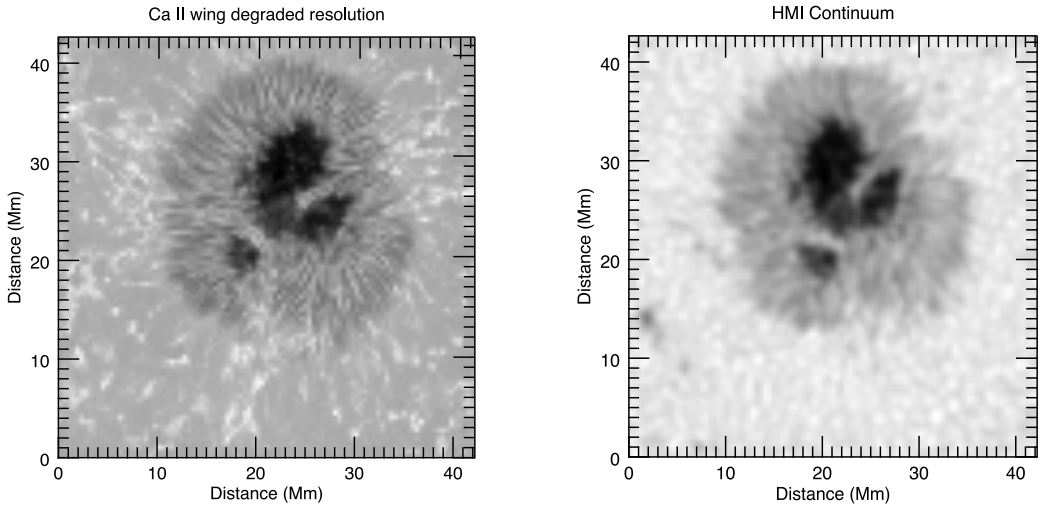

FIGURE 5.15: **Degraded CRISP and HMI white-light sunspot data.** Two panel image showing the CRISP photospheric intensity -0.942 Å from line centre (*left*), the resolution has been degraded to match that of the HMI white-light photospheric data (*right*).

Cross-correlation is performed with these images and the resultant displacement (and rotation) vectors are determined, facilitating the orientation matching of the two datasets. This can be seen from the HMI continuum contours over-plotted on the CRISP degraded image, left panel in Fig. 5.16. In right panel (Fig. 5.16) the corrected orientation of the continuum image can be seen. The location of LOS magnetic field maximum is then determined by applying a 2D Gaussian fit to the LOS magnetic field data. Thus, with the knowledge of the degradation factor, the displacement vectors allow the location of maximum field strength to be translated onto the profile-minimum CRISP data.

5.2.2 NUWT (automated)

The motivation for an automated wave measurement system is clear; and since the incarnation of the original routine, advancements have prevailed in delivering a working automated NUWT code. This version is currently under development by Micah Weberg (Weberg et al., 2016), and has been used in this research to track and measure kink waves found in the Ca II dataset. The automated NUWT code shares the same tracking routine as the semi-automated version, the difference lies in how the wave parameters

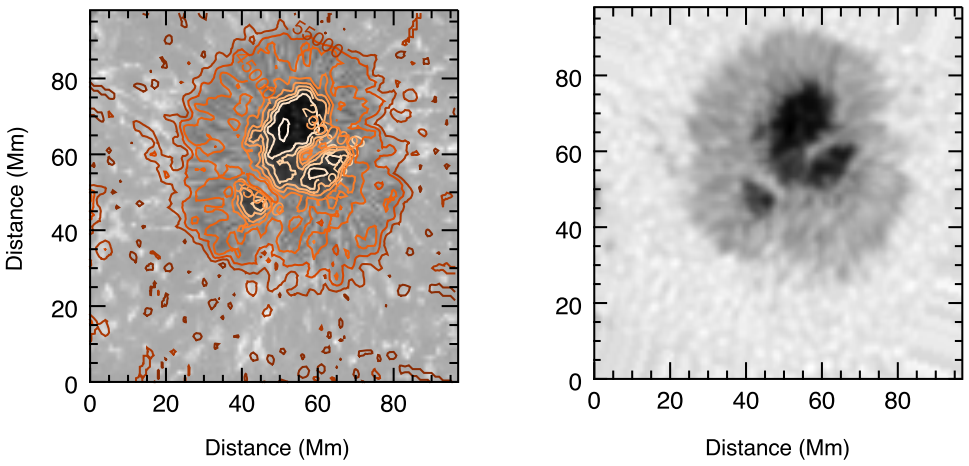

FIGURE 5.16: **Post-correlated degraded CRISP and HMI white-light sunspot data.** Left panel shows the degraded CRISP image with the HMI continuum data contour over-plotted indicating the successful cross-correlation. The right panel shows the white-light HMI image with the orientation corrected to match the CRISP dataset.

are measured. The automated code relies on Fourier analysis instead of manual fitting procedures. Not only does this remove fitting bias but also circumvents the need for specifying the number of sinusoids used in the model; if a thread has multiple wave modes present, they can be recovered from the Fourier transform. This allows for reproducible and fast measurement, and has been used extensively in the Ca II sunspot dataset where we have identified hundreds of features. In the three panel image of Figure 5.17, we see the time-distance diagram from the Ca II dataset largest radial cross-cut. The top panel depicts the intensity from the profile-minimum data, this data has been unsharped masked to aid in detection and only half the curve is shown. In the middle panel, a binary image shows the detected peaks from the NUWT code and the bottom panel shows the joined peaks forming threads.

Waves are identified from the Fourier power spectrum using statistical significance testing (Torrence & Compo, 1998), this essentially sets a threshold value where any power above this value will be considered a signature of a wave, rejecting the null-hypothesis. The null-hypothesis can be described here as the notion that the measured signal cannot be distinguished from white noise. The frequency and amplitude at the bin location that exceeds this threshold is recorded as the parameter measurement of that wave. The code also features the optional use of zero padding for visual clarity of the signals, and windowing (using split cosine-bell function) to reduce spectral leakage.

Figures 5.18 and 5.19 show example outputs from the NUWT automated code. In the top right plot of Figure 5.19, we see the power spectral density plot for a specific thread where the Fourier spectra has failed the significance test and cannot be distinguished

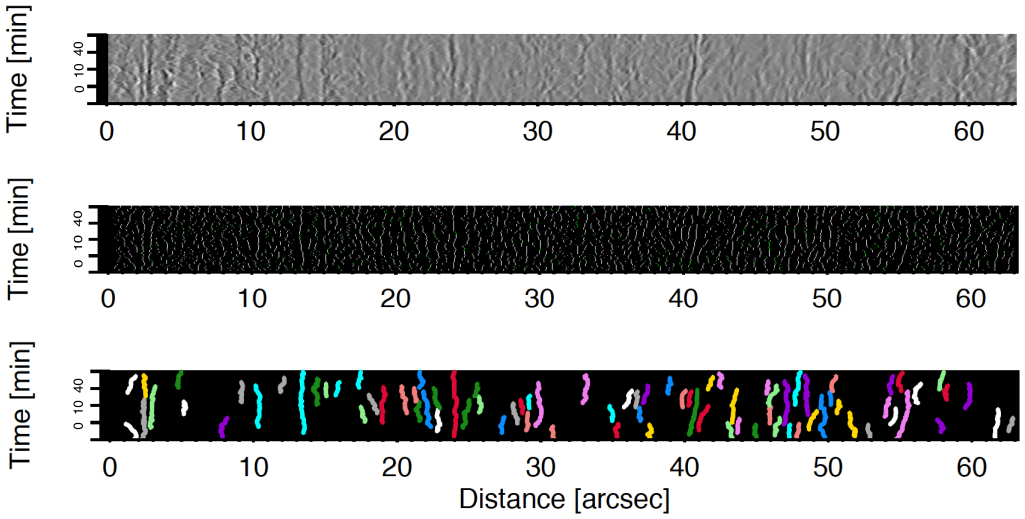

FIGURE 5.17: **Automated NUWT wave-tracking.** Time-distance (x, t) diagram from the outermost radial cross-cut of the sunspot data. The top panel shows an unsharped-masked intensity image. Transverse displacements can be seen throughout. The middle and bottom panels show the tracked intensity peaks (binary image) resultant from the NUWT code and the subsequent joined threads shown as the coloured lines, respectively.

from white noise. This is indicated by power spectra falling below the horizontal dashed line. Consequently no reconstruction of the signal can be seen plotted in the top left plot, the flat black line reveals no significant peak was found. However, in Figure 5.18 a peak has been found, this is revealed by the red diamond on the power spectral density plot, the parameters of that point can be seen in the relevant legend below the plot. In the signal plot on the left, the signal has been reconstructed with the found significant peak and over-plotted on the original signal. This signal has been windowed, this can be seen by the blue crosses marked on the plot and as such the reconstruction is of the windowed signal. The dotted line indicates a basic linear trend. Below this plot the residuals are shown and in the legend the statistics from the test of randomness.

Further advantages of the automated code is the validation and inspection of the resultant transform by testing the residuals. To do this, the residuals between the original signal and the rebuilt signal (rebuilt using the significant peaks) are tested for normality using the Kolmogorov-Smirnov, Anderson-Darling and the Ljung-Box statistical methods. These tests have been discussed in Section 4.3. This gives the user three comparative methods to inspect the resulting transform, other than visual, allowing for further scrutiny of the measurement. However, in the legend of Fig. 5.18, the criteria of normality is also not met. Though, the reconstructed signals represent only the primary wave components, and furthermore they are fitted to the windowed function, not the original signal and a full replica of the signal dynamics is not expected.

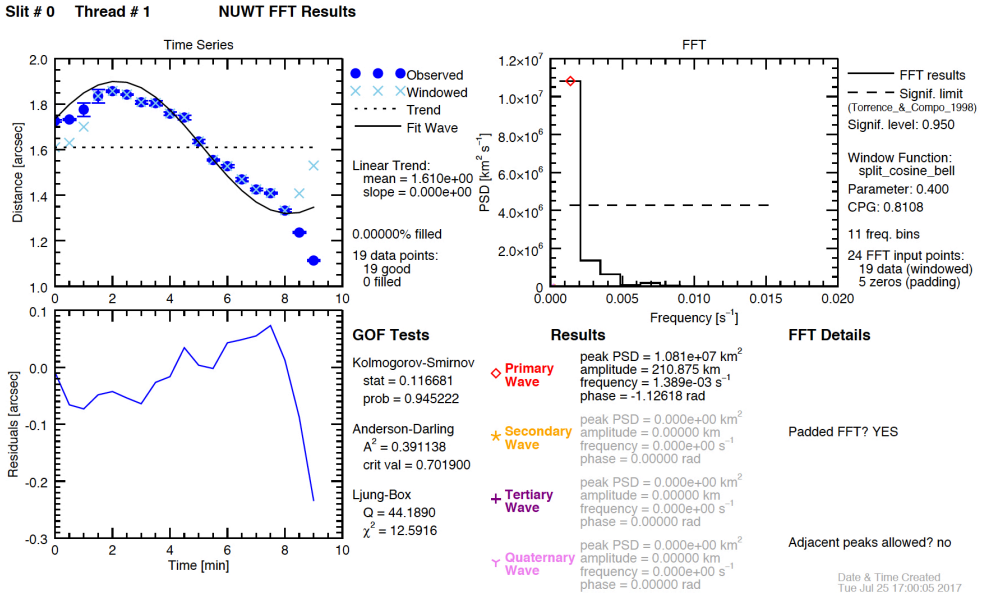

FIGURE 5.18: **Automated NUWT routine output-significant peak.** In the right hand plot the power spectral density plot from the Fourier transform of the signal is shown. The horizontal dashed line indicates the level of statistical significance. The power spectral density has exceeded the necessary significance level to reject the null hypothesis. The significant bin is highlighted by the red diamond and in the legend below the measured parameters are listed. Top left plot shows the detected signal (blue dots) with associated error-bars. Over-plotted crosses (light blue) show the applied split cosine-bell window. The dotted black-line shows the mean value of the data. The over-plotted black line is the reconstructed signal from the significant peaks found in the Fourier transform. The lower left plot displays the residuals between the signal and the reconstructed data.

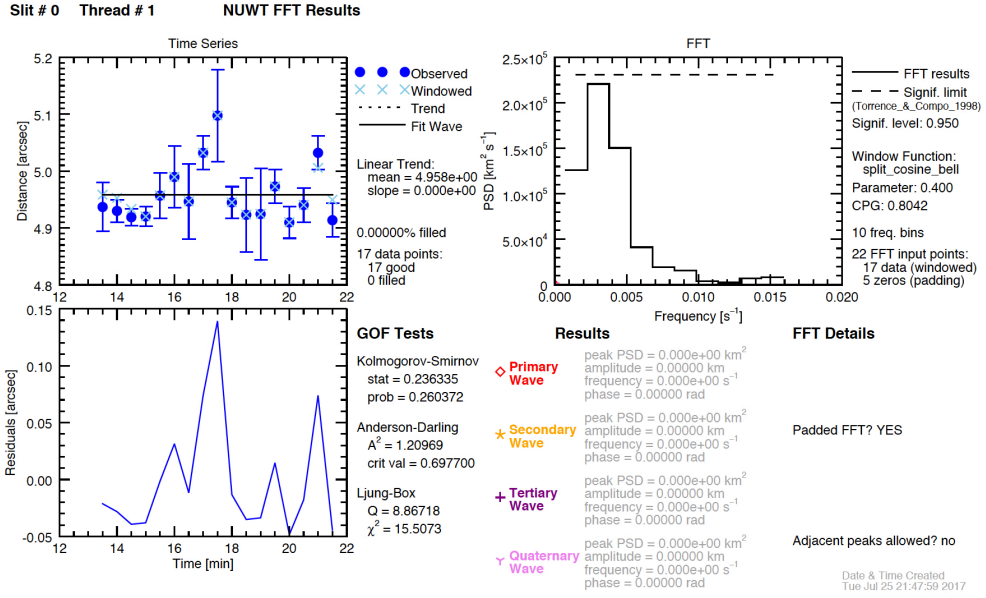

FIGURE 5.19: **Automated NUWT routine output-no peaks.** In this example output of the automated NUWT code, the detected wave has failed the significance test in the power spectrum revealing that the signal cannot be statistically distinguished from white noise. See Fig. 5.18 for details of plotting features.

5.3 Results

A host of fibrils are readily visible surrounding the upper region of the sunspot, as such we concentrate our measurement selection in this area. Using Fig. 5.13 the area in question can be identified as the region contained within a semi-circle starting from the left hand side at approximately 27 Mm on the y-axis. Therefore, the time-distance diagrams from the radial slits are cut to contain data from these semi-circles at each increasing radius. Figure 5.20 shows examples of the radial time-distance diagrams from slits counted as the fifteenth and sixteenth from the centre (at a radius of 13-14.5 Mm). Here, the image areas have been cropped to cover the same distance range so that they could be plotted on the same scale, the data has undergone unsharp-masking to increase contrast to aid in the detection of the fine-scale features. Hundreds of kink waves supported by super-penumbral fibrils are identified using the automated NUWT method, Fig 5.17 and Fig. 5.20 show examples of the tracked waves. Poor temporal-resolution makes it difficult to discern some features and so large detection gradients are used in the NUWT code to delineate features. Small gaps in the time series data are interpolated to form a longer series. In this instance we reduce the available interpolation gap to a single pixel, as the default two pixels would result in a gap of one minute would be extensive.

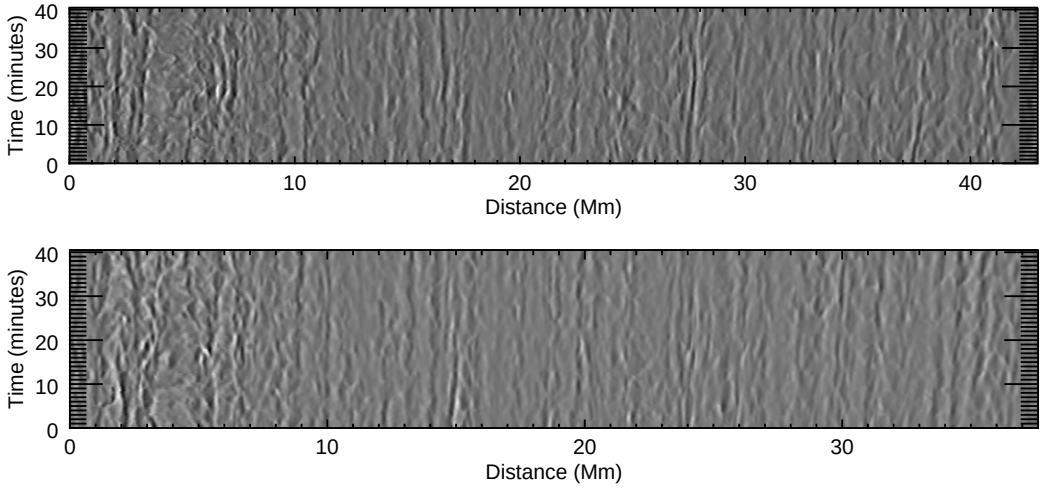

FIGURE 5.20: **Radial time-distance diagrams.** Two panel image showing example time-distance diagrams from the (semi) circular cross-cuts. The diagrams from top to bottom are from the fifteenth and sixteenth radial slits as counted from the centre (at a radius of 13-14.5 Mm), A host of transverse displacements can be seen throughout the unsharped masked image.

We found the number of detected kink waves increased as a function of radius, potentially supporting the theoretical basis that the kink waves are a result of mode conversion of low-frequency magnetoacoustic oscillations that are prevalent in areas of inclined magnetic field. The reasoning here is that increased kink wave detection results from

the abundant source of low-frequency magnetoacoustic waves able to mode convert as they propagate into the atmosphere, (e.g., Cally & Moradi, 2013, Khomenko & Cally, 2012, Schunker & Cally, 2006). However, this conclusion would be negligent without considering the fact that the increase in detection could be linked to the larger search area attributed to the radii increase in the semi-circular time-distance diagrams. It is difficult to decouple this result. For instance fixing the time-distance diagrams to a set area by reducing their sizes; would either subject the measurement to a directional location bias, if all diagrams are chosen along the same radial line. Or, if at chosen at pseudo-random locations at varying radii about the sunspot, how could one distinguish chance from assertion.

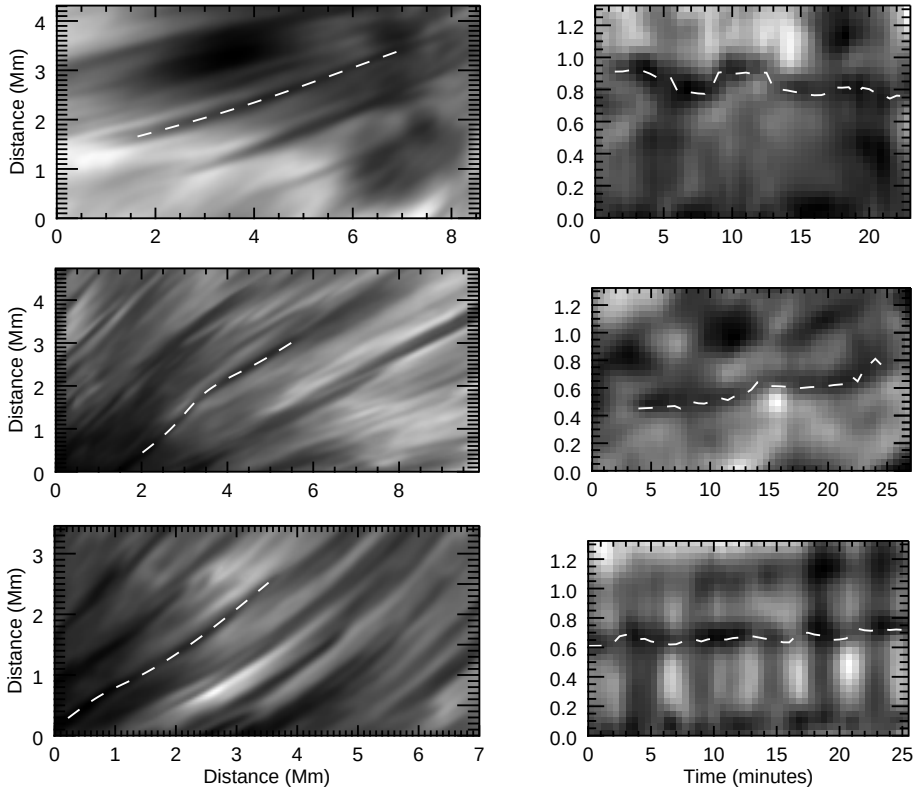

FIGURE 5.21: **Tracked super-penumbral fibrils and time-distance diagrams.** Six panel figure showing examples of isolated fibrils in the super-penumbra, left, over-plotted is the guide-line used to place cross-cute perpendicular to the structure (dashed white). On the right hand side, the incidental (x, t) diagrams from varying positions along the features. Transverse displacement can be seen around the central axis that has been tracked via the automated NUWT code (over-plotted dashed white).

By employing the curvilinear spline slit code and the automated NUWT code we track and measure ten individual fibrils in the super-penumbra, identified in the above specified region, e.g. Fig. 5.21. We isolate these fibrils with the aim of providing clear indication of the observed transverse displacement and to provide an estimate of the phase speed

along the fibril. With the cadence of this dataset at 30 s, the temporal resolution is at the limit required to provide useful wave analysis. Therefore, with this dataset we place the cross-cuts at distances of one pixel, this ensures we track the displacement over smaller separations in the event that the wave has evolved greatly over the length of the feature. In Figure 5.21, the left panels display a set of isolated fibrils and the dashed curves indicate the guide-line used to perform cross-cuts. In the right hand panels we see the consequential time-distance diagrams where evidence of the transverse oscillations are apparent, perhaps most pronounced in the top panels. The dashed white line indicates the central axis of the feature as tracked by the automated NUWT code. The temporal resolution in these images can be seen to be limiting the delineation of the wave nature, a clear example of the long cadence. In the lower right panel, manifestations of the magnetoacoustic waves can be seen as ridges in intensity, features like this are most evident in (x, t) plots that originate closer to the umbra. Relying on the same methodologies expressed in the previous chapters (Section 4.2.3), we estimate propagation speeds of the waves supported by the ten isolated fibrils.

Examining the (x, t) over the height of the fibril revealed that the structure can disappear and reappear much like the IN fibrils but on longer time periods. It may be that these occurrences are physical in nature, dependant on an underlying structure that re-organises itself after some disturbance or even some form of damping. Either scenario is not hard to believe, however we could also be observing the consequences of a sub-optimal dataset, where inter-placed dynamics could be missed due to the poor temporal resolution. Since the waves cannot be tracked across the whole fibril, the measurement of (x, t) diagrams was performed over sub-regions of the fibril, meaning that some measurements originate from the same feature but from a different sub-regions.

Figure 5.22 displays example displacement time-series and their corresponding lag-plots, transverse waves can be seen throughout the plot. Interestingly, much like the IN fibrils of the H-α data, the phase speeds appear to be invariant over the measured length. Further, the maximum phase speed value is less than that found in the IN fibrils, this is maybe unexpected in an active region where the larger magnetic field should result in a higher Alfvèn speeds as in in Equation 1.6. The difference in values from the H-α and Ca II dataset could be explained by the variation in local plasma density in each region. For instance, a drop in density in the denominator of Equation 1.6 would increase the detected phase significantly, this suggests that the H-α IN has a smaller local plasma density. The propagation speed values observed in this study are similar to those found in the recent SUNRISE results (Jafarzadeh et al., 2017b) and (Gafeira et al., 2017a) in Ca II H slender fibrils. Table 4.3 lists the measured phase speeds from the lag plot gradients and Fig. 5.23 displays the distribution, the uncertainties measured here are smaller than those found in the IN fibrils except for speeds of 40 km/s or larger.

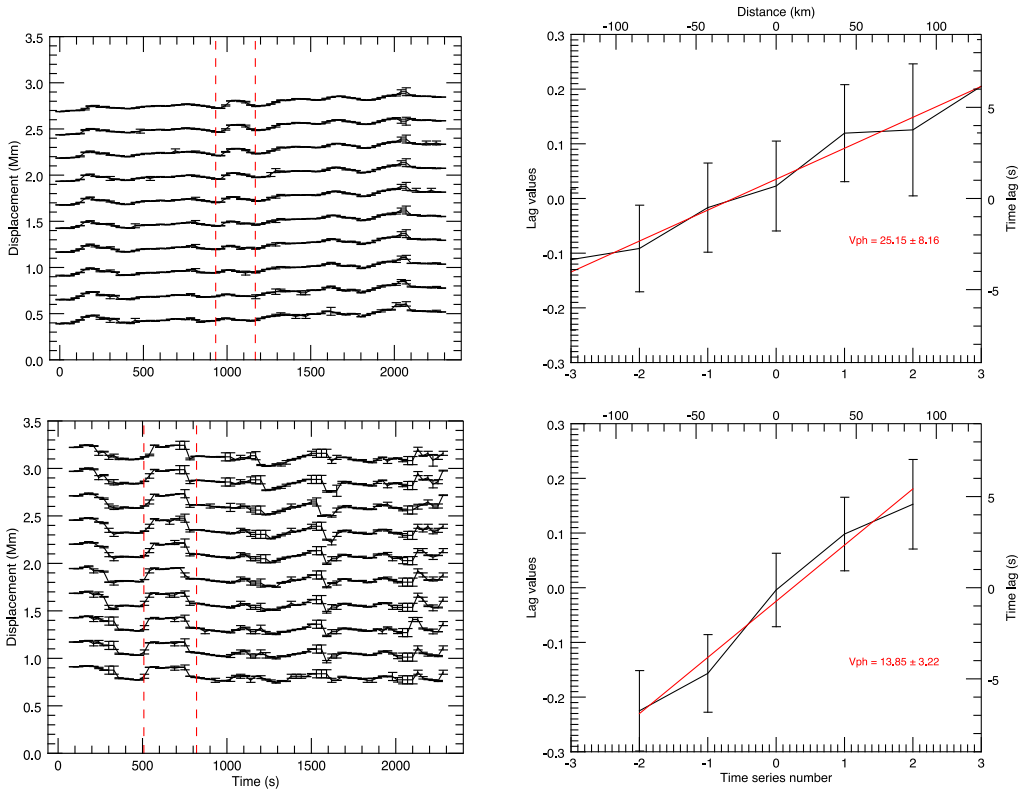

FIGURE 5.22: **Phase speed measurement of super-penumbral fibrils.** Example time-series (left panel column) from two different fibrils and their correlated lag-plots (right panel column). The time series are depicted with the black curves with associated error bars, the vertical red dotted lines indicate the time interval that the correlation was carried out. The black curve in the lag plots and associated error bars depict the lag values determined from the cross-correlation, the over-plotted red curve shows the linear least-squares fit.

Figure 5.24 displays the histograms of the measured wave properties (amplitude, period), the distribution of the amplitudes appears log-normal and the period distribution indicates two prominent periods. However, the first peak is close to three minutes, which is indicative of magnetoacoustic oscillations and so it is possible that there is some cross-contamination in the detection method. Though, the speeds are much greater than those of the running penumbral waves in (Jess et al., 2013). As shown in Section 4.2.2 multiple wave modes were detected by the NUWT system, the histograms presented here are a combination of all measured modes across all radial slits.

The averages of the measured properties can be seen in Table 5.1 and it is found that the displacement amplitudes are comparatively similar to those of the IN fibrils (though smaller) and those previously measured and listed in Table 1.1. This perhaps is expected as areas of stronger magnetic fields require greater energy to drive waves and so amplitudes are generally smaller. The average measured periods however appear far larger and both measured quantities are larger than those found in (Jafarzadeh et al.,

TABLE 5.1: Phase speeds of super-penumbra fibrils

Propagation speed (km/s)	Standard deviation
21.03	3.86
10.01	0.96
44.18	79.58
19.12	5.63
15.69	6.32
29.01	14.94
55.50	30.69
13.85	3.22
4.85	0.55
40.36	20.08
11.02	1.44
18.98	1.84
42.77	24.29
25.15	8.16

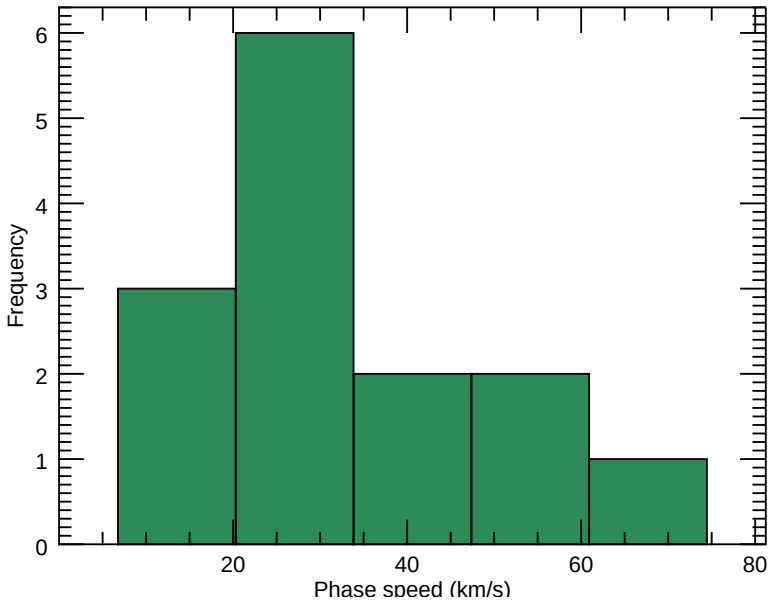

FIGURE 5.23: **Distribution of Phase speeds.** Histogram showing the distribution of phase speeds of the ten isolated super-penumbral fibrils.

2017b) and (Gafeira et al., 2017a). However, considering the larger uncertainties on the higher values the results are comparable. Compared to (Pietarila et al., 2011b), who found kink waves in a pore active region (Ca 8542 Å), we find that our phase speeds are lower. Though the authors note their measurements of the speeds are not reliable. We find comparable values for displacement amplitudes, but larger periods.

From the radial time-distance diagrams we have attempted to assess the average amplitude as a function of radius. Using the NUWT code we determine the average amplitude

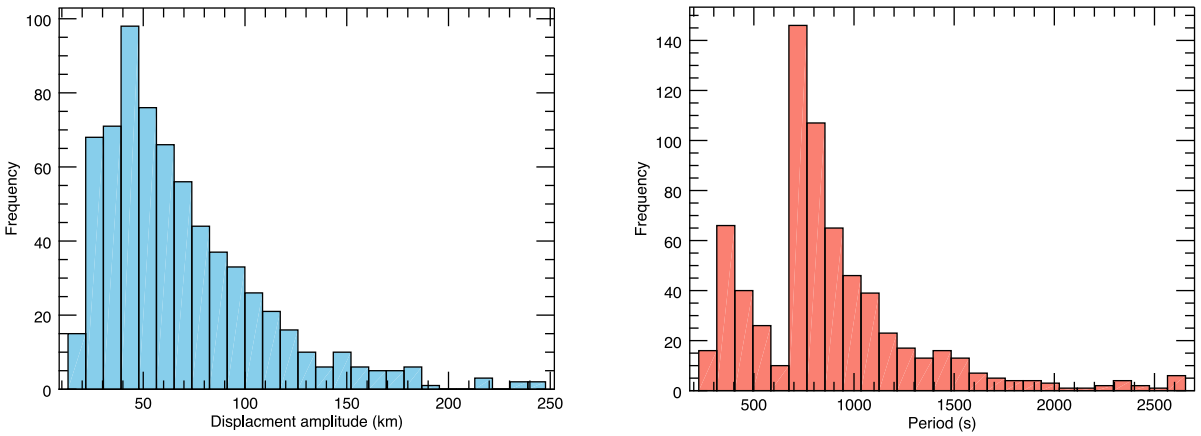

FIGURE 5.24: **Histograms for Displacement amplitude and period.** Histograms showing the displacement amplitudes (left) and periods (right) as measured from the hundreds of waves identified from the radial cross-cuts. Note, the spatial resolution of the dataset is 42 km and minimum observable period is 62.5 seconds.

TABLE 5.2: Average wave properties Ca II

	Mean	Median	Standard deviation
ξ (km)	59.31	50.08	41.01
P (s)	810.79	750.00	414.6
Propagation speed (km/s)	25.11	21.02	0.74

measured from the kink waves in each (x, t) image and errors on the mean values are determined using bootstrapping. Figure 5.25 displays the mean amplitudes with associated error-bars, the plot exhibits a positive gradient suggesting an increase in detected amplitude that may serve as an indication of density stratification with along the super-penumbral fibril. This would imply that the fibrils rise in height in the atmosphere which may be at odds with the assumed geometry of the field lines. Further, if we consider that each successive (x, t) diagram increases in size the assumed amplification could be caused by shift in the distributions as a result of the larger quantity of waves being detected.

Similar to the H-α study, we present here the average PSD for an active regions Ca II chromosphere, Fig. 5.26. The average PSD combines the measured results from the radial (x, t) diagrams where hundreds of waves are available. The methodology is the same as previously discussed in Chapter 4 subsection 4.6.2, except here the results are processed using the NUWT code and the PSD data-points are from the significant peaks only (instead of the full spectra). The over-plotted black line indicates the average PSD, red markers show the primary peaks and the orange makers the secondary peaks. The PSD scatter points, at first glance appear more dispersed than observed in the H-α

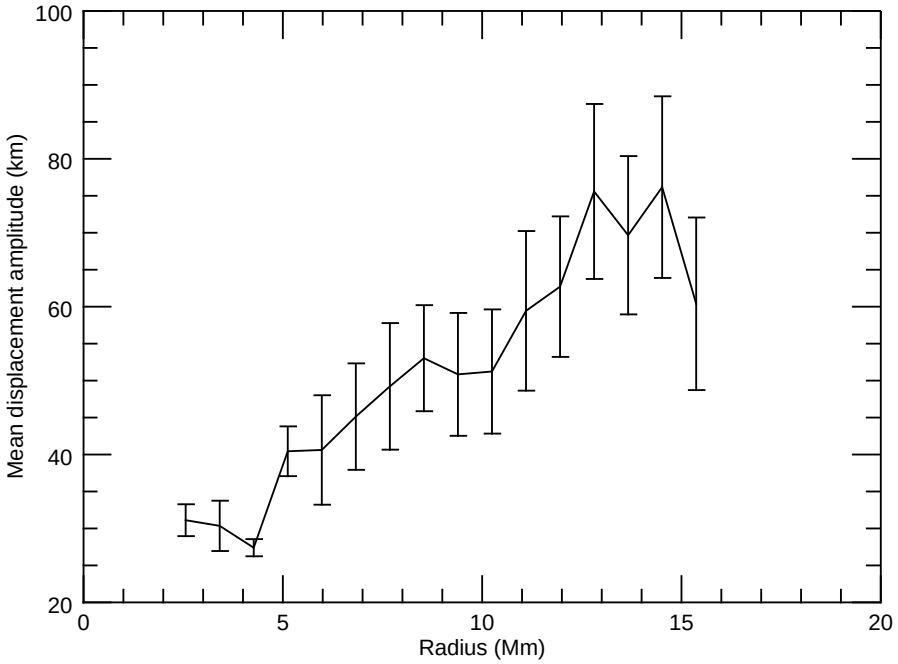

FIGURE 5.25: **Mean displacement amplitude as a function radius.** Plot showing the average displacement amplitudes as measured from each radial time-distance diagram.

dataset however this is just a manifestation of the plotting scale, both PSD scatter plots range within a factor of two. There appears to be a sharp separation of data-points at approximately 2 mHz, it is possible that a larger sample would fill this gap. The average curve here shows an upward trend, similar results were found in active regions by (Morton et al., 2014).

5.3.1 Discussion

We have presented here for the first time, direct observational evidence of kink waves supported by super-penumbral fibrils. As seen through an assortment of time-distance diagrams, the kink waves appear to be numerous with average measured properties given in Table 5.1. However, visual inspection of wave dynamics has been suboptimal due to the low temporal resolution, as such it may be possible that we are missing important features in their evolution/propagation.

We conjecture that the kink waves are the result of mode conversion of fast-magnetoacoustic waves at the equipartition layer, the theoretical literature was presented in Chapter 1 subsection 1.4.3. However, we lack the current theoretical models to prove observationally that these waves are indeed the result of mode conversion, though with the

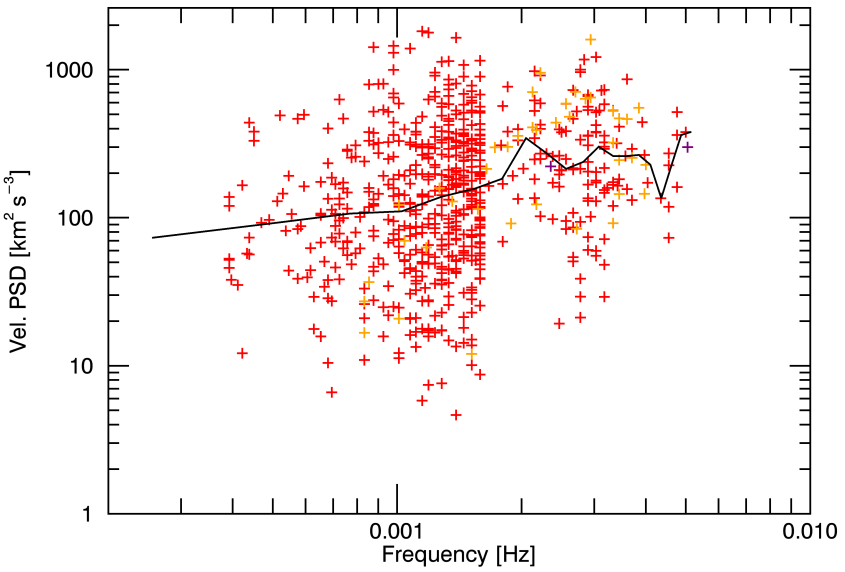

FIGURE 5.26: **Power spectral density scatter plot.** Shown here is the combined power spectral density (PSD) of ten fibrils from the super-penumbra of Ca II sunspot dataset. The over-plotted black line indicates the average PSD, red markers show the primary peaks and the orange the secondary peaks.

suppression of convection below the sunspot alternative drivers are sparse. Though it is noted that some convection does exist below the sunspot umbra, (Rempel & Schlichenmaier, 2011, Spruit & Scharmer, 2006) however power is reduced.

Signatures of magnetoacoustic waves were observed in time-series movies, (x, t) diagrams and the 2D Fourier spectrum. These waves are identified as running penumbral waves by their radial appearance in the videos and running penumbral waves have been established as slow magnetoacoustic waves, (Bloomfield et al., 2007, Jess et al., 2013). From the combined diagnostics we have seen evidence of the ramp effect in action, for instance strong periodicities in the LOS velocity umbra region (Fig. 5.4) and the high-power low-frequency waves in the super-penumbral area (Fig. 5.8). In correlation with the map of magnetic field inclination we serve a compelling argument for the abundance of waves available for conversion.

Figure 5.10 and Fig 5.11 displays the maps of the LOS magnetic field inclination angle estimated from a quiet sun model and umbral model of temperature. Like previous studies, greater inclination was inferred in the penumbra. However, it was also noted that portions of the umbra were under-mapped, due to the inner ratio of Equation 1.19 exceeding the cosine range resulting in a mathematical error. Testing both the Maltby quiet sun model and an umbral model from the Stokes inversions it was found that although the umbral model (with its lower temperature) resulted in less out of range values the overall the umbra remained under-mapped.

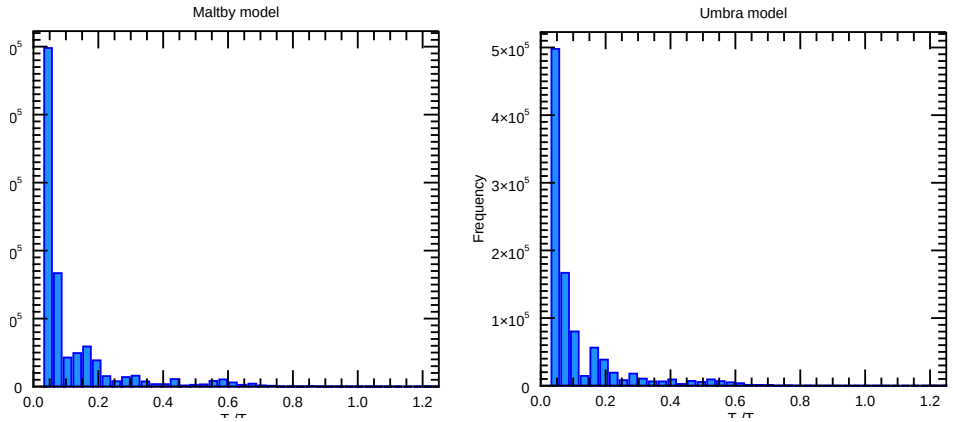

FIGURE 5.27: **Histogram of T_{cut}/T_{peak} for Maltby and Umbra models.** The distribution of T_{cut}/T_{peak} shows the the departure form the expected model ratio of 1.25, thus supplying evidence for the enhanced periodicities.

It is possible that the umbral regions of the peak period map could have larger than expected periods, this could be the result of radiative cooling which causes a 'blurring' of the cut-off frequency and in addition to the ramp effect allows the propagation of larger periods, (Bloomfield et al., 2007, Centeno et al., 2006, Khomenko et al., 2008). This could result in higher periods available in the umbra than the simple cut-off model, applied here, would account for. Displayed in Figure 5.27 is the distribution of, T_{cut}/T_{peak} for both models. Recalling equation 1.17, we should expect values close to 1.25. However, we can see that this is not the case and supports the notion for enhanced periodicities, i.e. for both temperature models T_peak is larger than the expected model.

The local average power spectral density is calculated for the active region sunspot of Ca II. Here, it was possible to combine hundreds of waves, thanks to the use of the automated NUWT code. The average PSD showed an upward trend of PSD with frequency similar to results found by (Morton et al., 2014). This is likely to be expected due the abundance of high frequency power propagating upwards through the inclined and vertical field lines. However, without multi-height data over the same region it is not possible to comment on the propagation of power through the height of the atmosphere.

As described in subsection 1.4.2, kink waves are Alfvènic, the question then arises whether the observed waves are the result of further theoretical conversion of fast-magnetic waves to Alfvèn waves. If so, are these waves resultant of those found to reflect from the transition region or those propagating upwards or even a combination of the two (from some constructive interference). The positive phase speed gradients would suggest that they are indeed upward propagating. However, these results are only from ten individual fibrils and we learn from literature (Section 1.5.4) that a high percentage of Alfvèn waves should reflect of the transition region. This being the case,

should we expect to observe a host of downward propagating Alfvènic waves? At this stage from this single study the answer to these questions cannot be determined and further studies with faster cadences may reveal more. The affirmation of kink waves in the super-penumbra, here, could yet be supplying Alfvèn waves to the coronal active regions. Furthermore, the observation of Alfvènic kink waves possibly reopens questions of downward propagating Alfvèn waves contributing to the cooling of sunspots as discussed in (Khomenko & Collados, 2015).

6

Concluding remarks

6.1 Retrospective

On the surface, any observational dataset is just an image, or a series of images in the case of a time series. However, in reality each one is a multi-faceted, agglomeration of information and it is only when you dig deeper into the data, that the true picture emerges. The intricacies of interacting with this information, how to extract physical quantities, is what this thesis has been about (or at least on the deeper level). On the grander scale, each aspect of the analysis presented here is just a tiny puzzle piece of the never ending jigsaw of solar physics. In this final section I present a summary of the research, areas of future work and open questions.

6.2 Summary

In this thesis we presented two studies examining the MHD kink wave in the quiescent H-α chromosphere and the Ca II 8542 Å active region sunspot. In the first instance, we undertook a comprehensive study of IN fibrils, which as we established are understudied magnetic wave guides. The fibrils were found to be intermittent, meaning that over time they would disappear and reappear in the same location. Suggesting that they are organised to a persistent underlying magnetic field and possibly undergo some form of cyclical heating. It was determined that these features exhibited wave-like behaviour that was interpreted as the kink wave. The kink wave properties (amplitude, period and phase speed) were measured to be on par with results from previous studies. We delivered a robust measurement approach to the phase speed and found it was invariant along the height of the feature. This enabled a magneto-seismological study that was solely

dependant to the measured displacement amplitude (within the limits of the assumed model).

The results of the magneto-seismology were difficult to interpret due to large variations in the profiles. The profiles were distributed into three observed categories, some of the profiles demonstrated evidence for damping, others enhanced amplification and the remaining profiles were in line with a model stratified atmosphere. Keeping in mind that the observed deviations were relative to the normalisation factor, and that the chosen model may not have been indicative of that atmospheric region. The evidence for damping was supported by an observed decrease in power in PSD's with height and a reduction in amplitude evident in select time-series. We explain the observation of enhanced amplification as the measurement of the combined ambient and internal densities of the flux tube and surrounding plasma. As the fibril protrudes slightly into the corona, there would be large variations in the external density that will contribute to the average density measured from the magneto-seismological profiles.

On the course of the study we discovered via statistical verification that the employed sinusoidal model may not be adequate to describe the dynamics of the measured kink waves. Further, with the use of Fourier analysis we examined how well the single period model represented the measured time-series. It was found that deviations from χ^2_2 distribution suggested non-linearity or possibly multi-periodicity.

Finally, we produced an average PSD of the quiescent H-α chromosphere that when compared to H-α photospheric PSD's, from (Chitta et al., 2012), revealed amplification of power. This result is in-line with a gravitational stratified atmosphere.

Moving forward from this analysis, the avenues for improvement and additional study are clear. Employing the curvilinear cross-cut guidelines may provide more improved measurements of the phase speeds and density profiles, as this would allow for consistent measurement along a feature rather than separate parts. In comaprison to the linear cross-cut method the key difference will be in the masurement of the phase speed. The ability to follow the curvature of the fibrils will change the separation distances between subsequent cross-cuts. This in turn will change the measurement arguably for the better, as the curvilinear method can follow the structure and thus the propgation more closley. To truly understand the differences of the two methods a statistical study would be well suited. In this manner two distributions of phase speeds could be built from the two methods of cross-cuts from the same set of fibrils. By comparing the two distributions it could be possible to understand the effects the measurments systems.

On the matter of the phase speed measurement, a less subjective method of estimation needs to be developed, for instance the use of Fourier cross spectral analysis. In regards

to the average PSD, a multi-height investigation from a single observation (or at least observations of the same region within a similar time frame) may lead to further insight to the propagation of the waves. Lastly, this study has raised the question whether the assumed single period sinusoidal model is suitable to measure the the properties of the kink wave (at least in the IN fibrils). Extensive work is needed to test a range models using methods highlighted here (e.g. KS1, Anderson Darling).

In the Ca II study we observed for the first time kink waves in super penumbral fibrils, this discovery may prove to important for the propagation of Alfvènic waves to coronal active regions. We conjecture that the kink waves result from the mode conversion of upward propagating magnetoacoustic waves from the lower atmosphere. Evidence was shown to support the notion that these acoustic waves could propagate into the chromosphere by means of the ramp effect, thus confirming that the findings from previous studies apply here. However, with current theoretical understanding it is difficult to prove the link between mode conversion and the manifestation of kink waves observationally. Though, with the knowledge that convection is suppressed, alternative drivers are slim.

Utilising methods similar to that of the H-α study, we measured the amplitude, periods and phase speed of the kink waves. In general, the measurements were in agreement with studies of kink waves in other regions, though the measured periods were larger and phase speeds were much smaller. However, due to the long cadence of the dataset compared the time-scales typical of chromospheric features, it is possible that we are missing dynamics. As such, the temporal variations and hence periods measurements may be incomplete. Two distinct peaks were found in the period histograms, suggesting waves in the super-penumbra held two prominent periods. Alternatively, it is possible that there is some cross contamination from magnetoacoustic waves in the automated NUWT measurement system. Multiple peaks were also detected via the automated NUWT code significance test, which could be an indication of cross contamination. Although, the waves could be multi-periodic.

Despite the expected larger magnetic field strengths in the sunspot, the phase speeds measured in the super-penumbral fibrils were smaller than those found in the IN fibrils. This would indicate that the plasma density in the Ca II fibrils is larger than the H-α. This is likely due to the respective local plasma and magnetic field conditions of the quiet IN (weak field and low density) and active region sunspot (strong field, high density). Interestingly, the phase speeds of the super-penumbral fibrils were also found to be invariant along the height of the fibril.

It was shown that the average displacement amplitude increased with radial distance from the sunspot centre, possibly indicating density stratification along the fibril. This

would imply that the fibril may be rising into the atmosphere. However, the displacement amplitudes have an asymmetric distribution and the mean average can be affected by the tails. Thus, a more accurate measure of the average may be needed.

Finally, with the same methodology as in the H-α data we produced a local average PSD, this time of the sunspot active region Ca II chromosphere. Similar to that of (Morton et al., 2014) we found an increasing power spectra with respect to frequency as opposed to the downward spectra found in the quiet sun. Unfortunately, it is difficult to make further interpretations due to the lack of further observations, multi-height or of similar regions, for comparison.

The study of kink waves in super-penumbral fibrils would greatly benefit from a high-cadence dataset, this would allow better estimates of the wave properties. Further, a multi-height study of the average PSD would enable a better understanding of the propagation of waves in the super-penumbra. Moreover, though we cannot directly link mode conversion of the magnetoacoustic waves to the kink waves, we may be able to eliminate other possible drivers.

In both studies we employed line width diagnostics, though we recognised that the measured width may be contaminated with photospheric contributions. Therefore, as part of future work more accurate methods to determine the widths will need to be employed, such as, the lambda metre method or even the La Palma codes as mentioned in Section 3. Correlating line width data with temperature information from Stokes inversions could help determine heating events in these features.

6.3 Open questions

At last, we come to the open questions. Much of this research has relied on assumed geometry of fibrils which in turn underpins the interpretations. However, there may not be a 'typical' fibril geometry and it may depend on how the fibril is formed, which currently is also undetermined. Further, in this work we have presented an example of a flow along a fibril, what effect this flow may have on the measured properties and internal densities is difficult to determine observationally. It may be appropriate to form some simulation to replicate a flow and compare it to a fibril without.

Additionally, we have discussed the suitability of a single period sinusoidal model and determined that further work is needed to test it against other models. Though, the tests carried out in this study were on a small sample of fibrils. Therefore, it is possible that the model may be adequate for some and not others, as such more statistics are required. On this point, is this behaviour evident in other features? We have also suggested that

the fibrils from both the H-α and Ca II data show multi-periodicity, what does this mean in terms of coupling of the kink mode?

Finally, if possible how can we examine mode conversion observationally?

As we approach a new dawn of observations with the construction of world class instruments; the Daniel K. Inouye Solar Telescope, European Solar Telescope and Solar Orbiter, we embark on an era of higher resolution data that is unprecedented. Moreover, advancements in computational power will allow advanced 3D simulations, with this combination we may find the answers to some of these questions (and probably a lot more).

Bibliography

Andrae, R. 2010, ArXiv e-prints

Andrae, R., Schulze-Hartung, T., & Melchior, P. 2010, ArXiv e-prints

Antolin, P., et al. 2015, ApJ, 809, 72

Aschwanden, M. J. & Schrijver, C. J. 2011, ApJ, 736, 102

Asensio Ramos, A., de la Cruz Rodríguez, J., Martínez González, M. J., & Socas-Navarro, H. 2017, A&A, 599, A133

Aulanier, G., et al. 2007, Science, 318, 1588

Balasubrahmanyan, V. K. 1969, Sol. Phys., 7, 39

Banerjee, D., Erdélyi, R., Oliver, R., & O'Shea, E. 2007, Sol. Phys., 246, 3

Beck, C., Khomenko, E., Rezaei, R., & Collados, M. 2009, A&A, 507, 453

Beck, C., Rezaei, R., & Puschmann, K. G. 2012, A&A, 544, A46

Beck, C., Rezaei, R., & Puschmann, K. G. 2013a, A&A, 549, A24

Beck, C., Rezaei, R., & Puschmann, K. G. 2013b, A&A, 553, A73

Bel, N. & Leroy, B. 1977, A&A, 55, 239

Bello González, N., Flores Soriano, M., Kneer, F., & Okunev, O. 2009, A&A, 508, 941

Bello González, N., Flores Soriano, M., Kneer, F., Okunev, O., & Shchukina, N. 2010, A&A, 522, A31

Berger, T. E. & Title, A. M. 1996, ApJ, 463, 365

Bloomfield, D. S., Lagg, A., & Solanki, S. K. 2007, ApJ, 671, 1005

Bloomfield, D. S., McAteer, R. T. J., Mathioudakis, M., Williams, D. R., & Keenan, F. P. 2004, ApJ, 604, 936

Bobra, M. G., et al. 2014, Sol. Phys., 289, 3549

Cally, P. S. 2005, MNRAS, 358, 353

Cally, P. S. 2011, in Astronomical Society of India Conference Series, Vol. 2, Astronomical Society of India Conference Series, 221–227

Cally, P. S. & Goossens, M. 2008, Sol. Phys., 251, 251

Cally, P. S. & Moradi, H. 2013, MNRAS, 435, 2589

Carlsson, M., et al. 2007, PASJ, 59, S663

Cauzzi, G., Reardon, K., Rutten, R. J., Tritschler, A., & Uitenbroek, H. 2009, A&A, 503, 577

Cauzzi, G., et al. 2008, A&A, 480, 515

Centeno, R., Collados, M., & Trujillo Bueno, J. 2006, ApJ, 640, 1153

Centeno, R., et al. 2014, Sol. Phys., 289, 3531

Centeno, R., Trujillo Bueno, J., & Asensio Ramos, A. 2010, ApJ, 708, 1579

Chae, J., et al. 2014, ApJ, 789, 108

Chitta, L. P., van Ballegooijen, A. A., Rouppe van der Voort, L., DeLuca, E. E., & Kariyappa, R. 2012, ApJ, 752, 48

Choudhuri, A. R., Auffret, H., & Priest, E. R. 1993, Sol. Phys., 143, 49

Cranmer, S. R. & van Ballegooijen, A. A. 2005, ApJS, 156, 265

Cuntz, M., Rammacher, W., & Musielak, Z. E. 2007, The Astrophysical Journal, 657

de la Cruz Rodríguez, J., De Pontieu, B., Carlsson, M., & Rouppe van der Voort, L. H. M. 2013, ApJ, 764, L11

de la Cruz Rodríguez, J. & Socas-Navarro, H. 2011, A&A, 527, L8

de la Cruz Rodríguez, J., Socas-Navarro, H., Carlsson, M., & Leenaarts, J. 2012, A&A, 543, A34

de la Cruz Rodríguez et al. 2015, A&A, 573, A40

De Moortel, I. 2009, Space Science Reviews, 149, 65

De Moortel, I. & Galsgaard, K. 2006, A&A, 459, 627

De Pontieu, B., et al. 2012, ApJ, 752, L12

De Pontieu, B., Erdélyi, R., & James, S. P. 2004, Nature, 430, 536

De Pontieu, B., et al. 2007a, PASJ, 59, 655

De Pontieu, B., et al. 2011, Science, 331, 55

De Pontieu, B., et al. 2007b, Science, 318, 1574

de Wijn, A. G., Rutten, R. J., Haverkamp, E. M. W. P., & Sütterlin, P. 2005, A&A, 441, 1183

Deubner, F.-L. 1975, Sol. Phys., 40, 333

Domínguez Cerdeña, I., Kneer, F., & Sánchez Almeida, J. 2003, ApJ, 582, L55

Druett, M., et al. 2017, Nat. Commun., 8, 15905 EP

Dymova, M. V. & Ruderman, M. S. 2006, A&A, 457, 1059

Ebadi, H., Zaqarashvili, T. V., & Zhelyazkov, I. 2012, Ap&SS, 337, 33

Edwin, P. M. & Roberts, B. 1983, Sol. Phys., 88, 179

Erdélyi, R. & Fedun, V. 2006, Sol. Phys., 238, 41

Fedun, V. 2014, MHD simulations from the Solar Wave Theory Group (SWAT)

Fossum, A. & Carlsson, M. 2006, The Astrophysical Journal, 592

Gafeira, R., et al. 2017a, ApJS, 229, 7

Gafeira, R., et al. 2017b, ApJS, 229, 6

Gary, G. A. 2001, Sol. Phys., 203, 71

Gaskell. 1987, The Astrophysical Journal, 65, 1

Giannattasio, F., et al. 2014a, A&A, 569, A121

Giannattasio, F., Stangalini, M., Berrilli, F., Del Moro, D., & Bellot Rubio, L. 2014b, ApJ, 788, 137

Goossens, M. 2003, An Introduction to Plasma Astrophysics and Magnetohydrodynamics, Vol. 294 (Kluwer Academic Publishers)

Goossens, M. 2008, in IAU Symposium, Vol. 247, IAU Symposium, 228–242

Goossens, M., Soler, R., Terradas, J., Van Doorsselaere, T., & Verth, G. 2014, ApJ, 788, 9

Goossens, M., Terradas, J., Andries, J., Arregui, I., & Ballester, J. L. 2009, A&A, 503, 213

Gošić, M., Bellot Rubio, L. R., Orozco Suárez, D., Katsukawa, Y., & del Toro Iniesta, J. C. 2014, ApJ, 797, 49

Guo, Y., et al. 2015, ApJ, 799, 151

Hansen, S. C. & Cally, P. S. 2012, ApJ, 751, 31

He, J., Marsch, E., Tu, C., & Tian, H. 2009a, ApJ, 705, L217

He, J.-S., et al. 2009b, A&A, 497, 525

Heinzel, G., Rüdiger, A., & Schilling, R. 2002, Spectrum and spectral density estimation by the Discrete Fourier transform (DFT), including a comprehensive list of window functions and some new flat-top windows

Henriques, V. M. J. 2012, A&A, 548, A114

Henriques, V. M. J. 2013, PhD thesis, University of Stockholm

Henriques, V. M. J., Kuridze, D., Mathioudakis, M., & Keenan, F. P. 2016, ApJ, 820, 124

Henriques, V. M. J., Mathioudakis, M., Socas-Navarro, H., & de la Cruz Rodríguez, J. 2017, ApJ, 845, 102

Hillier, A., Morton, R. J., & Erdélyi, R. 2013, ApJ, 779, L16

Hood, A. W. 2000, St Andrews: Sun Course

IAC. 2017, Observatorio del Roque de los Muchachos - Instituto de Astrofísica de Canarias -

institute for Plasma Physics, M. P. 2003, Plasma diagram

ISF. 2002, Institute for Solar Physics - Stockholm

Jafarzadeh, S., et al. 2017a, ApJS, 229, 11

Jafarzadeh, S., et al. 2017b, ApJS, 229, 9

Jakosky, B. M., et al. 2017, Science, 355, 1408

Jefferies, S. M., et al. 2006, in ESA Special Publication, Vol. 624, Proceedings of SOHO 18/GONG 2006/HELAS I, Beyond the spherical Sun, 16.1

Jess, D. B., Mathioudakis, M., & Keys, P. H. 2014, ApJ, 795, 172

Jess, D. B., et al. 2015, Space Sci. Rev., 190, 103

Jess, D. B., et al. 2012, ApJ, 744, L5

Jess, D. B., Reznikova, V. E., Van Doorsselaere, T., Keys, P. H., & Mackay, D. H. 2013, ApJ, 779, 168

Judge, P. 2006, in ASP Conference Series, Vol. 354, Solar MHD Theory and Observations: A High Spatial Resolution Perspective, ed. Leibacher, J. and Stein, R. F. and Uitenbroek, H.

Karampelas, K., Van Doorsselaere, T., & Antolin, P. 2017, ArXiv e-prints

Khomenko, E. & Cally, P. S. 2012, ApJ, 746, 68

Khomenko, E. & Calvo Santamaria, I. 2013, in Journal of Physics Conference Series, Vol. 440, Journal of Physics Conference Series, 012048

Khomenko, E., Centeno, R., Collados, M., & Trujillo Bueno, J. 2008, ApJ, 676, L85

Khomenko, E. & Collados, M. 2006, ApJ, 653, 739

Khomenko, E. & Collados, M. 2015, Living Reviews in Solar Physics, 12, 6

Kim, Y.-H., et al. 2008, Journal of Korean Astronomical Society, 41, 173

Klimchuk, J. A. 2015, Philosophical Transactions of the Royal Society of London Series A, 373, 20140256

Klimchuk, J. A., Karpen, J. T., & Antiochos, S. K. 2010, ApJ, 714, 1239

Kubo, M., et al. 2008, in Astronomical Society of the Pacific Conference Series, Vol. 397, First Results From Hinode, ed. S. A. Matthews, J. M. Davis, & L. K. Harra, 79

Kuridze, D., et al. 2015, ApJ, 802, 26

Kuridze, D., et al. 2013, ApJ, 779, 82

Langangen, Ø., et al. 2008, ApJ, 679, L167

Leenaarts, J., Carlsson, M., & Rouppe van der Voort, L. 2012, ApJ, 749, 136

Leenaarts, J., Carlsson, M., & Rouppe van der Voort, L. 2015, ApJ, 802, 136

Leighton, R. B., Noyes, R. W., & Simon, G. W. 1962, ApJ, 135, 474

Lilliefors, H. 1969, J AMER STATIST ASSN, 62, 399

Liu, Z.-X., He, J.-S., & Yan, L.-M. 2014, Research in Astronomy and Astrophysics, 14, 299

Ljung, G. M. & Box, G. E. P. 1978, Biometrika, 65, 297

Löfdahl, M. G. 2002, in Proc. SPIE, Vol. 4792, Image Reconstruction from Incomplete Data, ed. P. J. Bones, M. A. Fiddy, & R. P. Millane, 146–155

Löhner-Böttcher, J. 2016, PhD thesis, Universität Freiburg im Breisgau

Maltby, P., et al. 1986, ApJ, 306, 284

Markwardt, C. B. 2009, in ASPCS, Vol. 411, Astronomical Data Analysis Software and Systems XVIII, ed. D. A. Bohlender, D. Durand, & P. Dowler, 251

Marsh, K. A. 1976, Sol. Phys., 50, 37

Martínez-Sykora, J., De Pontieu, B., Carlsson, M., & Hansteen, V. 2016, ApJ, 831, L1

Mathioudakis, M., Jess, D. B., & Erdélyi, R. 2013, Space Sci. Rev., 175, 1

McAteer, R. T. J., et al. 2003, ApJ, 587, 806

McCracken, K. G., Beer, J., & McDonald, F. B. 2002, Geophysical Research Letters, 29, 14, 2161

McLaughlin, J. A., De Moortel, I., Hood, A. W., & Brady, C. S. 2009, A&A, 493, 227

McLaughlin, J. A., Thurgood, J. O., & MacTaggart, D. 2012a, A&A, 548, A98

McLaughlin, J. A., Verth, G., Fedun, V., & Erdélyi, R. 2012b, ApJ, 749, 30

Mooroogen, K., Morton, R. J., & Henriques, V. 2017, ArXiv e-prints

Mooroogen, K., Scott, O., & Morton, R. J. 2016, Spline Slit Code Document, 1st edn., Northumbria University: Mathematics, Physics and Electrical Engineering, Solar Group

Morton, R. J. 2014, Astronomy & Astrophysics, 566, 13pp

Morton, R. J. & McLaughlin, J. A. 2014, ApJ, 789, 105

Morton, R. J. & Mooroogen, K. 2016, A&A, 593, A59

Morton, R. J., Mooroogen, K., & McLaughlin, J. 2016, Wave Tracking Code Document, 1st edn., Northumbria University: Mathematics, Physics and Electrical Engineering, Solar Group, Newcastle Upon Tyne, Ellison Place

Morton, R. J. & Ruderman, M. S. 2011, A&A, 527, A53+

Morton, R. J., Tomczyk, S., & Pinto, R. 2015, Submitted

Morton, R. J., Verth, G., Fedun, V., Shelyag, S., & Erdélyi, R. 2013, ApJ, 768, 17

Morton, R. J., Verth, G., Hillier, A., & Erdélyi, R. 2014, ApJ, 784, 29

Morton, R. J., et al. 2012a, Nat. Commun., 3, 1315

Morton, R. J., Verth, G., McLaughlin, J. A., & Erdélyi, R. 2012b, ApJ, 744, 5

Mumford, S. J., Fedun, V., & Erdélyi, R. 2015, ApJ, 799, 6

Nakariakov, V. M. & Roberts, B. 1995, Sol. Phys., 159, 213

Narayan, G. 2011, A&A, 529, A79

Narayanan, A. S. 2013, An Introduction to Waves and Oscillations in the Sun (Springer)

Nisenson, P., van Ballegooijen, A. A., de Wijn, A. G., & Sütterlin, P. 2003, ApJ, 587, 458

Noyes, R. W. & Leighton, R. B. 1963, ApJ, 138, 631

Okamoto, T. J., et al. 2015, ApJ, 809, 71

Okamoto, T. J. & De Pontieu, B. 2011, ApJ, 736, L24

Olsen, S. I. 1993, CVGIP: Graphical Models and Image Processing, 55, 319

Orozco Suárez, D. & Bellot Rubio, L. R. 2012, ApJ, 751, 2

Pant, V., et al. 2015, Research in Astronomy and Astrophysics, 15, 1713

Parker, E. N. 1958, ApJ, 128, 677

Parker, E. N. 1964, ApJ, 140, 1170

Parker, E. N. 1988, ApJ, 330, 474

Parnell, C. E. 2004, in ESA Special Publication, Vol. 575, SOHO 15 Coronal Heating, ed. R. W. Walsh, J. Ireland, D. Danesy, & B. Fleck, 227

Parnell, C. E. & De Moortel, I. 2012, Royal Society of London Philosophical Transactions Series A, 370, 3217

Pereira, T. M., De Pontieu, B., & Carlsson, M. 2012, ApJ, 759, 16

Pereira, T. M. D., De Pontieu, B., & Carlsson, M. 2013, ApJ, 764, 69

Pietarila, A., Aznar Cuadrado, R., Hirzberger, J., & Solanki, S. K. 2011a, ApJ, 739, 92

Pietarila, A., Aznar Cuadrado, R., Hirzberger, J., & Solanki, S. K. 2011b, ApJ, 739, 92

Priest, E. 2014, Magnetohydrodynamics of the Sun (Cambridge University Press)

Reardon, K. P., Yang, Y. M., Muglach, K., & Warren, H. P. 2011, ApJ, 742, 119

Rempel, M. & Schlichenmaier, R. 2011, Living Reviews in Solar Physics, 8, 3

Rouppe van der Voort, L. & de la Cruz Rodríguez, J. 2013, ApJ, 776, 56

Rouppe van der Voort, L., De Pontieu, B., Pereira, T. M. D., Carlsson, M., & Hansteen, V. 2015, ApJ, 799, L3

Rouppe van der Voort, L., Leenaarts, J., de Pontieu, B., Carlsson, M., & Vissers, G. 2009, ApJ, 705, 272

Rouppe van der Voort, L. H. M., De Pontieu, B., Hansteen, V. H., Carlsson, M., & van Noort, M. 2007, ApJ, 660, L169

Rutten, R. J. 2007, in Astronomical Society of the Pacific Conference Series, Vol. 368, The Physics of Chromospheric Plasmas, ed. P. Heinzel, I. Dorotovič, & R. J. Rutten, 27

Rutten, R. J. 2008, in Astronomical Society of the Pacific Conference Series, Vol. 397, First Results From Hinode, ed. S. A. Matthews, J. M. Davis, & L. K. Harra, 54

Rutten, R. J. 2010, Mem. Soc. Astron. Italiana, 81, 565

Rutten, R. J. 2016, A&A, 590, A124

Rutten, R. J. 2017, A&A, 598, A89

Rutten, R. J. & Rouppe van der Voort, L. H. M. 2017, A&A, 597, A138

S. Habbal, M. D. & Aniol, P. 2017, Total eclispe

Sakamoto, Y., Tsuneta, S., & Vekstein, G. 2008, ApJ, 689, 1421

Samanta, T., et al. 2016, ApJ, 828, 23

Schad, T. A., Penn, M. J., & Lin, H. 2013, ApJ, 768, 111

Scharmer, G. B., Bjelksjo, K., Korhonen, T. K., Lindberg, B., & Petterson, B. 2003, in Proc. SPIE, Vol. 4853, Innovative Telescopes and Instrumentation for Solar Astrophysics, ed. S. L. Keil & S. V. Avakyan, 341–350

Scherrer, P. H., et al. 2012, Sol. Phys., 275, 207

Schmieder, B. & Mein, N. 1980, A&A, 84, 99

Schnack, D. D. 2009, Ideal MHD and the Frozen Flux Theorem (Berlin, Heidelberg: Springer Berlin Heidelberg), 49–53

Schnerr, R. S., de La Cruz Rodríguez, J., & van Noort, M. 2011, A&A, 534, A45

Schou, J., et al. 2012a, Sol. Phys., 275, 327

Schou, J., et al. 2012b, Sol. Phys., 275, 229

Schrijver, C. J. & Title, A. M. 2003, ApJ, 597, L165

Schunker, H. & Cally, P. S. 2006, MNRAS, 372, 551

Sekse, D. H., Rouppe van der Voort, L., & De Pontieu, B. 2012, ApJ, 752, 108

Sekse, D. H., Rouppe van der Voort, L., & De Pontieu, B. 2013a, ApJ, 764, 164

Sekse, D. H., Rouppe van der Voort, L., De Pontieu, B., & Scullion, E. 2013b, ApJ, 769, 44

Snow, B., Botha, G. J. J., & Régnier, S. 2015, A&A, 580, A107

Socas-Navarro, H. 2015, NICOLE: NLTE Stokes Synthesis/Inversion Code, Astrophysics Source Code Library

Solanki, S. K., et al. 2010, ApJ, 723, L127

Soler, R., Oliver, R., & Ballester, J. L. 2009, ApJ, 707, 662

Soler, R. & Terradas, J. 2015, ApJ, 803, 43

Soler, R., Terradas, J., Oliver, R., Ballester, J. L., & Goossens, M. 2010, ApJ, 712, 875

Soler, R., Terradas, J., Verth, G., & Goossens, M. 2011, ApJ, 736, 10

Spruit, H. C. & Scharmer, G. B. 2006, A&A, 447, 343

Stanford.edu. 2010, Helioseismic and Magnetic Imager

Stangalini, M., Del Moro, D., Berrilli, F., & Jefferies, S. M. 2011, A&A, 534, A65

Stangalini, M., Giannattasio, F., & Jafarzadeh, S. 2015, A&A, 577, A17

Starck, J.-L. & Murtagh, F. 2006, Astronomical Image and Data Analysis, 2nd edn. (Springer-Verlag Berlin Heidelberg)

Stenborg, G. & Cobelli, P. J. 2003, A&A, 398, 1185

Stephens, M. A. 1974, Journal of the American Statistical Association, 69, 730

Suematsu, Y., et al. 2008, Sol. Phys., 249, 197

Terradas, J., Goossens, M., & Verth, G. 2010, A&A, 524, A23

Terzo, S., et al. 2011, ApJ, 736, 111

Testa, P., et al. 2013, ApJ, 770, L1

Thomas, J. H., Weiss, N. O., Tobias, S. M., & Brummell, N. H. 2002, Nature, 420, 390

Tobias, S. & Weiss, N. 2007, in The Solar Tachocline, ed. D. W. Hughes, R. Rosner, & N. O. Weiss, 319

Tomczyk, S., et al. 2007, Science, 317, 1192

Torrence, C. & Compo, G. P. 1998, Bull. Am. Meteorol. Soc., 79, 61

Tsiropoula, G., et al. 2012, Space Sci. Rev., 169, 181

Uitenbroek, H. 2006, in Astronomical Society of the Pacific Conference Series, Vol. 354, Solar MHD Theory and Observations: A High Spatial Resolution Perspective, ed. Leibacher, J. and Stein, R. F. and Uitenbroek, H., 313

Ulmschneider, P. 1976, Sol. Phys., 49, 249

van Ballegooijen, A. A., Asgari-Targhi, M., Cranmer, S. R., & DeLuca, E. E. 2011, ApJ, 736, 3

Van Doorsselaere, T., Gijsen, S. E., Andries, J., & Verth, G. 2014, ApJ, 795, 18

van Noort, M., Rouppe van der Voort, L., & Löfdahl, M. G. 2005, Sol. Phys., 228, 191

Vaughan, S. 2005, A&A, 431, 391

Vecchio, A., Cauzzi, G., & Reardon, K. P. 2009, A&A, 494, 269

Vernazza, J. E., Avrett, E. H., & Loeser, R. 1981, ApJS, 45, 635

Verth, G. & Erdélyi, R. 2008, A&A, 486, 1015

Verth, G., Goossens, M., & He, J.-S. 2011, ApJ, 733, L15

Wang, H. & Zirin, H. 1988, Sol. Phys., 115, 205

Weberg, M. J., Morton, R. J., & McLaughlin, J. A. 2016, AGU Fall Meeting Abstracts

Welsh, W. 1999, Chicago Journals, 111, 1347

Weston, E. B. 1972, PASP, 84, 645

White, O. R. & Athay, R. G. 1979a, ApJS, 39, 317

White, O. R. & Athay, R. G. 1979b, ApJS, 39, 347

Wiegelmann, T., et al. 2010, ApJ, 723, L185

Zhou, G. P., Wang, J. X., & Jin, C. L. 2010, Sol. Phys., 267, 493

Zhugzhda, Y. D., Balthasar, H., & Staude, J. 2000, A&A, 355, 347

Zirin, H. 1988, Astrophysics of the Sun (Cambridge University Press)